UNIVERSITY OF SOUTHAMPTON

FACULTY OF PHYSICAL SCIENCES AND ENGINEERING

Optoelectronics Research Centre

Single mode fibre based interaction of trapped ions enhanced by optical cavities

by

Dean T. Clarke

Thesis for the degree of Master in Philosophy

Primary Supervisor: Dr Peter Horak

Secondary Supervisor: Dr Tim Freegarde

September 12, 2019

UNIVERSITY OF SOUTHAMPTON

ABSTRACT

FACULTY OF PHYSICAL SCIENCES AND ENGINEERING
Optoelectronics Research Centre

Master of Philosophy

SINGLE MODE FIBRE BASED INTERACTION OF TRAPPED IONS ENHANCED BY OPTICAL CAVITIES

by Dean T. Clarke

Quantum technology has the potential to change the way we solve many problems in our daily lives. Perhaps the most ambitious quantum technology in development is quantum computers. In the past decade significant progress has been made in the number of qubits within a quantum computer, and this trend seems to be increasing.

In this work we look at one particular architecture for quantum computing; the ion-trap quantum computer. In this thesis we investigate the integration of this type of quantum computer with fibre tip optical cavities. We numerically analyse the effect of misalignment of these cavities and attempt to find the optimal cavity parameters for integration into the ion-trap quantum computer.

This work should provide a useful framework for optimal integration of cavities, and the tolerances to misalignment. This should allow for future ion-trap quantum computer designs to be more efficient and help increase the number of qubits, paving the way to develop a useful universal quantum computer.

Contents

List of Figures

List of Tables

List of Definitions

R_{mir} = Radius of the mirror i.e. half the mirror diameter.

L = Cavity length.

l = Fibre length.

λ = Wavelength of light used in the cavity.

z = Cavity axis.

W_0 = Waist size of a Gaussian beam.

Z_0 = Rayleigh range of the Gaussian beam.

$\eta(z)$ = Gouy phase of the Gaussian beam at position z.

E_0 = Electric field amplitude of the Gaussian beam.

$\eta_{cl} = 1 - \kappa_{clip}$ = Clipping loss at a mirror.

$\eta_{cl1} + \eta_{cl2} = 1 - \rho$ = Clipping loss after 1 round trip.

η = Overlap of a misaligned beam with the perfectly aligned beam at the mirror surface.

$R(z)$ = Radius of curvature of the Gaussian beam wavefront at position z.

W_m = Size of the Gaussian beam at a point z, usually the sub index m will be used to indicate the spot size at the mirror surface.

$R_{1,2}$ = Radius of curvature of mirror 1 and 2 (in this thesis R_1 is taken as negative and R_2 as positive).

M_{ax} = Misalignment of the mirrors relative to each other.

M_m = Misalignment of the cavity mode on the mirror.

M_{tol} = Tolerance to mirror axial misalignment.

θ_{tol} = Tolerance to tilted mirror misalignment.

R_{ef} = Mirror reflectivity.

T = Mirror transmission

D_m = Mirror depth.

M_D = Mirror depth at a given point.

Q = Cavity Q-factor.

F = Cavity finesse.

κ = Cavity decay rate.

g = Coupling strength to the atom.

γ = Atom decay rate.

C = Cooperativity.

δ = A value used to simplify the dimensionless radius of curvature defined by $|R/L|-0.5$.

Declaration of Authorship

I, Dean T. Clarke , declare that the thesis entitled *Single mode fibre based interaction of trapped ions enhanced by optical cavities* and the work presented in the thesis are both my own, and have been generated by me as the result of my own original research. I confirm that:

- this work was done wholly or mainly while in candidature for a research degree at this University;
- where any part of this thesis has previously been submitted for a degree or any other qualification at this University or any other institution, this has been clearly stated;
- where I have consulted the published work of others, this is always clearly attributed;
- where I have quoted from the work of others, the source is always given. With the exception of such quotations, this thesis is entirely my own work;
- I have acknowledged all main sources of help;
- where the thesis is based on work done by myself jointly with others, I have made clear exactly what was done by others and what I have contributed myself;
- parts of this work have been published as: [98]

Signed:.....

Date:.....

Acknowledgements

I would like to thank my supervisor Peter Horak for his patience and support throughout this project.

Chapter 1

Introduction

This chapter will cover a brief history of the subject area, the goals of the project, and an overall thesis summary.

Section 1.1 briefly goes over the motivation for researching quantum technologies.

Section 1.2 looks at how quantum theory is being used to build quantum computers.

Section 1.3 covers how we can get qubits to communicate to build a quantum network, and the motivations for doing so.

Section 1.4 looks at the requirements for fault tolerant universal quantum computing, with special interest on one particular system.

Section 1.5 outlines the goals of this project.

Section 1.6 gives a brief outline of each chapter of the thesis.

1.1 The Quantum Revolution

In the early 1900s the discovery of the particle nature of light[1] caused a revolution in physics of new quantum theories. This caused a lot of debate among physicists of the time about the nature of the universe. Since then, the original quantum theories have been used to exploit the quantised nature of electronic states perhaps most notably in semiconductor technology, creating many new technologies such as lasers and the transistor. These technologies are the backbone of many important aspects of the modern age such as classical information processing and internet communications.

Due to the success of the first quantum revolution there is now a major worldwide push for the 'second quantum revolution' based on exploiting quantum effects such as superposition and entanglement[2]. The goal of the second quantum revolution is to create new technology for secure communications, quantum information processing, quantum simulation, advanced imaging and quantum sensors.

Since the universe is inherently quantum, and numerical research is done on classical computers many aspects of physics have been extremely hard to simulate and as a result quantum information processing will be a powerful new tool for solving certain types of problems. In 1982 on the topic of quantum computers R. Feynman said:

"...nature isn't classical, dammit, and if you want to make a simulation of nature, you'd better make it quantum mechanical, and by golly it's a wonderful problem, because it doesn't look so easy."[3]

Since this time a great deal of progress has been made in in individual building blocks of a quantum computer. However, current quantum computers are still in a very primitive state.

1.2 Quantum Computers and Quantum Simulators

Perhaps one of the most convincing arguments that a quantum computer can do something a classical computer cannot is how difficult it is to simulate a quantum computer classically. Even the most powerful classical computer of today attempting to simulate a quantum circuit currently can only simulate a small number of qubits[4]. The current record found in literature is 45 qubits; this many qubits required 0.5 Petabytes of memory to simulate[5]. Since classically computing the dynamics of a quantum system is so hard another approach is needed for such simulations; a quantum approach.

This has naturally led on to the idea of using one quantum system that is easy to control to simulate another quantum system. Currently various quantum simulators are being developed using multiple different methods. One method called boson sampling[6] is considered one of the easiest approaches to creating a working quantum simulator. Boson sampling uses multiple waveguides all linked together with 50/50 beam splitters. Photons are then fed into one end of this system and detectors at the other end measure which waveguide the photons exit from. This builds up a probability distribution for the system, related to the permanent of a matrix, which classically is exponentially difficult to calculate.

Another method drawing a lot of attention is called quantum annealing[7]. Quantum annealing is a method of finding a global minimum energy state of a system. This method works by setting up a large system of qubits in superposition to represent a problem and then adiabatically reducing the energy of the system. The result of this should be a system that is in (or close to) the global minimum energy state. Classically this is hard due to the abundance of local minima present in complicated systems.

Both of these methods are non-universal quantum computers since they can only simulate very specific problems. Such computers are useful tools for developing ideas for what a universal quantum computer might be capable of and are useful as a proof of concept that quantum computing itself is possible. However, a non-universal quantum computer is very limited in terms of what it can simulate. A universal quantum computer should be as programmable as a classical computer but with the ability to run any quantum algorithm without the need to build a new computer for every problem. Several design proposals have been suggested with the goal of realising universal quantum computation. For example, qubits can be physically implemented as superconducting circuits[8], nitrogen vacancy (NV) centers in diamond[9] and using trapped ions[10]. One measurement of how well these regimes perform is called the threshold theorem[11]; this theorem states that error correction can only be achieved if the fidelity of the system is above a certain threshold. Using surface code quantum computing this threshold currently sits at around 99% fidelity[12]. So far using NV centres a 2-qubit gate has been created with a gate fidelity of 88%[13] which puts it below the required fidelity threshold. Whereas,

both super conducting circuits and ion traps are above the threshold with 2 qubit gate fidelities of 99.4%[14] and 99.9%[15], respectively.

Due to its high gate fidelity the Networked Quantum Information Technologies (NQIT) Hub is attempting to build a universal quantum computer using the ion trap technique. The qubits in such a system are formed by the electronic states of the ion [16]. These qubits can be prepared in a desired initial state by a series of laser pulses and then, using photons [10] or phonons [17][18] to enable coherent coupling between qubits, it is possible to build quantum logic gates [19]. Since ion traps are able to contain the ions for long periods of time and ions tend to have a long coherence time this method has been the most successful so far at creating high fidelity logic gates, at 99.9% for a two qubit gate[15]. This ability to write a state to the qubits and build quantum logic gates is the basis for universal quantum information processing.

So far Intel, IBM, and Google have managed to build universal quantum computers with 49[20], 50[21] and 72 qubits[22], respectively, all using superconducting qubits. However, for any useful applications it is estimated that we would need > 150 logical qubits, and for fault tolerant quantum computation we would require $> 10^7$ logical qubits[19]. Due to the increased fidelity of using ion traps NQIT hopes to build a 250 qubit machine known as Q5:50, consisting of 50 logical qubits and 4 error correcting qubits per logical bit, by the end of 2020[23].

1.3 Networking Qubits

Networking spatially separated qubits is necessary at both short distance (∼m length scale), in quantum computation, and long distance (>km length scale), for quantum communication. This allows the system to become entangled to perform computing operations or sending information

An entangled quantum state is a state of multiple quanta or particles where the overall state cannot be described by the parts individually. An example of an entangled state would be[24],

$$|\Phi^+\rangle = \frac{1}{\sqrt{2}} \left[|0\rangle \otimes |0\rangle + |1\rangle \otimes |1\rangle\right], \tag{1.1}$$

this state is now the sum of two tensor products. Notice that here the states of each qubit are dependent on each other i.e. if I started with the Bell state in eq.(1.1) and measured one qubit in the state $|0\rangle$ then the second qubit would be found in the same state. This implies that by measuring one qubit I can instantly know the state of the other qubit no matter how far apart they are. This type of maximally entangled state is one of four possible Bell pairs[25],

$$|\Phi^{\pm}\rangle = \frac{1}{\sqrt{2}}\left[|0\rangle \otimes |0\rangle \pm |1\rangle \otimes |1\rangle\right], \tag{1.2}$$

$$|\Psi^{\pm}\rangle = \frac{1}{\sqrt{2}}\left[|0\rangle \otimes |1\rangle \pm |1\rangle \otimes |0\rangle\right]. \tag{1.3}$$

Entangled states like this allow for quantum teleportation [26], which is required to send quantum information, and superdense coding, which is a method of representing 2 classical bits as a single qubit[25].

Entangling two ions works by interfering the emitted photons of two qubits via a 50:50 beam splitter with detectors at the other 2 outputs. By measuring in the Bell basis it is possible to detect if the two emitted photons had successfully entangled with each other via a 'double click' event. This simultaneous destruction leaves the two qubits in a maximally entangled state [24]. This can be done via free space or an optical fibre. Since the free space option requires direct line of sight of the pulse it can easily be affected by distortions in the atmosphere, misalignment, and objects in the way. Using an optical fibre to guide guide the light should fix most these issues, however extra losses are introduced since we now need to couple the emitted photon into the fibre. The single photon detector efficiency is one of the most limiting factors of entanglement generation. Optical fibre operates at low loss at a wavelength of 1.55μm, and single photon detectors at this wavelength are efficient up to 70% for avalanche photodiodes [27] or 90% for superconducting nanowires[28]. 90% is considered very efficient for a single photon experiment, however when scaling up to a full size quantum computer the overall efficiency quickly falls as the number of required entangled qubits increases. With a small number of qubits this efficiency is fine as one can attempt the entanglement several times. However, as one scales the system up more attempts are needed to prepare the entire system, which results in slower operations allowing the qubits to decohere.

We can strengthen the interaction between the photon and the ion by introducing cavities to the system. This works by placing the qubits into cavities and allowing a single photon pulse to drive interaction between one cavity based qubit through a fibre to the cavity containing the qubit we want to interact with[29][30][31]. Introducing cavities to strengthen the ion-photon interaction is the key to achieving fast processor speeds in the Q5:50 quantum computer [23]. If it is possible to network qubits in this way and achieve near deterministic entanglement we would be able to scale the system down as we would require fewer single photon detectors. By reducing the number of components in a quantum communications channel we would expect to reduce the error simply by reducing the number of instances in which an error may occur as well as reducing the complexity of the implementation.

1.3.1 Long Distance Quantum Communications

One application of long distance quantum networks is Quantum Key Distribution (QKD), which enables a quantum type of encryption that has potential to be the future of secure communication. QKD requires the use of two communications channels to work; one classical and one quantum. The quantum channel is used to transmit quantum states which are prepared by a sender in either one of two conjugate basis sets at random and sent to the receiver. The receiver does not know which basis the bit was prepared in and has to select at random which of the two basis to measure in. The classical communications channel is then used so the sender can tell the receiver what basis the state was prepared in. If both sender and receiver were preparing and measuring in the same basis then the bit is kept otherwise it is discarded. Using this it is possible to detect the presence of a potential eavesdropper by sending a predetermined message: if the receiver measures errors in the message then it is likely that an eavesdropper was also measuring the key and thus altering the state of the sent qubit. If this happens then another key can be generated to attempt the communication again, or they can switch to another communications channel.

Another way to perform QKD uses entangled pairs of photons, distributed in such a way that both parties that wish to communicate each receive one of the pairs. In this regime both parties select which basis to measure in and then communicate what basis was used over the classical channel. If both measured in the same basis then they know that their results are both the same and thus keep the bit.

This means that for long distance QKD we want to be able to send a quantum state over a long distance with minimal decoherence. Currently this has been done over a distance of 1200km using satellites[32], and over 300km using optical fibre [33] with quantum repeaters periodically along the fibre [34].

Another reason we might want to transfer a quantum state over a large distance is networking quantum computers. Since the power of quantum computers scales exponentially as the number of qubits increases, linking two or more small quantum computers will give an extremely large performance boost for certain tasks. This means that linking quantum computers together is an area of great interest[35].

This thesis looks at how fibre-tip optical cavities may be optimally introduced into the design at NQIT to increase the efficiency of entanglement generation in a stable and scaleable way.

1.4 Requirements for Quantum Computing

Building a working universal quantum computer is an extremely difficult task that requires input from many disciplines including Physics, Engineering and Computer Science. The requirements of building such a machine vary depending on the type of quantum computer, however any universal quantum computer will need to improve error correction, gate fidelity, and the number of qubits.

Classical and quantum computers are both susceptible to errors and error correction is the ability to detect and correct when a qubit has flipped. In classical computing error correction can be done in many different ways; one simple method is by introducing an extra parity bit. Assuming we want to send the bits 1001 to another computer we can introduce either odd or even parity checking for error detection, for even parity we would send the information as 0|1001, where the leading bit is the parity bit. Since the number of 1's in the system is even, now if the reviving party obtains 0|1011 they can tell that an error has occurred by noticing that there is an odd number of bits. However, this form of error detection has a set tolerance, if 2 bits had an error then the receiver would not be able to detect that the information was corrupt. This leads on to another important factor, the error tolerance.

To perform any error correction enough of the original information must be present to both detect and correct the error. Using surface code quantum error correction we can currently allow errors per gate operation of around 1%[12]. By improving error correction techniques we may be able to further increase the allowed error in the system. Currently, only ion-traps and superconducting qubits have a high enough fidelity, 99.9%[15] and 99.4%[14] respectively for 2-qubit gates, to allow for error correction. However, NV centres are getting close to this threshold with 2-qubit gate fidelities of 88%[13].

The largest number of qubits achieved in a universal quantum computer today is 72 in a superconducting quantum computer built by Google[22]. The number of qubits in a quantum computer is often cited as a measure of its power. However, in reality the power of a quantum computer comes from the number of logical qubits. In an ideal system all qubits would be thought of as logical qubits, however due to errors introduced in the system, i.e. from decoherence, a number of advanced error correction techniques and fault tolerant systems need to be in place. Since such techniques require extra qubits this means that most of the qubits inside a universal quantum computer as understood today would be used for error correction and fault tolerance[19].

1.4.1 Q5:50 at NQIT

The Networked Quantum Information Technologies (NQIT) hub is part of a large UK national programme to help develop technologies based on quantum principals. The

main goal of NQIT is developing the Q5:50 ion-trap based quantum computer[23]. This machine will be a proof of principle demonstrator showing how we may be able to scale up this device for fault tolerant quantum computing.

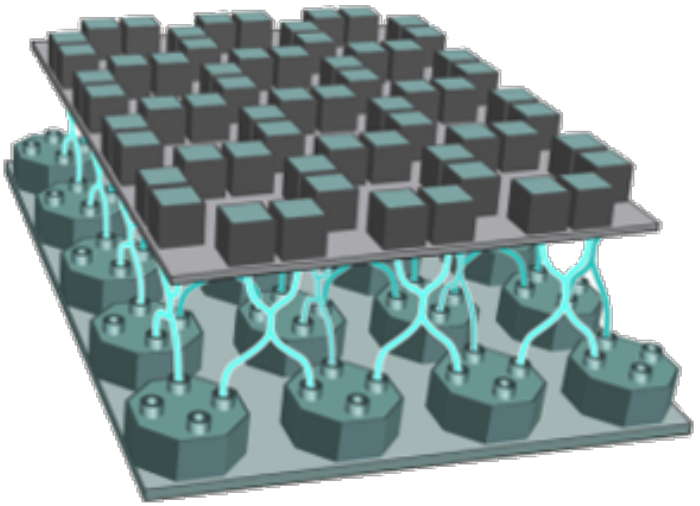

Figure 1.1: NQIT Q20:20 quantum computer was the original NQIT architecture, however since then the design has been altered to the Q5:50 machine[19].

Figure 1.1 shows the old Q20:20 design where the bottom layer contains 20 octagonal boxes each containing 20 qubits in ion traps. Each of these boxes is then connected to its neighbours by fibre or waveguides via a 50/50 beam splitter to interfere the emitted photons. Finally the top layer contains the single photon detectors to both generate the entanglement between traps and confirm entanglement. Currently, the photons are coupled into the fibres via a free space lens set up, however to increase the efficiency of the device it is a good idea to integrate fibre-tip cavities into the design. By doing this we should be able to strengthen the interaction between the optical fibre and the ion, allowing for a more efficient transfer of photons. The ultimate goal of this would be to obtain deterministic transfer which would eliminate the need for the detector layer entirely. However, even if this cannot be reliably achieved, integrating cavities into the system would allow for more efficient transfer making the device faster and reducing errors[23].

Work has already been done looking at the optimal geometry of the ion-trap when a cavity is integrated, including how the cavity length and mirror size affect the system[36][37]. This is important as the dielectric mirror from the cavity can reduce the trapping time of the ion by affecting the radio-frequency trapping potential.

This thesis will look at how the transverse and rotational alignment tolerances for cavities with any arbitrary parameters can be calculated. Due to specific interest in mm length cavities for fibre integrated ion-trap quantum information processing [36] (schematic shown in Figure 2.4) we will apply our methods to this specific case. With the results of this analysis we are then able to determine the optimal trade off between cavity

concentricity and mirror reflectivity for a set cavity length and mirror size to maximise the efficiency of the device and then assess the performance of the optimal results within alignment tolerances. This trade off will allow systems to be designed for optimal light-matter interaction within realistic physical constraints.

Many of the results obtained in this thesis were done in such a way that they could be applied to a large variety of differing cavity experiments. However, for NQIT we restricted the cavity length L and the mirror radius R_{mir} to $1.4mm$ and $70\mu m$, respectively, as this was consistent with literature [36][37] to avoid disturbance of the trapping field.

1.5 Project goals

The NQIT team are hoping to be able to integrate fibre tip cavities into their next design of a quantum computer. As a result the main goals of this project were to look into the feasibility of integrating such cavities under imperfect alignment, and to ascertain the optimal cavity parameters under known constraints. To simplify the problem this thesis will study the simplest possible network shown in Figure 1.2.

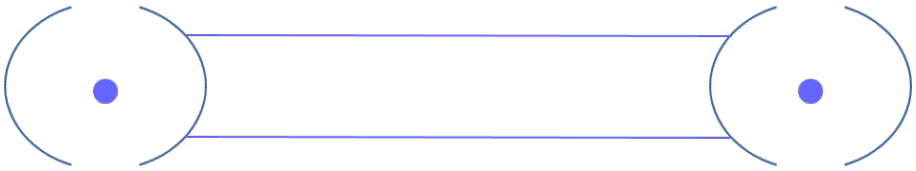

Figure 1.2: Ions in cavities at both ends of a long optical fibre

The device in Figure 1.2 consists of a long optical fibre connecting two distant cavities, where each cavity will contain an ion based qubit. Whilst this simple network is different to the entanglement scheme used by the Q5:50 machine, by optimising this simple network we should be able to find the optimal cavity parameters for the Q5:50 system.

This work builds on the previous work looking at different trap geometries to avoid interference between the cavity mirrors and the ion-trapping time[36][37] by looking at how these constraints affect the ion-cavity system. The constraints required decrease the size of the cavity mirrors and increase the length of the cavity, thereby increasing losses and reducing ion-cavity coupling strengths. This work will look at the best cavity parameters for balancing losses with ion-cavity coupling, the tolerance to fabrication errors and cavity misalignment, and will also explore the potential of asymmetric cavity geometry.

1.6 Thesis summary

This thesis is split up into five main chapters detailing the history, background theory, main research and conclusions of the project.

Chapter 2 will start off by covering the fundamental theory used to build the simulations. The research will then be covered in a chapter focusing on the misalignment of optical cavities, and then a chapter on networking two cavities with an optical fibre.

This thesis covers theory in:-

- Gaussian beam physics
- Quantum Cavity Electrodynamics (QCED)
- Time-reversal symmetry
- Cavity Stability Analysis

Using the above theory the thesis will then split into two distinct chapters 'Misalignment and Optimisation of Ion-Trap Optical Cavities' and 'Ion-Ion state transfer'.

Chapter 3 will look at the properties of fibre-tip optical cavities, then look at the alignment tolerance for any optical cavity with emphasis on the ion-trap information processing. Finally, this chapter will look at the optimal parameters for use in an optical fibre network and how tolerant these parameters are to fabrication error.

Chapter 4 will look at simulating ion-ion state transfer and how by shaping the photon wave function we can increase the chance of successful transfer. By taking the results of chapter 3 we build an atom-cavity-fibre-cavity-atom model of a simple component of a quantum network. Using this model along with the model of the numerical cavity we are able to determine the optimal parameters of a cavity for ion-trap based quantum networks and their robustness to fabrication and experimental errors.

Chapter 5 will go over the thesis conclusions and ideas for how this work can be expanded upon for a future project.

Chapter 2

Fibre-Tip Cavities for Quantum Networks

This chapter will cover the fundamental theory which is the basis for the research in the rest of the thesis. Some of the theory covered here has already been briefly mentioned in the first chapter. However, this chapter will cover the theory in more technical depth.

Quantum cavity electrodynamics is the quantum description of how electromagnetic fields behave when confined into a cavity. The first section will cover the general behaviour of light in cavities, then the second section will cover the quantum mechanical theory of light-matter interaction using a cavity and then the final section will cover how we can shape single photon pulses.

2.1 Cavities

In the context of this thesis a cavity is a structure that is used to confine light. For the fibre tip cavities this is done via reflections from 2 mirrors forming standing waves. A common measure of the performance of a cavity is its Q-factor which describes how 'leaky' a cavity is and can be defined by

$$Q = \frac{\omega_0}{\kappa}, \tag{2.1}$$

where ω_0 is the resonant frequency of the cavity and κ is the cavity decay rate. Since most experiments aim to avoid having a leaky cavity, it is common to desire a high Q-factor. There are three main different types of cavities: Fabry-Perot (FP), Whispering gallery, and Photonic crystal[38].

Whispering gallery resonators use total internal reflection to guide light around a ring structure. This type of cavity has nodes caused by the superposition of forwards and backwards propagating waves[39]. Using this type of structures it is possible to achieve ultra high Q factors in excess of 10^{10} [40]. Whilst these structures can be used to generate entangled photons[41], they are unsuitable for ion-trap based quantum computer design at NQIT as they cannot be used to enhance light-matter interaction for a single atomic qubit.

Photonic crystal cavities usually consist of a large array of periodic holes, with one defect area left without a hole. By doing this one can trap photons in the defect via reflections from the holes. This type of cavity is often used for its very low mode volume[40], with Q factors in excess of 10^7[42]. These cavities have the same issue as the whispering gallery resonators that one cannot easily insert an ion into the cavity to obtain enhanced light-matter interaction.

The main focus of this project is on Fabry-Perot style resonators. This style of cavity is one of the most simple and consists of two mirrors facing each other such that light is forced to resonate between them forming a standing wave. This type of resonator is the most suitable to ion-trap integration as there can be a large gap between the mirrors, which allows extra space to interact with the ion with external lasers and a further distance from the ion-trap to reduce trap distortion. The next subsection will cover this type of cavity in more detail.

2.1.1 Fabry-Perot Cavity

Fabry–Pérot (FP) resonators are basic structures where two mirrors are facing each other, which causes light to be confined via multiple reflections inside the cavity. FP

resonators are used in a large variety of different experiments ranging from the gravitational wave detector LIGO [43] to quantum information processing experiments [16] [44] as a method of increasing the coupling strength [45] of single photon based, 'flying', qubits to an ion based, 'stationary', qubit.

Depending on the application of the cavities they can be used in a variety of different regimes. For example a neutral atom experiment will often use a concentric cavity, as seen in the middle of Figure 2.1, to achieve strong light-matter coupling[44]. This works by focusing the light down to a small point at the center of the cavity. By placing some matter we would like to interact with, such as an ion, at this point we are able to increase the overlap of the light and the matter, thus increasing the interaction strength. Whereas, for applications where we are not aiming to increase the interaction between light and matter, e.g. interferometers, we are more likely to use planar or confocal cavities, as seen at the top and bottom of Figure 2.1, this is because the concentric regime has a higher beam divergence causing the light to spread out much more. This high divergence can cause an increase in losses where light misses the mirror, known as clipping losses. By using confocal or planar regimes we can reduce these losses[43][46].

Whilst concentric cavities are useful for focusing the light to a tight spot for light-matter interaction, they also have one major drawback: stability. Highly concentric cavities are very sensitive to misalignment. One way of analysing this stability is by cavity stability analysis as described next.

2.1.2 Stability Analysis

The stability of geometric rays inside perfectly aligned cavities has been extensively covered in literature [47]. Geometric stability analysis of cavities looks at whether rays inside said cavity are confined within the cavity such that each ray will eventually retrace its initial path. A cavity is considered unstable if the rays diverge such that the width of the path eventually becomes larger than the mirror. The confinement condition for a stable resonator is given by

$$0 \leq \left(1 - \frac{L}{R_1}\right)\left(1 - \frac{L}{R_2}\right) \leq 1, \tag{2.2}$$

where L is the cavity length and $R_{1,2}$ is the radius of curvature of mirrors 1 and 2 respectively [47]. Figure 2.2 shows two different types of cavity set up. The left cavity shows two mirrors placed in a geometrically unstable regime. The right cavity shows two plane mirrors placed in a regime that is at the limit of geometric stability. However, it should be noted that since the size of the mirror is not considered in this analysis it becomes less practical when the size of the mirror is comparable to the beam spot size at the mirror W_m i.e. when clipping losses play a significant role.

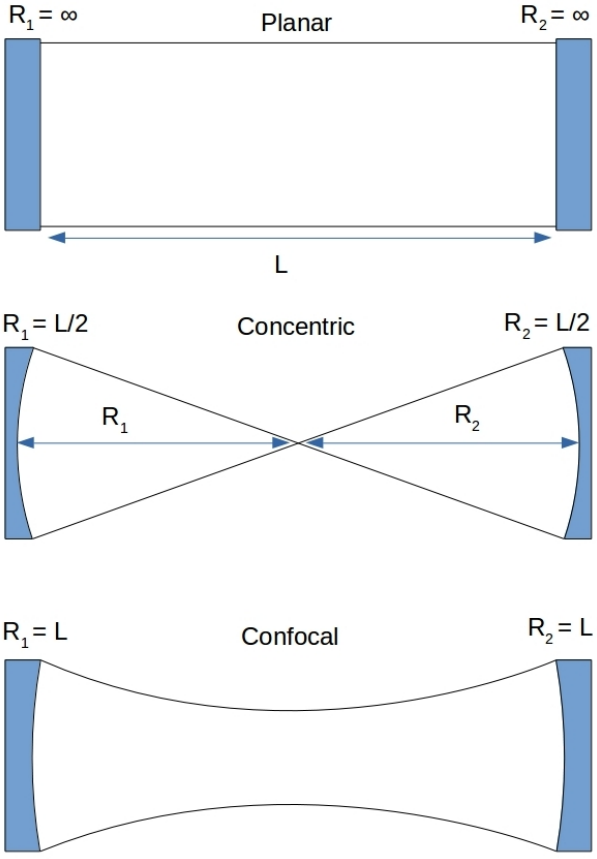

Figure 2.1: This diagram shows three possible FP cavity configurations. The top shows a planar cavity, where the mirrors are both flat. The middle shows a concentric cavity, where the center of curvature of both mirrors is the center of the cavity. The bottom shows a confocal cavity, where the center of curvature for both mirrors is the center of the opposing mirror.

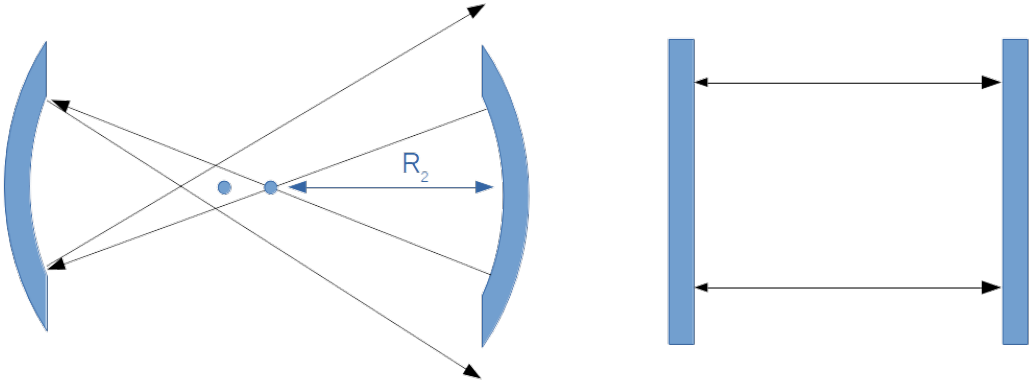

Figure 2.2: Here we see two different cavity configurations with arrows representing rays of light. The left diagram shows a geometrically unstable cavity set up, whereas the right diagram shows a cavity set up at the limit of geometric stability.

To model finite size mirrors with misalignment, geometric stability analysis alone is not

enough, especially when dealing with mirror sizes that are comparable to the beam size at the mirror. To accurately analyse the performance of such a cavity Gaussian beam physics must also be considered.

2.1.3 Gaussian Beam Physics

The fundamental TEM_{00} mode of a cavity with spherical mirrors can be accurately approximated by Gaussian beam physics. However this approximation does worsen slightly as the on-mirror beam size, W_m, increases, with a 99% correlation at a beam size of $W_m = 60\mu$m due to deformation of the end mirrors[48], however in this thesis we will be looking at beam sizes that are well within the high correlation parameters.

The electric field at any given point (x,y,z) of a Gaussian beam can be calculated using [47][49]

$$E = E_0 \left(\frac{W_0}{W(z)}\right) e^{-i[kz-\eta(z)]-r^2\left[\frac{1}{W(z)^2}+\frac{ik}{2R(z)}\right]}, \tag{2.3}$$

where r indicates the distance from the cavity axis defined by $r^2 = x^2+y^2$. The Rayleigh range (Z_0) for the mode in a Fabry–Pérot resonator can be calculated by [47][49]

$$Z_0 = \sqrt{\frac{L(-R_1-L)(R_2-L)(R_2-R_1-L)}{(R_2-R_1-2L)^2}}, \tag{2.4}$$

where R_1 and R_2 are the radius of curvature for mirrors 1 and 2, respectively, and L is the cavity length. The beam waist is given by

$$W_0 = \sqrt{\frac{Z_0\lambda}{\pi}}, \tag{2.5}$$

where λ is the wavelength of the light. These parameters now allow us to calculate the radius of curvature of the beam wave front,

$$R(z) = z\left(1+\frac{Z_0^2}{z^2}\right), \tag{2.6}$$

and the beam size at each point in the cavity

$$W(z) = \sqrt{W_0^2\left(1+\frac{z^2}{Z_0^2}\right)}. \tag{2.7}$$

The spot size on a mirror surface, W_m, is found by setting z as the distance from the beam waist to the mirror surface. For symmetric mirrors this can be simplified to [47]

$$W_m = \left(\frac{\lambda L}{2\pi}\right)^{\frac{1}{2}} \left(\frac{2R^2}{L\left(R - \frac{L}{2}\right)}\right)^{\frac{1}{4}}, \tag{2.8}$$

where $R = R_2 = -R_1$. The Gouy phase, $\eta(z)$, of the beam can be found by

$$\eta(z) = \arctan\left(\frac{z}{Z_0}\right). \tag{2.9}$$

The wave number k is given by

$$k = \frac{2\pi}{\lambda}. \tag{2.10}$$

Figure 2.3 shows a 2D visual representation of a Gaussian beam at $x = 0$.

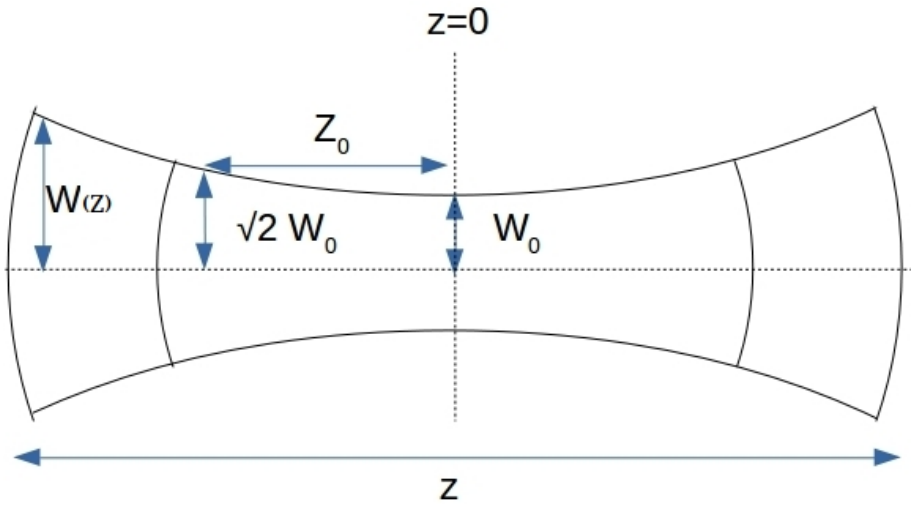

Figure 2.3: A visual representation of a Gaussian beam. The axis along the beam is labelled as the z-axis and a representation of the beam wavefront is shown by curved lines. Here the Rayleigh range (Z_0), beam waist (W_0), beam size at z ($W(z)$) can be seen.

Using the above we can calculate what Gaussian beam we wish to obtain and the mirror parameters that are needed to achieve this beam. By placing two mirrors matching the radius of curvature of the wavefronts of the Gaussian beam and then allowing light between the mirrors it is possible to create an optical cavity with the desired Gaussian beam parameters for our system.

The radius of curvature of the cavity mirrors R_1 and R_2 have to match the radius of curvature of the wavefronts at distances from the beam waist, $z_{1,2}$, thus the radius of curvature of the mirrors can be found via

$$R_1 = z_1 + \frac{Z_0^2}{z_1}, \tag{2.11}$$

and

$$R_2 = z_2 + \frac{Z_0^2}{z_2}. \tag{2.12}$$

These distances are related to the cavity length by

$$L = |z_1| + |z_2|. \tag{2.13}$$

We can use eq. (2.11), eq. (2.12), and eq. (2.13) to determine the distance of the mirror from the beam waist by

$$z_1 = \frac{L(L + |R_2|)}{-|R_1| - |R_2| - 2L}, \tag{2.14}$$

$$z_2 = z_1 + L. \tag{2.15}$$

When symmetric cavities are used (i.e. $R_2 = -R_1$) this distance can be defined by $-z_1 = z_2 = L/2$.

Since our mirrors will be of a finite size but eq.(2.3) decays exponentially, we can already see that there will be some inherent loss associated with any realistic cavity due to the light missing the mirror. This loss is known as a clipping loss, κ. These clipping losses can be calculated via the overlap integral,

$$\rho_{\text{clip}} = \frac{\int\int |E_m|^2 dxdy}{\int\int |E_{tot}|^2 dxdy}, \tag{2.16}$$

where E_m is the electric field on the mirror surface and E_{tot} is the total electric field.

2.1.4 Fibre-Tip Cavities

Quantum information processing uses cavity lengths ranging from $L \sim 10\mu$m with mirror diameters of $D \sim 100\mu$m [45] to $L \sim 10$mm [44] with mirror diameters of $D \sim 10$mm [50]

for neutral atoms and L ~mm and mirror diameters of $D \sim 100\mu$m for ion traps[36]. This means that the stability of FP cavities has a large variation for different cavity parameters and desired performance. Unfortunately, the cavity regimes which focus the cavity mode to a tight beam waist, W_0, are more concentric and thus more unstable from eq.(2.2) and have a larger beam size at the mirror, W_m, as seen in eq.(2.7).

Due to distortion of the electric field of the ion-trap previous work has found that we need mm cavity lengths with $10-100\mu$m scale mirror sizes by dielectric mirrors [36][37]. This is why fibre tip cavities are used; the small profile allows them to be integrated into the trap with as little disturbance to the trapping field as possible, and the fibre allows us to couple photons in and out of the cavity easily. However, eq.(2.5) shows that we desire a concentric cavity, but Section 2.1.2 shows that we want to be in the stable regime and eq.(2.7) shows that we want to have either large cavity mirrors, a more confocal regime, or a shorter cavity length.

For integration into an ion-trap a FP fibre-tip cavity, as seen in Figure 2.4, will be used. This type of cavity is fabricated by cleaving a fibre and using a CO_2 laser to ablate the ends of the fibre to the correct radius of curvature [51]. There are now two options to create high finesse cavity mirrors, firstly we can use a metallic coating such as copper[51] achieving low scattering and absorption losses of 10PPM and 2PPM respectively[52]. Alternatively, we can fabricate a dielectric stack on the ends of the fibre which create a highly reflective mirror known as a distributed Bragg reflector (DBR)[53]. DBR mirrors will be looked at further in Section 2.1.5.

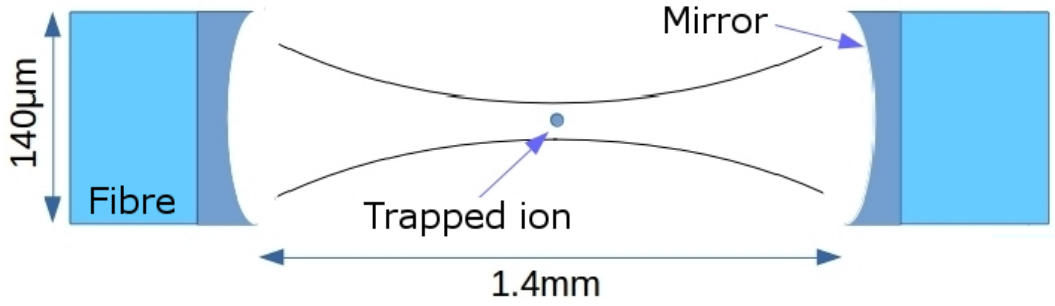

Figure 2.4: Schematic of an ion trapped in a fibre-tip FP cavity.

Unfortunately integrating a cavity into an ion-trap causes the dielectric of the fibres to interfere with the trapping potential and lead to shorter ion trapping times. This issue has been addressed in a previous paper [36]. This paper found that with the right trap geometry and by increasing the cavity length and reducing the amount of dielectric it is possible to reduce the interference on the trapping potential of the ion. Unfortunately, by increasing the cavity length and reducing the size of the mirror the beam waist of the cavity, from eq. (2.5), is reduced and the on-mirror beam size, from eq. (2.7), is increased. This causes a weaker cavity ion interaction and increases the clipping losses. However, this type of cavity still increases the device efficiency compared to collecting the photon using free space optics.

2.1.5 Bragg Mirror

A Quarter Wavelength DBR is a simple structure consisting of periodic dielectrics with alternating refractive indices, as seen in Figure 2.5[54]. The thickness of each layer is chosen to be $\frac{\lambda}{4}$, where λ is the wavelength of light in the material. This creates destructive interference on the other side of the mirror causing a large reflectivity. Each individual layer of the DBR my not be very reflective but the combination of a stack results in high reflectivity[55]. This method of creating a highly reflective cavity mirror has been tested in experiments to produce a reflectivity of >99.999%[56][57].

A Bragg mirror can be fabricated within an optical fibre by using a pulsed laser to create periodic layers of increased refractive index in the silica [58] or by periodic coating of a curved surface. If these layers are created such that the distance between them corresponds to a quarter of the wavelength of the light in that medium then a highly reflective mirror can be fabricated. A boundary between the fibre and cavity constructed in this way can be seen in Figure 2.5.

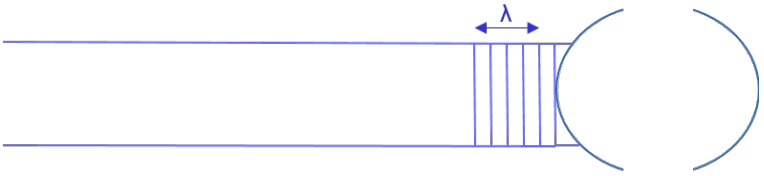

Figure 2.5: Bragg mirror in the fibre (note that the number of layers have been reduced for clarity).

Figure 2.6 shows a zoomed in picture of Figure 2.5 focused at the mirror.

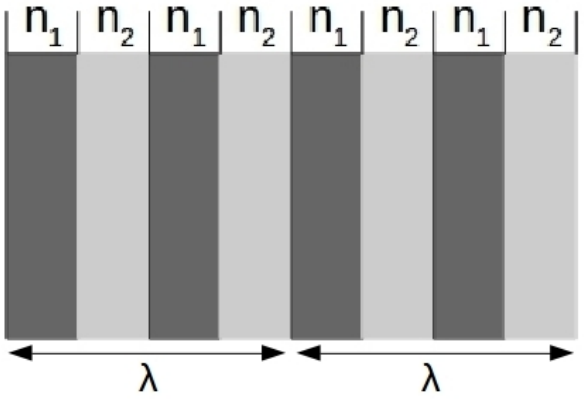

Figure 2.6: A DBR stack with alternating dielectrics of refractive index n_1 and n_2.

This DBR was modelled using Matrix Transfer Theory where each layer alternates between a high and a low refractive index block. The thickness of each block was calculated by the equation

$$d_i = \frac{\pi}{2kn_i}, \tag{2.17}$$

where d_i is the thickness of material i, n_i is the refractive index of material i and k is the wave number. This calculates the thickness of each material layer in the stack that corresponds to $\frac{\lambda}{4}$ in the material for optimal reflection.

In the following, some specific examples of Bragg mirrors are simulated numerically.

Since the refractive indices are λ dependent, the simulations done used the Sellmeier equation for fused silica[59]

$$n^2 = 1 + \frac{0.6961663\lambda^2}{\lambda^2 - 0.0684043^2} + \frac{0.4079426\lambda^2}{\lambda^2 - 0.1162414^2} + \frac{0.8974794\lambda^2}{\lambda^2 - 9.896161^2}. \tag{2.18}$$

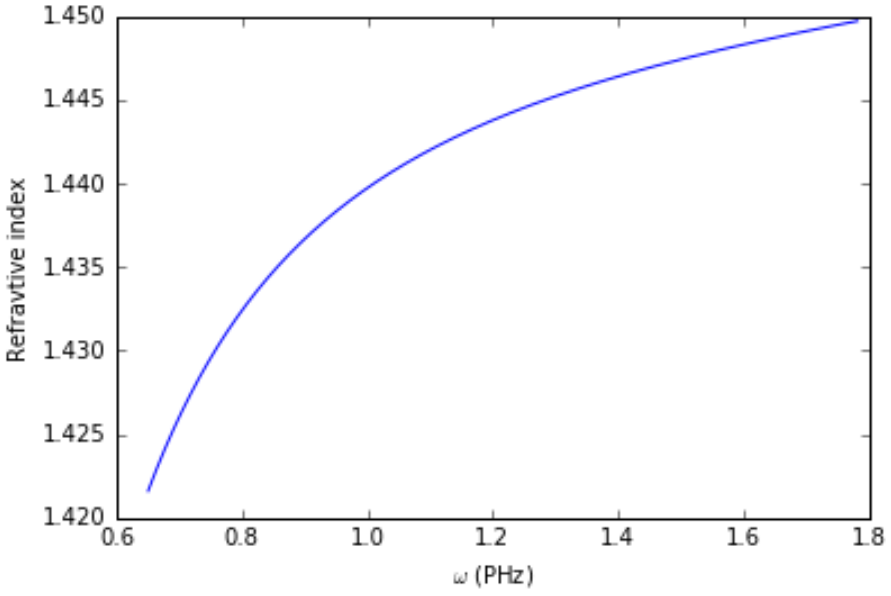

Figure 2.7: Refractive index of fused silica with frequency.

The equation was looked at in terms of frequency to calculate the frequency dependent refractive index profile seen in Figure 2.7. This was done in order to calculate the frequency dependent reflectance of a mirror. For the second material a constant refractive index was used so it may be easily changed for analysis. Two simulations have been looked at where the refractive indices for the second material were 1 (air) and 1.43 respectively. This was done to see how the system behaves with a large and small change in refractive index. By taking the resulting transfer matrix, the reflectivity of the mirror can be determined by

$$R = \left| \frac{m_{21}}{m_{11}} \right| \tag{2.19}$$

where m_{21} and m_{11} are elements in the transfer matrix M [55]. The reflectivity of the DBR can be seen in Figure 2.8.

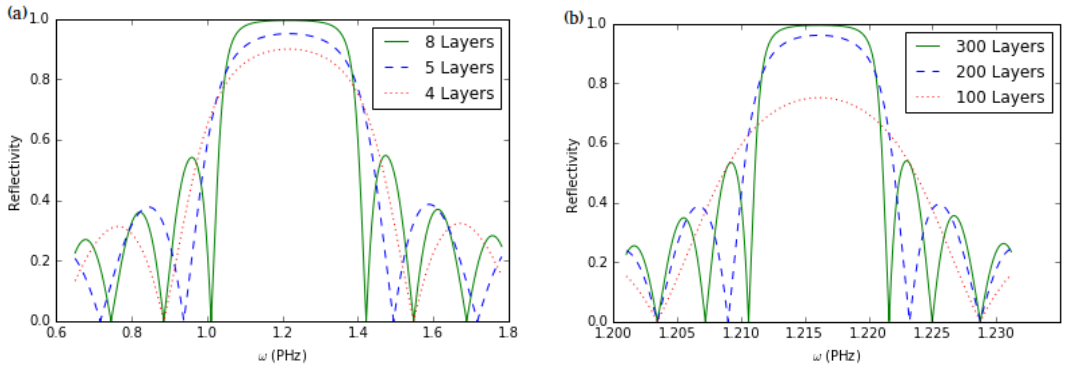

Figure 2.8: Figure (a) shows the reflectance of DBR as a function of frequency where the second material is air with a refractive index of 1. Figure (b) shows the reflectance of DBR as a function of frequency where the second material has a refractive index of 1.43.

These graphs were also plotted as a function of wavelength λ in Figure 2.9.

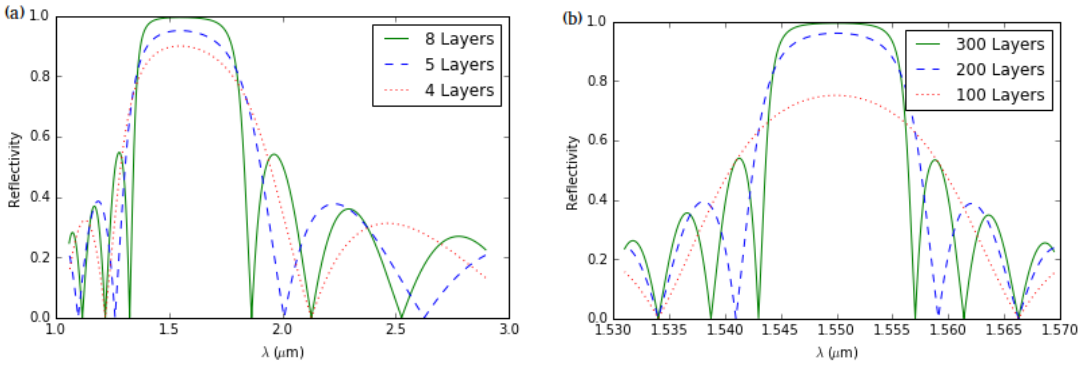

Figure 2.9: Figure (a) shows the reflectance of DBR as a function of wavelength where the second material is air with a refractive index of 1. Figure (b) shows the reflectance of DBR as a function of wavelength where the second material has a refractive index of 1.43.

Here the graphs on the left plot the simulation between air and fused silica and the ones on the right plot some media with a refractive index of 1.43. These values were chosen to see how changing $\Delta n = |n_1 - n_2|$ from large to small values affects the number of layers needed for a highly reflective DBR. This was done in order to see how large the overall length of the DBR would need to be. Note that Figure 2.8 and Figure 2.9 show that the lower the change in refractive index Δn the more layers needed to make a highly reflective DBR. This increase in layers also results in a smaller bandwidth of light being efficiently reflected. The high Δn device is highly reflective over wavelengths of

1.3–1.8μm whilst the low Δn device is only reflective over wavelengths of 1.54–1.56μm (for the 300 layer stack).

The DBR with a refractive index of 1.0000239 (air) as the 2nd material, shown in Figure 2.8(a) and Figure 2.9(a) on the left, shows a device where the thickness of each 2 material layer in the stack is 655.8nm with an overall thickness of the DBR shown in Table 2.1.

Number of Layers	**Total Thickness (μm)**
8	5.25
5	3.28
4	2.62

Table 2.1: The thicknesses of the DBR with air and fused silica.

The DBR with a refractive index of 1.43 as the second material, shown in Figure 2.8(b) and Figure 2.9(b) on the right, show a device where the thickness of each 2 material layer in the stack is 539.3nm and an overall thickness shown in Table 2.2.

Number of Layers	**Total Thickness (μm)**
100	53.93
200	107.87
300	161.80

Table 2.2: The thicknesses of the DBR with fused silica and some material with a refractive index of n=1.43.

As can be seen from Table 2.1 and Table 2.2 the overall thickness of a highly reflective DBR would need to be on the order of μm for a grating with large Δn, or on the order of 100μm for a grating with a small Δn. Since we will be dealing with long single photon pulses in the order of 100 meters with a bandwidth in the order of pm, both of these profiles have a bandwidth that is much larger than needed for our system. However the first method is preferable since it requires fewer layers, this reduces the overall scattering loss from boundary effects.

Now the mirror has been looked at we need to find a method of efficiently coupling light from the cavity into the optical fibre; to do this we can use mode matching optics.

2.1.6 Mode Matching

One issue facing this fibre tip design is that we require a small beam waist for strong coupling. However, without changing the wavelength of light or cavity length the only

way of obtaining such a waist is by increasing the concentricity, shown in eq. (2.5). This however, would result in an increased size of the beam spot on the mirror, shown in eq. (2.7). This now means that we will be attempting to couple a large cavity mode into a smaller single mode optical fibre and this mismatch of mode size causes a decrease in coupling efficiency.

One way of addressing this issue is to use a graded index (or GRIN) lens designed such that the one end is mode matched with the larger cavity mode. The graded index of the lens then acts as a lens focusing the light to match the smaller fibre mode at the other other end. This effect works in both directions, with the light being magnified when travelling through the other way, and should help eliminate inefficiencies due to mode mismatch[60]. A diagram of the mode with and without this lens can be seen in the Figure 2.10.

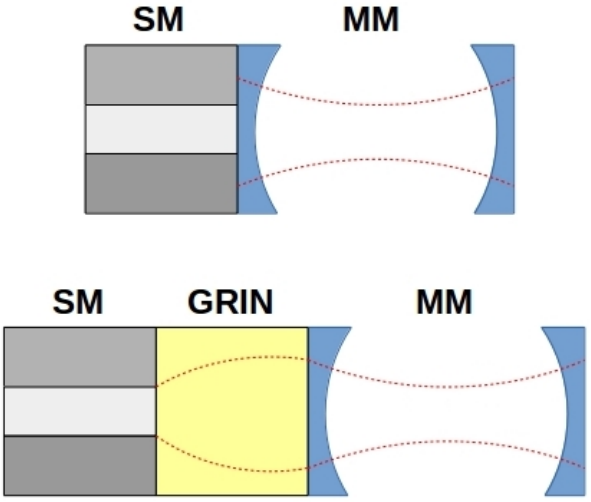

Figure 2.10: The focusing effect of the Graded Index (GRIN) Lens. The top image shows a a single mode fibre with a large mode cavity without a GRIN lens and the bottom picture shows how the system behaves with a GRIN lens. The red dotted lines represent the size of the fundamental mode[60].

In our work we assume that mode matching optics, such as a GRIN lens, are used so that the fibre is mode matched with the cavity. This means that our results assume that a perfectly aligned cavity has 100% coupling efficiency with the optical fibre.

2.2 Cavity-Atom-Photon Interactions

This section we will look at how by using a cavity we can enhance light-matter interactions. We will cover the basic quantum mechanical description of a cavity, the Jaynes-Cummings model, and different cavity regimes.

2.2.1 Jaynes-Cummings Model

The simplest model of an atom trapped in a cavity with a single photon is known as the Jaynes-Cummings model[61], which describes the physics of a 2-level atom inside an optical cavity with a light field. This model is an excellent starting point for our ion-cavity-photon interactions.

The Hamiltonian for the Jaynes-Cummings model in the rotating wave approximation is [62]

$$\hat{H} = \hbar\omega_c \hat{a}^\dagger \hat{a} + \frac{1}{2}\hbar\omega_a \hat{\sigma}_z + \hbar g \left(\hat{a}^\dagger \hat{\sigma}_- + \hat{a}\hat{\sigma}_+\right). \tag{2.20}$$

Here ω_c is the cavity frequency and ω_a is the transition frequency of the 2 level atom. $\hat{\sigma}_z$ is the operator of the population difference between the ground state $|g\rangle$ and the excited state $|e\rangle$ of the 2 level atom defined by $\hat{\sigma}_z = |e\rangle\langle e| - |g\rangle\langle g|$. $\hat{\sigma}_+$ and $\hat{\sigma}_-$ are the raising and lowering operators of the atom respectively. $\hat{a}^\dagger$ and $\hat{a}$ are the photon creation and annihilation operators of the cavity field. g is the coupling strength between the cavity field and the atom. The Hamiltonian shown in eq. (2.20) describes a closed system. A method of analysing an open quantum system is to use the Lindblad equation in the form [63]

$$\dot{\rho} = -\frac{\mathrm{i}}{\hbar}\left[\hat{H}, \hat{\rho}\right] + \hat{L}\left(\hat{\rho}\right), \tag{2.21}$$

where

$$\hat{L} = \sum_n \frac{1}{2}\left[2\hat{C}_n\hat{\rho}(t)\hat{C}_n^\dagger - \hat{\rho}(t)\hat{C}_n^\dagger\hat{C}_n - \hat{C}_n^\dagger\hat{C}_n\hat{\rho}(t)\right], \tag{2.22}$$

and the collapse operators $\hat{C}_n$ are given by

$$\hat{C}_n = \sqrt{\gamma_n}\hat{O}_n, \tag{2.23}$$

where $\gamma_n = \gamma, \kappa$ are the rates of collapse for the operators $\hat{O}_n = \hat{\sigma_-}, \hat{a}$. This system now describes a 2 level atom inside a leaky cavity and with spontaneous atomic decay. Figure 2.11 shows a diagram of the basic Jaynes-Cummings system.

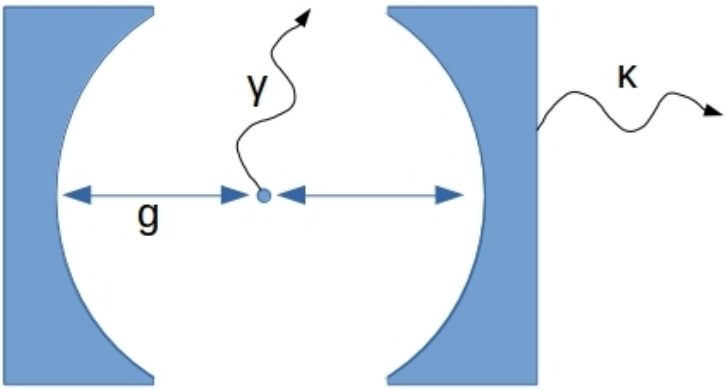

Figure 2.11: The Jaynes-Cummings model describes the interaction between a single atom and a photon inside an optical cavity. Here g is the coupling strength between the cavity and the atom, κ is the cavity decay rate, and γ is the atom spontaneous decay rate.

The cavity shown in Figure 2.11 has two main mechanisms for loss, one is the cavity decay rate, κ, and the other is the spontaneous decay rate of the atom γ.

2.2.2 Cavity Coupling Regimes

The Jaynes-Cummings model as seen in Figure 2.11 is typically operated in three different regimes:

- Strong coupling, where $g \gg \kappa, \gamma$. Here the atom-cavity coupling is much stronger than the associated losses. This results in pronounced photon absorption-emission-reabsorption oscillations known as Rabi oscillations.
- Weak coupling, where $g \ll \kappa, \gamma$. Here the system is dominated by losses and the Rabi oscillations are suppressed.
- Bad cavity (or fast cavity), where $\kappa > g > \gamma$. In this regime the atom still interacts relativity strongly with the cavity, meaning that an atom in the excited state is more likely to emit into the cavity than free space. However, since κ is the dominant loss, the photon is likely to be lost through the cavity before it can be reabsorbed. This regime is known as 'fast' when the dominant cavity loss is transmission, or 'bad' when the dominant cavity losses are the intrinsic losses (i.e. absorption, scattering, clipping etc)[64].

In this thesis we are most interested in the strong coupling regime. However, when looking at devices which yield large light-atom coupling strengths, g, we find that a small beam waist, W_0, is desired from the dipole coupling [45]

$$g = \frac{\lambda}{\pi W_0}\sqrt{\frac{3c\gamma}{L}}, \tag{2.24}$$

where c is the speed of light. As can be seen from eq. (2.24), the coupling strength, g, of the atom-cavity system is dependent on the cavity length, L, the spontaneous decay rate, γ, the wavelength of light, λ, and the beam waist, W_0. Since we are integrating this cavity into an ion trap this system will have set constraints on all of these variables. Only the beam waist, and by extension the cavity concentricity, can be adjusted to obtain a large atom-cavity coupling strength. This results in a desire for highly concentric cavities. Unfortunately highly concentric cavities have a lower tolerance to misalignment (as will be discussed in chapter 3) and also a larger on-mirror spot size, W_m.

2.3 Optical Fibres to Network FP Cavities

This section will cover how we can use an optical fibre to network cavities and thus ions together to build a quantum network. It will cover how the fibre was modelled for this project and the motivation behind using a fibre network in both quantum computing and quantum communications along with the requirements for both systems and then an in-depth analysis of the constraints set by the NQIT design.

2.3.1 Short Fibre Limit

When networking cavities with optical fibre several papers discuss a simplification known as the short fibre limit, where the fibre is short enough that it can be treated as if it were a simple single mode cavity coupled to the cavities eitherside of it. The condition for a fibre being this small is [65] [31]

$$\frac{l\Gamma}{\pi c} \leq 1, \tag{2.25}$$

where l is the length of the fibre and Γ is the cavity line width. Using the mode spacing $\Delta\omega = \frac{c\pi}{l}$, this is equivalent to

$$\Gamma\frac{1}{\Delta\omega} = \Gamma\frac{l}{c\pi} \leq 1. \tag{2.26}$$

Comparing this to eq. (2.57) we can see that

$$\frac{\Gamma^2}{\eta^2} \leq 1, \tag{2.27}$$

where η is the decay rate into a single fibre mode. This shows that the short fibre limit holds while the cavity line width is smaller than the decay into a single mode. As a result in this limit only one resonant mode of the fibre significantly interacts with the cavities. A 2012 paper by E.Kyoseva et al[29] covers the connectivity of cavity networks using short fibres such that fibre modes can be eliminated. This paper however looks at a system that is on the limit of this short fibre condition. Doing so they considered the fibre as a third cavity containing few modes. Doing this it is possible to study the full dynamics of the system with the interaction Hamiltonian

$$H_{fib} = \sum_k \frac{1}{2}\hbar J[a_{1k}^\dagger a_{2k} + H.c.], \tag{2.28}$$

$$H_{fib-cav} = \sum_{i=1,2} \sum_{k} \hbar g_{ik} e^{i(\omega_c - \omega_k)t} a_{ik}^{\dagger} c_i + H.c. \tag{2.29}$$

In this model i represents either cavity 1 or 2 respectively, where c_i is the cavity annihilation operator. a_{1k} and a_{2k} are the annihilation operators of photons travelling right and left in the fibre respectively and k indicates a mode of a photon in the fibre. In the limit where coupling between fibre modes $J \gg g$, i.e. where the mirror is highly reflective, very little of the photon is in the fibre at any given point. This allows for the adiabatic elimination of fibre modes via the introduction of an effective coupling strength

$$J_{\text{eff}} = -\frac{1}{J} \sum_{k} g_{1k}^{\star} g_{2k} \tag{2.30}$$

leading to a simplified effective Hamiltonian[29]

$$H_{eff} = 2J_{eff} c_1^{\dagger} c_2 + H.c.. \tag{2.31}$$

Since this model is right on the edge of the short fibre limit it is a good starting point for understanding how the length of a fibre affects the dynamics of the system, however these simplifications are not valid for a long fibre[30].

In 1997 T.Pellizzari analysed a similar atom-cavity-fibre-cavity-atom network to the one we are considering in this thesis[30]. This paper analysed the probability of successful state transfer from one atom to another as a function of the fibre length. It concluded that state transfer is almost perfect at short fibre lengths but as the length increases and more possible modes are introduced the efficiency of the system deteriorates rapidly. As a result this paper showed that the simplifications of short fibre limit break down as longer optical fibres are considered.

2.3.2 Modelling a Long Optical Fibre

In order to model the system shown in Figure 1.2 we can start by looking at the optical fibre. Since the optical fibre has a highly reflective mirror at each end it can be seen as a Fabry–Pérot (FP) cavity. The system of interest is one where the fibre is sufficiently long such that the photon can leak out of cavity A and be completely contained within the fibre before reaching cavity B. Any photon pulse in the fibre is clearly defined by standing waves with a node at each of the mirrors. The diagram in Figure 2.12 shows how the standing wave modes of a long cavity would look.

The electric field of these longitudinal modes can be written as

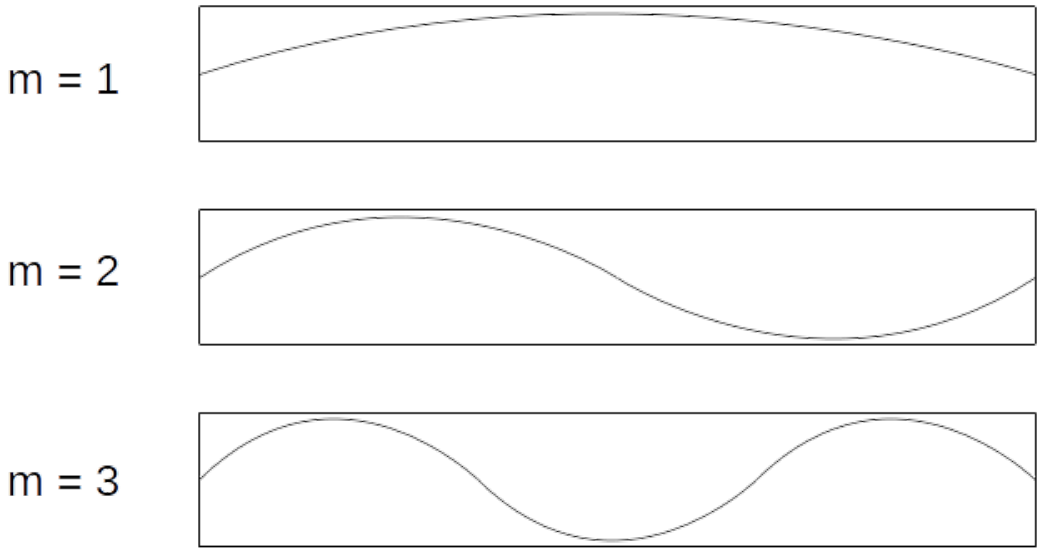

Figure 2.12: Longitudinal modes in a fibre

$$E_m = E_{m0} \sin\left(\frac{\pi m x}{l}\right) \tag{2.32}$$

where the mode number m is an integer and relates to the wavelength λ by

$$m = \frac{2ln}{\lambda} \tag{2.33}$$

with l being the length of the fibre and n being the effective index of the fibre. Since the energy of an electric field can be written as

$$U_e = \int_{-\infty}^{\infty} \frac{1}{2}\epsilon_0 |E|^2 dV \tag{2.34}$$

where ϵ_0 is the permittivity of free space and V is volume, and the energy of a photon can be written as

$$U_p = \hbar\omega \tag{2.35}$$

where $\omega = 2\pi c/\lambda$ is the frequency of the photon and $\hbar$ is the reduced Planck constant, we can normalise the electric field amplitude E_{m0} for a single photon by using eq. (2.34) and eq. (2.35),

$$E_{m0} = \sqrt{\frac{2\hbar\omega}{\epsilon_0 \pi r^2 l}}. \tag{2.36}$$

Here V has been replaced with $\pi r^2 l$ where r is the transverse mode field radius of the fibre and l is the fibre length.

A pulse in this system can now be written as a superposition of these longitudinal modes,

$$E(x) = \sum_m c_m E_m(x) \tag{2.37}$$

with c_m being a coefficient to show the amplitude of the field in mode m. Assume we are looking at a wavelength λ of 1.55μm, a refractive index n of 1.5, and a fibre length of 300m then using eq. (2.33) we can calculate the corresponding mode number m_0 to be 5.8×10^8 to 2 significant figures. This mode number corresponds to the central frequency of the pulse of 1.55μm wavelength light. Taking the Fourier transform of this pulse we would find a range of frequencies. As a result a detuning is introduced such that $m = m_0 + m_k$ where

$$m_k = k - \frac{n_k}{2}, \quad k \in \mathbb{Z} : 0 \leq k \leq n_k \tag{2.38}$$

Here m_k is the detuned mode number and n_k is the overall number of modes we are interested in, and is chosen by the number of significantly coupled modes[30]. Since modes further away from the central mode are less likely to contain significant population modes further away than n_k are ignored to save computing time. Now the light inside the fibre can be written as a sum of sine waves in the form

$$E(x) = \sum_{k=0}^{n_k} c_k E_{k0} \sin\left(\frac{\pi(m_0 + m_k)x}{l}\right). \tag{2.39}$$

By squaring this and substituting into eq. (2.34) we end up with

$$U_e = \hbar \sum_k \omega_k |c_k|^2 \tag{2.40}$$

Here ω_k is the frequency of the kth mode and $|c_k|^2$ describes its population. In a quantum system this is replaced with the quantum mechanical number operator,

$$\hat{N_k} = \hat{c_k}^\dagger \hat{c_k}. \tag{2.41}$$

This replaces the classical coefficients c_k^* and c_k with the quantum creation and annihilation operators $\hat{c_k}^\dagger$ and $\hat{c_k}$ respectively, and we can now describe the energy of the system by the Hamiltonian

$$\hat{H} = \hbar \sum_k \omega_k \hat{c_k}^\dagger \hat{c_k} \tag{2.42}$$

which is the sum of harmonic oscillators. Here the creation and annihilator operators, $\hat{c_k}^\dagger$ and $\hat{c_k}$, obey the bosonic commutation relations

$$[\hat{c_a}, \hat{c_b}^\dagger] = \delta_{ab}, \qquad [\hat{c_a}, \hat{c_b}] = [\hat{c_a}^\dagger, \hat{c_b}^\dagger] = 0. \tag{2.43}$$

2.3.3 Connecting the Cavities

Now a Hamiltonian for the fibre has been created we can look at the cavities. If we assume the cavities to be single mode harmonic oscillators then we can write the Hamiltonians as

$$\hat{H_i} = \hbar \omega_i \hat{i}^\dagger \hat{i} \tag{2.44}$$

where $i = a, b$ indicate the cavity on the left and the cavity on the right respectively. The next step is to create the interaction Hamiltonian. Both the electric field of the cavity $\hat{E}_{cav}$ and the electric field of the fibre interact through the dipole $\hat{d}$ of the mirror like so:

$$\hat{H}_{int} = \hat{d} \cdot \hat{E}_{cav} + \hat{d} \cdot \hat{E}_{fib}. \tag{2.45}$$

Assuming that this interaction is fast enough that it can be considered instantaneous, the dipole can be adiabatically eliminated and the interaction can be written as

$$\hat{H}_{int} = \hat{E}_{cav} \cdot \hat{E}_{fib}. \tag{2.46}$$

Combining the electric field of the cavity and fibre modes in this way leads to an interaction Hamiltonian in the form

$$\hat{H}_{int} = \hbar \sum_k \sum_{i=a,b} \eta_i (\hat{c_k} + \hat{c_k}^\dagger)(\hat{i} + \hat{i}^\dagger) \tag{2.47}$$

where η is some coupling strength determined below. Expanding this out gives

$$\hat{H}_{int} = \hbar \sum_k \sum_{i=a,b} \eta_i (\hat{c_k}\hat{i} + \hat{c_k}\hat{i}^\dagger + \hat{c_k}^\dagger \hat{i} + \hat{c_k}^\dagger \hat{i}^\dagger) \tag{2.48}$$

Using the rotating wave approximation (RWA)[66] we can discard the $\hat{c_k}\hat{i}$ and $\hat{c_k}^\dagger\hat{i}^\dagger$ terms. This is because the time evolution operator of this system can be defined by

$$\hat{U} = e^{-\frac{i\hat{H}t}{\hbar}} \tag{2.49}$$

Therefore $\hat{c_k}\hat{i}$ evolves with a frequency

$$e^{-i(\omega_k+\omega_i)t} \approx e^{-2i\omega t} \tag{2.50}$$

and $\hat{c_k}^\dagger\hat{i}^\dagger$ evolves with

$$e^{i(\omega_k+\omega_i)t} \approx e^{2i\omega t} \tag{2.51}$$

where as $\hat{c}_k\hat{i}^\dagger$ evolves with

$$e^{i(\omega_i-\omega_k)t} \approx e^{-i\Delta\omega t} \tag{2.52}$$

and $\hat{c}_k^\dagger\hat{i}$, evolves with

$$e^{i(\omega_k-\omega_i)t} \approx e^{i\Delta\omega t}. \tag{2.53}$$

Taking $\omega \approx \omega_k \approx \omega_i$ for this example. Since ω is extremely large at the wavelengths of interest, we can say that terms where we have 2ω will be oscillating extremely fast compared to the terms dependent on $\Delta\omega$ as $2\omega \gg \Delta\omega$. Since

$$\int e^{i\omega t}dt = \frac{e^{i\omega t}}{i\omega} \approx 0 \tag{2.54}$$

for large values of ω. These fast oscillations will have very little effect on the interaction of the systems and thus can be ignored. Note that this approximation breaks down if there is another evolution happening to the system on the time scale associated with the 2ω terms. This leaves an interaction Hamiltonian in the form

$$\hat{H}_{int} = \hbar\sum_k\sum_{i=a,b}\eta_i(\hat{c_k}\hat{i}^\dagger + \hat{c_k}^\dagger\hat{i}). \tag{2.55}$$

Since the fibre is calculated via the sum of many discrete modes we can relate the coupling strength η to the cavity line width Γ using Fermi's golden rule[67],

$$\Gamma_{i\to c_k} = \frac{2\pi}{\hbar}|\langle c_k|\hat{H}_{int}|i\rangle|^2\rho. \tag{2.56}$$

For our basic model we can assume that η is the same for all fibre modes and we obtain

$$\Gamma = 2\pi\hbar|\eta|^2\rho \tag{2.57}$$

where ρ is the density of states defined by

$$\rho = \frac{1}{\Delta E}. \tag{2.58}$$

In our case the energy spacing ΔE is defined by

$$\Delta E = \hbar\Delta\omega = \hbar c\Delta k = \frac{\hbar c\pi}{l}, \tag{2.59}$$

therefore

$$\rho = \frac{l}{\hbar c\pi}. \tag{2.60}$$

So now the coupling strength to an individual mode η can be defined by

$$\eta = \sqrt{\frac{\Gamma c}{2l}} \tag{2.61}$$

The Hamiltonian for the basic system can therefore be written as

$$\hat{H} = \hbar\omega_a\hat{a}^\dagger\hat{a} + \hbar\omega_b\hat{b}^\dagger\hat{b} + \hbar\sum_k \omega_k\hat{c_k}^\dagger\hat{c_k} + \hbar\eta_a\sum_k(\hat{a}\hat{c_k}^\dagger + \hat{c_k}\hat{a}^\dagger) + \hbar\eta_b\sum_k(\hat{b}\hat{c_k}^\dagger + \hat{c_k}\hat{b}^\dagger)(-1)^k \tag{2.62}$$

where the $(-1)^k$ term in eq. (2.62) is due to even modes being symmetric and odd modes being antisymmetric. This means that the fibre couples to the two cavities modes with different phases. Note that this Hamiltonian can also be found in literature[30].

Since ω is on the order of $\sim$ 100THz it is convenient to introduce a rotating frame. Since we know that the operators evolve such that

$$\hat{\chi}(t) = \hat{\chi}(0)e^{-i\omega t} \tag{2.63}$$

we can introduce the rotating frame such that the operators are now defined by [68]

$$\hat{\chi}_{rf} := \hat{\chi} e^{i\omega_{rf} t} \tag{2.64}$$

where ω_{rf} is the rotating frame frequency, and is usually chosen to be the resonant frequency of the cavity. Doing this we introduce a detuning $\Delta = \omega - \omega_{rf}$. This allows for the system to be simulated in a significantly more efficient way and by dropping the rf notation the Hamiltonian can be rewritten as

$$\hat{H} = \hbar\Delta_a \hat{a}^\dagger \hat{a} + \hbar\Delta_b \hat{b}^\dagger \hat{b} + \hbar \sum_k \Delta_k \hat{c_k}^\dagger \hat{c_k} + \hbar\eta_a \sum_k (\hat{a}\hat{c_k}^\dagger + \hat{c_k}\hat{a}^\dagger) + \hbar\eta_b \sum_k (\hat{b}\hat{c_k}^\dagger + \hat{c_k}\hat{b}^\dagger)(-1)^k \tag{2.65}$$

This covers modelling the basic system of two cavities connected by a long fibre. By also considering the Jaynes-Cummings model in eq. (2.20) to add atoms into the cavities, we have obtained the model we will be using as the backbone of the system this thesis analyses.

2.4 Pulse Shaping

Since the goal of this project is networking ions it is important to consider the absorption of the single photon pulse by the second cavity. The motivation to shape a single photon pulse is to maximise this absorption and by extension the overall efficiency of the transfer.

In this section I will cover some techniques that may be used to shape a single photon pulse. Extra focus will be given to shaping a photon using a laser to drive the population of a 3-level atom.

2.4.1 Pulse Shaping Using a Laser

One method of shaping an emitted photon is called Stimulated Raman Adiabatic Passage (STIRAP) [69] [70]. This method uses a 3-level atom with a Λ structure seen in Figure 2.13. This atom is placed inside a cavity where it is being driven by a laser.

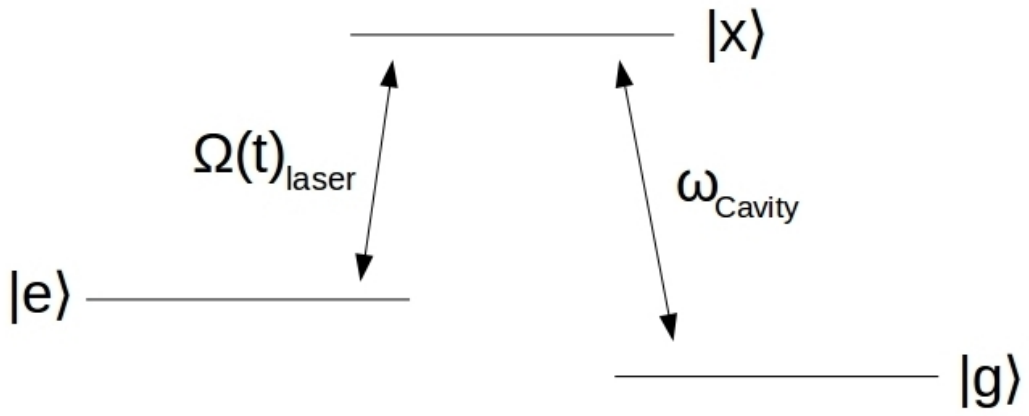

Figure 2.13: Energy levels for the atom cavity system.

If $|g\rangle \leftrightarrow |e\rangle$ is a forbidden transition and the cavity is tuned to ω_{cavity}, corresponding to the $|g\rangle \leftrightarrow |x\rangle$ transition, then we can take an atom in the initial state $|e\rangle$ and by driving the $|e\rangle \leftrightarrow |x\rangle$ transition with a laser, with a Rabi frequency $\Omega(t)_{laser}$, it is possible to shape the photon emission pulse. This works since we are controlling the $|x\rangle$ population thus controlling the emission corresponding to the $|x\rangle \rightarrow |g\rangle$ transition. By doing this with the right $\Omega(t)_{laser}$ it is possible to create a single photon pulse in the desired shape as it is being emitted.

To calculate the laser pulse required to obtain a desired single photon emission pulse we consider only the states $|e,0\rangle$, $|x,0\rangle$, and $|g,1\rangle$, corresponding to the atomic state and the cavity population, where the number of photons $n = 1$, where the probability amplitude of each state is given by

$$c(t) = \begin{bmatrix} c_e(t) \\ c_x(t) \\ c_g(t) \end{bmatrix}. \tag{2.66}$$

By initialising the atom completely in the excited state $|e,0\rangle$ and considering the decay rate of the cavity, κ, and spontaneous decay rate of the atom, γ, we can obtain the dynamics of the system [71]

$$i\hbar\frac{d}{dt}c(t) = -\frac{\hbar}{2}\begin{pmatrix} 0 & \Omega(t) & 0 \\ \Omega(t) & 2i\gamma & 2g \\ 0 & 2g & 2i\kappa \end{pmatrix} c(t). \tag{2.67}$$

The probability amplitude of the output pulse, $\psi(t)$ is linked to the probability amplitude of $|g,1\rangle$ via its decay rate κ. Also, the cavity coupling strength, g, and Rabi frequency of the driving laser, $\Omega(t)$, clearly link the $|g,1\rangle \leftrightarrow |x,0\rangle$ and $|x,0\rangle \leftrightarrow |e,0\rangle$, respectively. To solve the system for the desired laser pulse, $\Omega(t)$, we can use the equations

$$c_g(t) = \frac{\psi(t)}{\sqrt{2\kappa}}, \tag{2.68}$$

$$c_x(t) = -\frac{i}{g}\left(\dot{c}_g(t) + \kappa c_g(t)\right), \tag{2.69}$$

$$\Omega(t)c_e(t) = 2\left(i\dot{c}_x(t) + i\gamma c_x(t) - g c_g(t)\right). \tag{2.70}$$

By also taking into account the conservation of energy in the system with the decay rates κ and γ we can find the expression[71]

$$|c_e(t)|^2 = 1 - |c_x(t)|^2 - |c_g(t)|^2 - \int_0^t dt\left(2\gamma|c_x(t)|^2 + 2\kappa|c_g(t)|^2\right). \tag{2.71}$$

By combining eq. (2.70) and eq. (2.71) we can find a function which calculates the desired laser pulse, $\Omega(t)$, to create any arbitrary photon pulse shape, $\psi(t)$,

$$\Omega(t) = \frac{2\left(i\dot{c}_x(t) + i\gamma c_x(t) - g c_g(t)\right)}{1 - |c_x(t)|^2 - |c_g(t)|^2 - \int_0^t dt\left(2\gamma|c_x(t)|^2 + 2\kappa|c_g(t)|^2\right)}.\text{[71]} \tag{2.72}$$

Shaping a photon waveform via STIRAP has been achieved experimentally with a $40Ca^+$ ion inside a integrated fibre cavity - RF trap system [72]. This was done with a single-photon efficiency of $(8.0 \pm 1.3)\%$ which agrees with the theoretical model for that particular system [73].

A few different papers have looked at different methods of shaping a single photon pulse. One such method developed by V. Averchenko, D. Sych, and G. Leuchs[74][75] shows a method of shaping a photon pulse without interacting with it. This method uses 2 photons that are entangled with each other calling one the signal and the other the idler. The idler photon is passed through a temporal modulator to shape it into the desired shape in a probabilistic way in the time domain. The idler is then passed to a detector measuring in the frequency domain for the conjugate of the desired shape. If the detector has a 'click' event then we know that the signal photon has been successfully shaped without loss.

Now we can shape any arbitrary pulse, we can look at which shapes are the most efficient for the ion-cavity-fibre-cavity-ion network. A good starting point would be to look at the efficiency of a shape that is the time reverse of the emitted photon.

2.4.2 Time Reversal

If a single photon is placed into a cavity and allowed to spontaneously decay into a long fibre such that the entire pulse will be contained in the fibre, the pulse shape looks like a decaying exponential as can be seen in Figure B.1(a). M. Stobinska et al. [76] argue that a time reverse pulse should allow for perfect reabsorption.

The time reversal argument follows that most real world systems are in constant contact with the environment. This allows for information about the system to be lost causing them to be irreversible. A quantum system where environmental effects are limited or the system is closed, however, should be able to be traced back to its initial state from a time evolution of that state by applying the right operator. This means we can find the time reverse of the emitted pulse by using these arguments from a 2004 paper by S. Stenholm and M. Jakob [77] and a 2012 paper from G. Leuchs and M. Sondermann [78] and use this to create perfect absorption. So assuming the time evolution of a system is given by

$$A(t) = A(0)e^{-i\theta t} + A^*(0)e^{i\theta t} \tag{2.73}$$

then the time reverse of this is[77]

$$A_{flipped} = A(-t) = A(0)e^{i\theta t} + A^*(0)e^{-i\theta t}. \tag{2.74}$$

Using the time reverse of the emitted pulse as seen in Figure B.1(b) has been shown to have near 100% absorption[76]. Since the shape of the photon pulse is so important in this system a paper by Y. Wang in 2011 [79] has discussed the absorption of a photon into a cavity given a variety of different pulse shapes. This paper has shown 99.5% and 54% absorption for the time reverse and natural pulses respectively. More interestingly though they have shown high absorption in other shapes such as 80% for a Gaussian. This shows that it is possible to aid the absorption of a single photon by shaping its pulse shape, thus aiding in state transfer[80].

2.4.3 Shaping with Time Reversal in Mind

Using the previous two subsections it is possible to also drive the absorption of the second cavity to allow for almost complete photon absorption[71][81]. This was achieved experimentally by S. Ritter et al. using rubidium atoms trapped in an optical dipole trap in the center of a high finesse optical cavity and generating a near time-symmetric envelope. This paper used 60m of optical fibre to entangle distant atoms with 98% fidelity and transfer quantum information between the two atoms with 84% fidelity [82].

To achieve as high as possible transfer we require a strong coupling strength, g, and mirrors with low scattering and absorption losses. Another factor which affects this transfer is accurately positioning the atom at the beam waist. However, for the purposes of this thesis we assume that the atom is placed perfectly at the beam waist.

In this thesis rather than calculating the laser pulse required for absorbing any arbitrary photon, we instead use the time reverse of the laser pulse used to create the initial photon. This ultimately results in efficient transfer between two distant trapped ions, as seen in Figure 1.2.

Chapter 3

Misalignment and Optimisation of Ion-Trap Optical Cavities

This chapter uses ray tracing techniques and Gaussian beam optics to help derive the geometry of the fundamental cavity mode, and thus its location on the cavity mirrors, under various misalignments. Using this geometry we will then perform a numerical analysis of the performance of fibre tip optical cavities, with the parameters shown in table 3.1, under misalignment. We also look at how two different size cavity mirrors could provide a useful solution to misalignment sensitivity, the misalignment sensitivity of neutral atom experiments, and what cavity parameters are optimal for efficient ion-cavity-fibre-cavity-ion photon transfer.

Parameter	**Symbol**	**Value**
Cavity Length	L (mm)	1.4
Mirror Radius	R_{mir} (μm)	70
Concentricity	δ	0.0166
Wavelength	λ (nm)	866

Table 3.1: Parameters of the the fibre tip cavities used in this chapter.

Section 3.1 starts off looking at perfectly aligned cavities. Here we will look at how these cavities behave depending on parameters such as mirror size and concentricity, and how those affect the cavity clipping losses.

Section 3.2 will take the system from section 3.1 and derive the geometry of the system under misalignment. Using this new geometry we will then analyse the performance of misaligned cavities.

Section 3.3 looks at how we can use our system to analyse other cavity regimes. In this section we look at the parameters of a neutral atom experiment and show that we

can predict the sensitivity to misalignment by comparing our model to the results of previous literature.

Section 3.4 investigates how sensitivity to misalignment might be improved by looking at a regime where the cavity mirrors have a different size and radius of curvature.

Section 3.5 will use the previous results and constraints to find the optimal cavity parameters, for ion-cavity-fibre-cavity-ion single photon transfer, and its tolerance to misalignment.

Finally section 3.6 will summarise the key results of this chapter.

3.1 Perfectly Aligned Cavities

Using Gaussian beam physics, as discussed previously in the theory section, we are able to calculate the electric field at each point on the mirror surface. This in turn can be used to calculate both a clipping loss at the mirror surface and a coupling efficiency to a fibre.

However, before considering misaligned cavities it is useful to test the model in ideal conditions. A quick test that the model behaves as expected along the cavity axis can be done by setting $y = x = 0$ in eq. (2.3).

Using eq. (2.3) we can also calculate the electric field at any point in 3d space. Calculating the surface of a curved mirror can be done using the radius of curvature, length and mirror diameter. Since we are assuming spherical mirrors, calculating the location where each point of the beam hits the mirror can be done by:

$$z^2 = R_{1,2}^2 - (x^2 + y^2), \tag{3.1}$$

where x, y, z are the spatial coordinates, $R_{1,2}$ is the radius of curvature for cavity 1 and 2, and R_{mir} is the radius of the mirror. When $R_{mir} \leq \sqrt{x^2 + y^2}$ the electric field $E_{x,y,z}$ is not calculated since the light will miss the mirror surface.

Figure 3.1 shows the electric field of the fundamental cavity mode on the surface of a fibre tip mirror with a concentricity of $\delta = 0.017$, where $\delta = \left(\frac{|R_{1,2}|}{l} - 0.5\right)$. Here we can see the Gaussian profile of the beam with a high intensity in the center falling to nearly nothing at the edge of the mirror. This plot shows that we would expect low clipping losses as most of the electric field is visibly within the mirror boundaries.

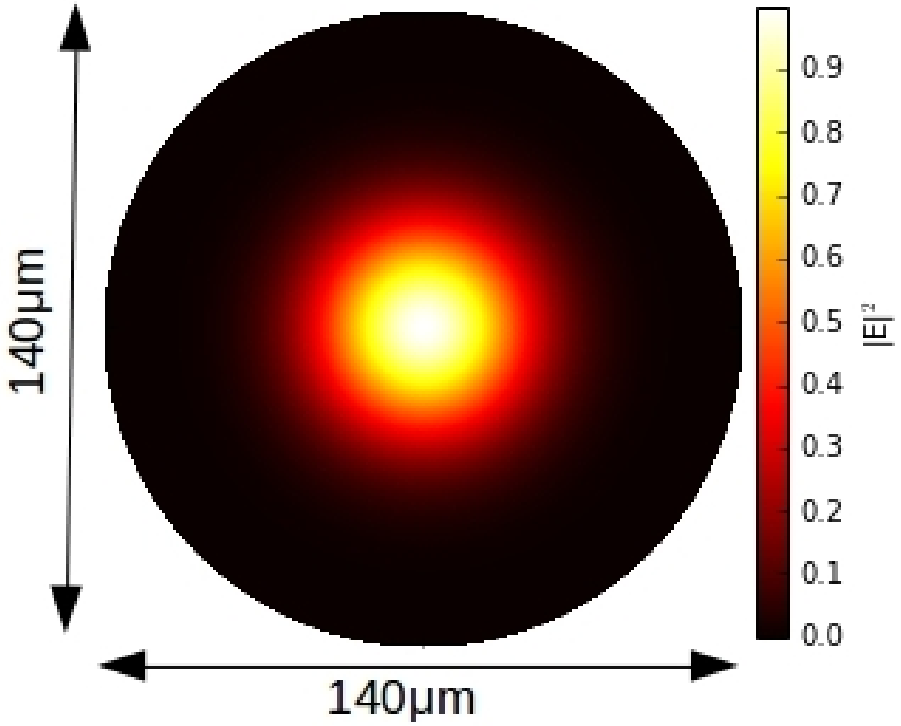

Figure 3.1: The intensity profile of $|E^2|$ on the surface of a perfectly aligned cavity mirror. Cavity parameters are given in Table 3.1.

Notice that this system is within the stability criteria of eq.(2.2). However, due to the finite size of the mirrors there will always be some clipping loss present in the system.

3.1.1 Mirror Size and Losses

Even assuming perfect mode matching, no absorption losses, no scattering losses, perfect reflectivity, and that the cavity mirrors are perfectly aligned there are still clipping losses in this system. Using stability analysis for the system in Figure 3.1 shows that the system is in the stable regime and the beam would remain unchanged. However, this is not considering clipping losses. To accurately model this system Gaussian beam physics was introduced. In most cavity experiments these clipping losses are minimal since the mirror size is much larger than the size of the TEM_{00} mode on the mirror. However, since the mirror size is constrained due to the electric field of the RF ion-trap, clipping losses play a larger role in realistic ion trap configurations. Figure 3.2, calculated using eq.(2.16), shows how much the clipping loss of a mirror varies when the mirror size, R_{mir}, and the size of the mode on the mirror, W_m, are comparable.

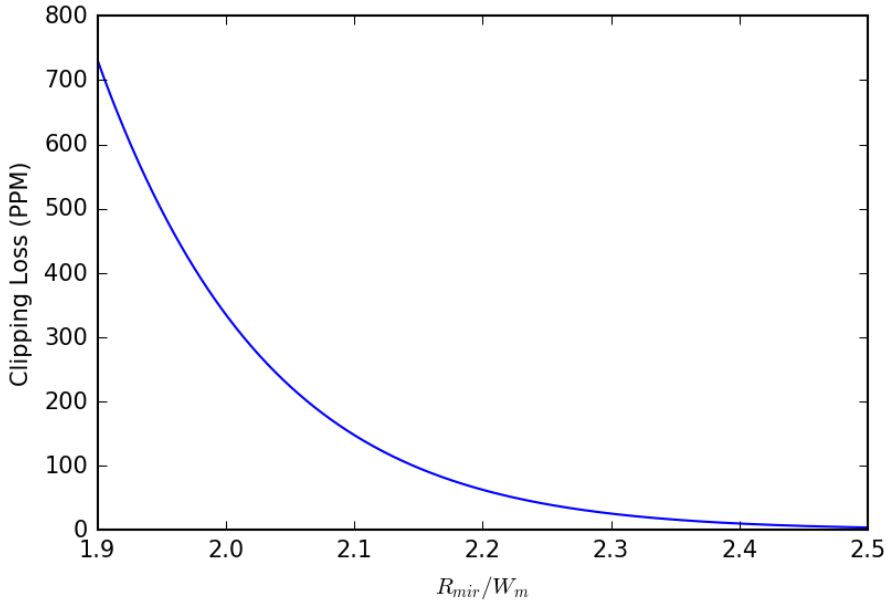

Figure 3.2: The clipping loss of a perfectly aligned mirror is dependent upon the mirror size, R_{mir}, and the size of the mode on the mirror, W_m. This graph was plotted using eq.(2.16). Section 3.2.1.2 later on includes a more complex analysis of clipping losses, including a simplified equation for the case where the mirrors are perfectly aligned.

In Figure 3.2 the cavity mirrors are perfectly aligned, yet for a single reflection off one mirror we see around 300PPM of clipping loss when the cavity mirrors are only twice as large as the beam size on the mirror, i.e. for a 70μm mirror the beam size on the mirror is 35μm. This shows that the clipping losses of a system increase exponentially as the beam size on the mirror is increased such that the size of the on-mirror spot and mirror are comparable. This ultimately puts restrictions on the minimum achievable spot size, W_0, from eq.(2.7) which reduces the achievable ion-cavity coupling strength, g, from eq.(2.24).

3.2 Misalignment

We now need to consider effects where the cavity mirrors may not be perfectly aligned. First off we consider what would happen if we misalign fibre tips without any reflection as done in past papers [83] [84]. As seen in Figure 3.3 the beam simply continues to the second fibre in a straight line, unaffected by the second fibre except for the final clipping loss.

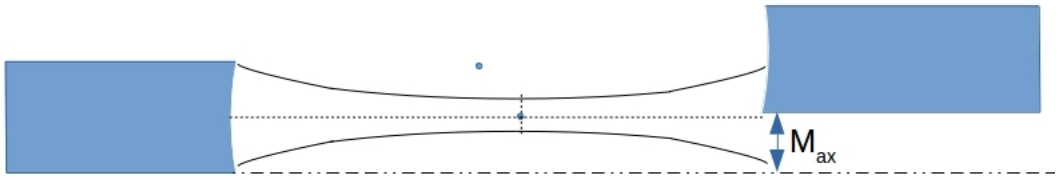

Figure 3.3: Misalignment of two distant fibres without reflective surfaces. Here we see 2 dots representing the center of curvature of each fibre, where the dot on the right is for the radius of curvature for the fibre on the left side and vice versa. The dotted line represents the centre of a Gaussian beam travelling from the fibre on the left to the fibre on the right, where the fibre on the right is misaligned by some distance M_{ax}.

Now we want to take into account the effect of multiple reflections on the fundamental cavity mode. Since cavity misalignment is a geometric issue the first step in understanding the problem was to create a geometric solution. Ray-tracing is a very simple way of quickly visualising the path light takes through a system of lenses and mirrors. Since this report focuses on the physics of two mirrors the entire ray-tracing program consists of only one fundamental equation [85]

$$\vec{v_r} = \vec{v_i} - 2(\vec{v_i} \bullet \vec{n})\vec{n}, \tag{3.2}$$

where $\vec{v_r}$, $\vec{v_i}$ and $\vec{n}$ are the reflected light vector, the incident light vector and the normal vector to the mirror plane, respectively. Figure 3.4 shows how this equation is used to calculate the reflected ray.

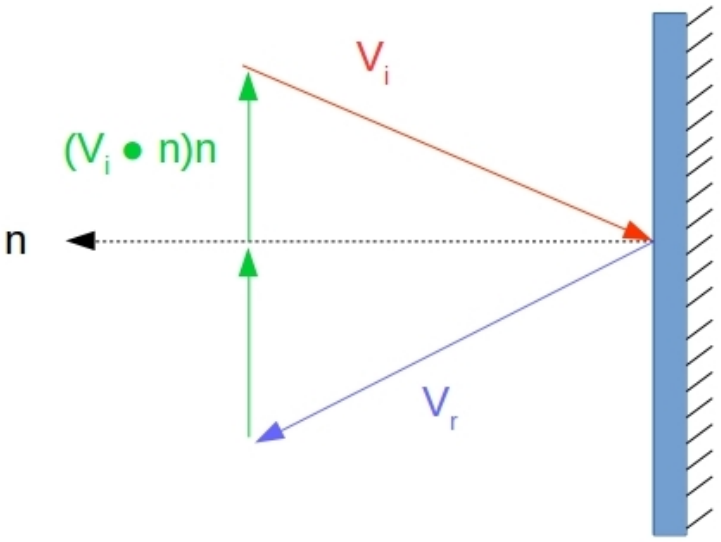

Figure 3.4: Diagram showing the reflection of a ray of light at a mirror plane using Equation (3.2). Here the black line shows the normal vector ($\vec{n}$) at the point of reflection, the red line shows the incident ray ($\vec{v_i}$), the blue line shows the reflected ray ($\vec{v_r}$), and the green line shows the vector connecting the normal at the mirror surface with the incident ray.

Note that since this simulation approximates the mirrors to be a section of a sphere the $\vec{n}$ vector can be found by normalising the vector connecting the center of the sphere and the surface point of the sphere where the incident ray of light hits.

When applying this model to a FP cavity we find that the difference between $\vec{v_i}$ and $\vec{v_r}$ causes the center of the cavity beam to rotate towards the axis connecting the two radius of curvatures. This rotation causes the misalignment seen in Figure 3.3 to be increased by some factor relating to the radius of curvatures of both cavity mirrors. This increased misalignment can be seen in Figure 3.5 for axial misalignment or Figure 3.6 for rotational misalignment. A animation of the ray tracing for the misalignment in Figure 3.5 can be found at `https://imgur.com/a/ZAYzLdk`.

As can be seen in Figure 3.5 and Figure 3.6, due to the multiple reflections within a FP cavity a small misalignment on one mirror can cause a significant tilt of the fundamental cavity mode. The magnitude of this tilt is dependent on the concentricity of the cavity, i.e. a concentric cavity will cause a significant rotation of the mode whereas a confocal cavity will scale the misalignment 1:1. By taking into account the misalignment scaling, mirror size, cavity length, wavelength, and concentricity we can define a tolerance to cavity misalignment for a desired performance. The next section will cover this effect in detail.

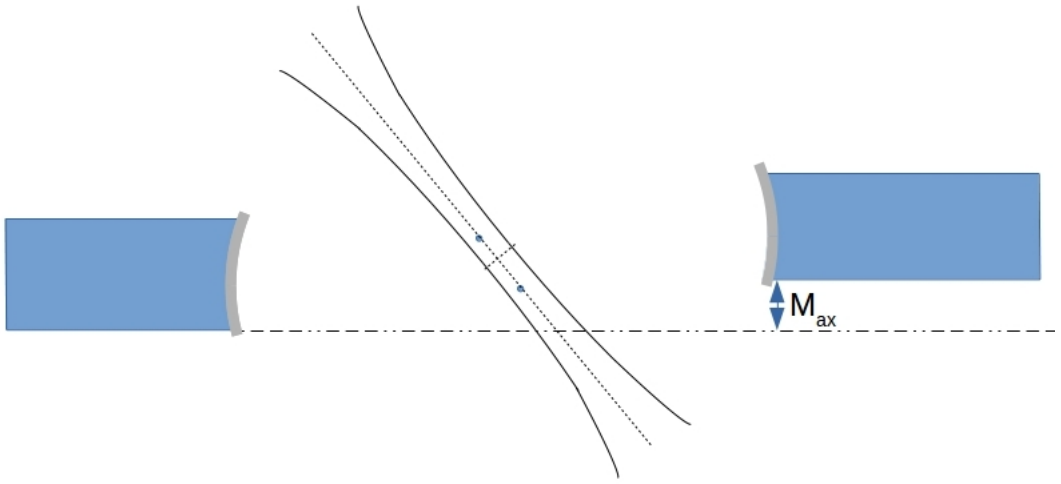

Figure 3.5: Axial misalignment of a cavity. This cavity is misaligned by the same amount as Figure 3.3. Note that the radius of curvature was chosen to exaggerate and show the effect; due to how extreme this case is all of the light would be lost before this rotation would actually be achieved.

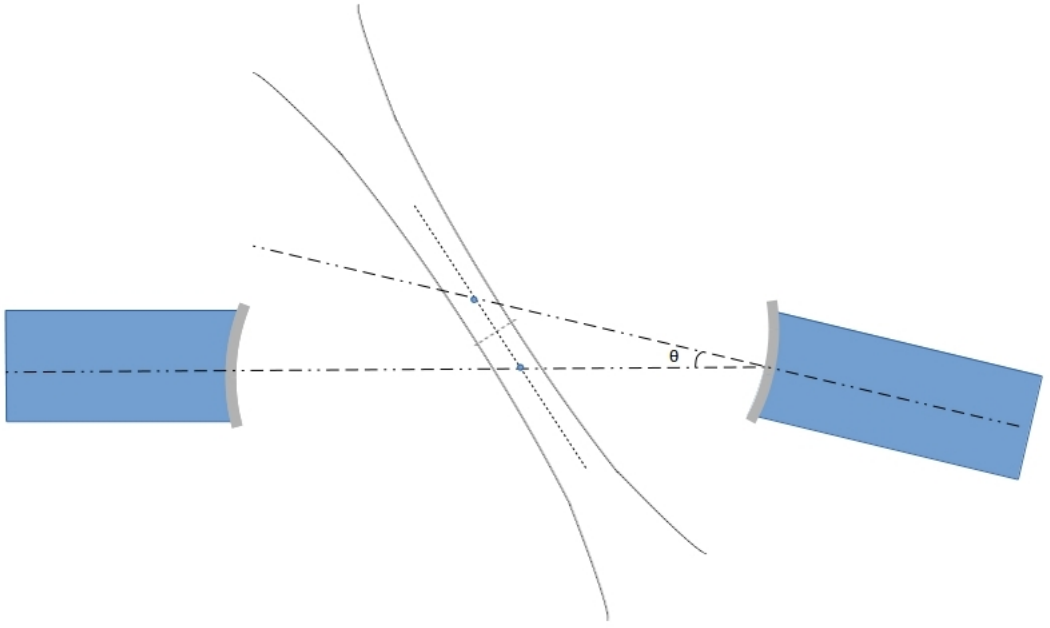

Figure 3.6: To scale rotational misalignment of a cavity, where θ shows the degree of rotation by the mirror on the right. Note that the radius of curvature was chosen to exaggerate and show the effect; due to how extreme this case is all of the light would be lost before this rotation would actually be achieved.

3.2.1 Axial Misalignment of Cavity Mirrors

Axial misalignment is defined in this thesis to mean the misalignment of the centre of curvature of the 2 cavity mirrors along a vector perpendicular to the perfectly aligned cavity axis.

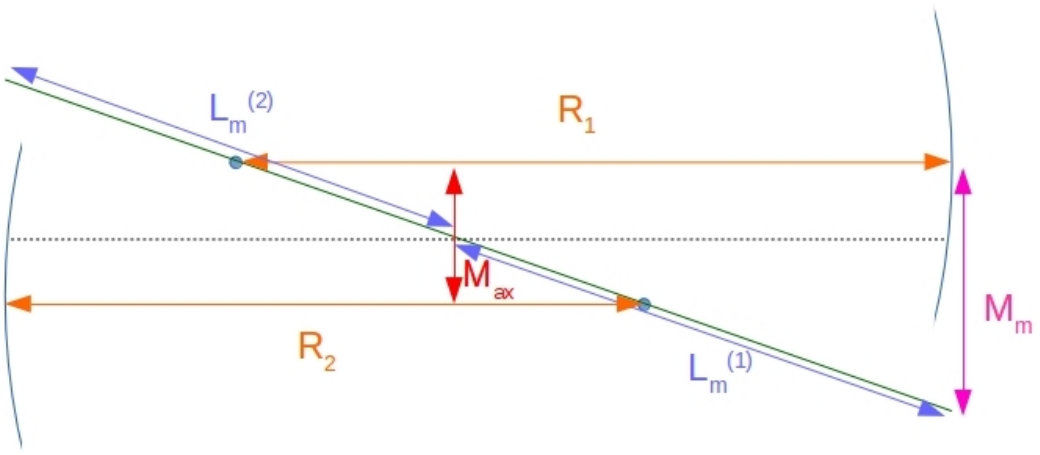

Figure 3.7: The geometry relating cavity length L, radius of curvature $R_{1,2}$, and axial misalignment M_{ax} with the on-mirror misalignment M_m. Here the green solid line represents the new cavity axis, $z = 0$.

Figure 3.7 shows how the geometry of a cavity that has been axially misaligned by M_{ax} relates to misalignment of the fundamental cavity mode on the mirror M_m. Since the fundamental cavity axis has to intersect both mirrors perpendicularly to remain stable we can find that the new cavity axis follows the line connecting the center of curvature of both mirrors. This was also confirmed using ray tracing techniques. Defining the misalignment as the displacement perpendicular to the old cavity axis we can derive the geometry. $L_m^{(1,2)}$ is the distance of mirror 1 and 2, respectively, from the centre of the cavity along the cavity axis. This value can be calculated with the cavity length L and radius of curvature $R_{1,2}$ of mirrors 1 and 2, respectively, by

$$L_m^{(1)} = \frac{|R_1| - |R_2|}{2} - \frac{L}{2}, \tag{3.3}$$

$$L_m^{(2)} = L_m^{(1)} + L. \tag{3.4}$$

Using $L_m^{(1,2)}$ and the axial misalignment M_{ax}, from Figure 3.7, we can calculate the on mirror misalignment $M_m^{(1,2)}$ of the cavity axis at each mirror with

$$M_m^{(1,2)} = \left| L_m^{(1,2)} \frac{M_{ax}}{|R_1| + |R_2| - L} \right| + \left| \frac{M_{ax}}{2} \right|. \tag{3.5}$$

In the case of identical cavity mirrors, $R = R_2 = -R_1$, and introducing the term

$$\delta = \frac{R}{L} - 0.5 \tag{3.6}$$

we can reduce eq. (3.5) to

$$M_m = M_{ax}\left(\frac{1}{4\delta} + \frac{1}{2}\right). \tag{3.7}$$

Note that we can also substitute eq.(3.6) into eq.(2.5) to obtain a beam waist, W_o, dependent version of the concentricity, δ

$$\delta = \frac{2\pi^2 W_o^4}{\lambda^2 L^2}. \tag{3.8}$$

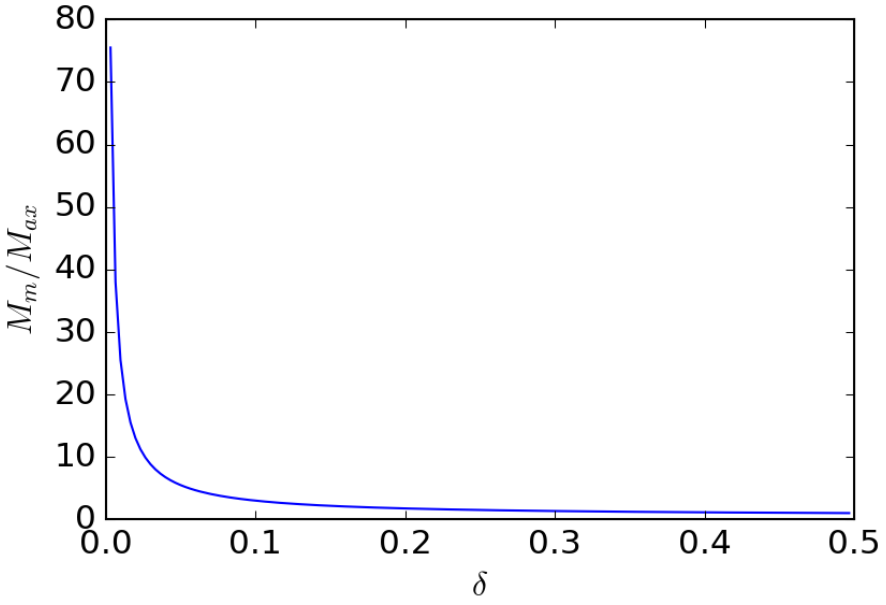

Figure 3.8: The scaling from axial misalignment, M_{ax}, to on-mirror misalignment, M_m, scales inversely proportional to the concentricity, $1/\delta$, as seen in eq. (3.7)

Figure 3.8 shows how the concentricity parameter, δ, of a symmetric FP cavity affects the alignment scaling of the system, where alignment scaling is defined by M_m/M_{ax}. Note that for a confocal system, $\delta = 0.5$, we obtain a 1:1 scaling ratio where $M_{ax} = M_m$. However, as the alignment scales $\propto 1/\delta$ we see a large misalignment as the concentricity parameter decreases.

Using the misalignment geometry, as previously derived, we can simulate the electric field similar to Figure 3.1 with an axial misalignment, M_{ax}, of 5μm. The resulting on-mirror misalignment for this mirror M_m is 76μm, as seen in Figure 3.9. This cavity shows that there is a need to further analyse the clipping losses, even for systems which look stable such as Figure 3.1, as the on-mirror spot has been misaligned to the point were we would expect most of the light in the cavity to be lost due to it missing the cavity mirror.

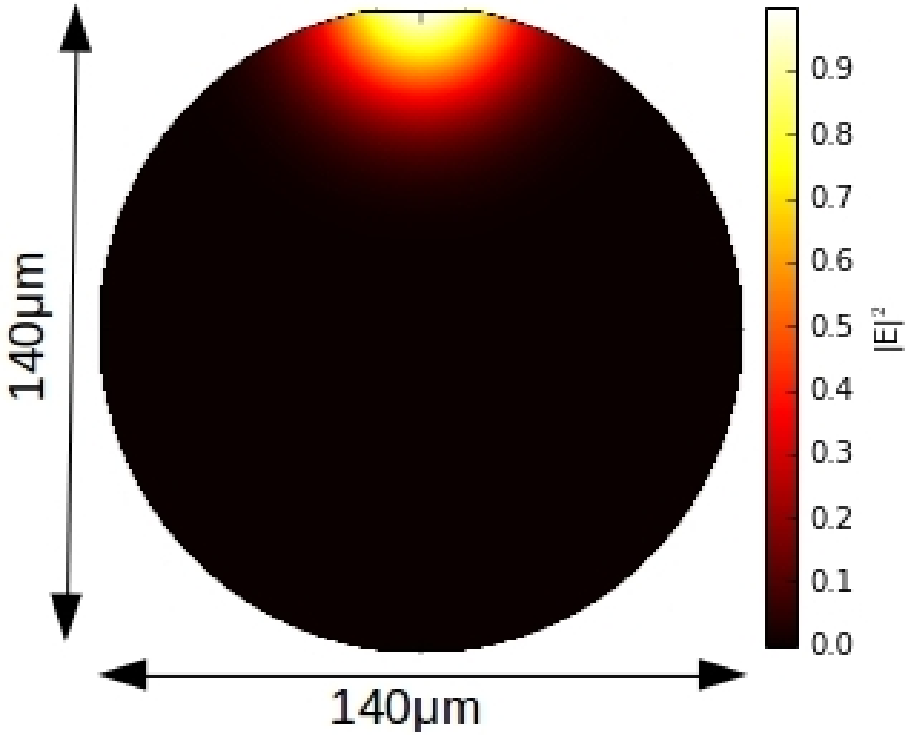

Figure 3.9: This figure shows a visualisation of the same cavity set up as in Figure 3.1. However, in this figure the mirrors are 5μm misaligned. This axial misalignment M_{ax} corresponds to a on-mirror misalignment M_m of 76μm for this particular cavity.

3.2.1.1 Mode Matching

For this thesis we also consider the coupling between the fibre and the optical cavity. To increase the coupling efficiency of a FP resonator to an optical fibre it is necessary to use mode matching optics. A graded index (GRIN) lens [60] has shown potential to achieving optimal overlap efficiency between a cavity fundamental TEM_{00} mode and the fibre (as discussed in Section 2.1.6). Here it is assumed that the mode matching optics are set up such that 100% coupling efficiency is achieved when perfectly aligned (i.e. electric field distribution on the mirror surface is the same as the end of the fibre mode). The coupling efficiency of the cavity mode with the fibre mode can be expressed by the overlap integral [36]

$$\eta = \frac{|\int\int E_p E_m^* dxdy|^2}{\int\int |E_p|^2 dxdy \int\int |E_m|^2 dxdy}, \tag{3.9}$$

where the integrals are over the mirror surface, E_p and E_m are the electric field at the mirror of the perfectly aligned beam and the misaligned beam respectively.

Using the analytical expression for the overlap of two misaligned Gaussian beams, for free space optics, found in literature [83],

$$\eta = e^{-\left(\frac{M_m}{W_m}\right)^2}, \tag{3.10}$$

we were able to verify the results of our numerical evaluation of eq. (3.9). This was done by comparing the analytical formula to the results of using a confocal cavity in our simulation to avoid effects of misalignment scaling. Also, by combining eq. (2.8) with eq. (3.7) and substituting eq. (3.10) we were able to derive the analytical expression

$$M_{tol} = \sqrt{\frac{2\ln(\sqrt{\eta})\lambda L(2\delta)^{3/2}}{\pi(1+2\delta)}}, \tag{3.11}$$

where M_{tol} defines the axial misalignment, M_{ax}, before relative coupling efficiency falls to η for a mode matched device. Note that this means that assuming δ is kept constant the tolerance to misalignment actually increases with cavity length, L. This is because the spot size on the mirror, W_m, also increases with L, as seen in eq. (2.8).

We know from eq.(3.7) that the on-mirror misalignment, M_m, scales with the inverse concentricity, $1/\delta$, and that from eq.(3.8) the concentricity is proportional to the beam waist W_0^4. Therefore, using the FP cavity shown in Figure 2.4 as an example we can fix the length at L = 1.4mm, and the wavelength at $\lambda = 866$nm and show how M_{tol} is affected by W_0 in Figure 3.10.

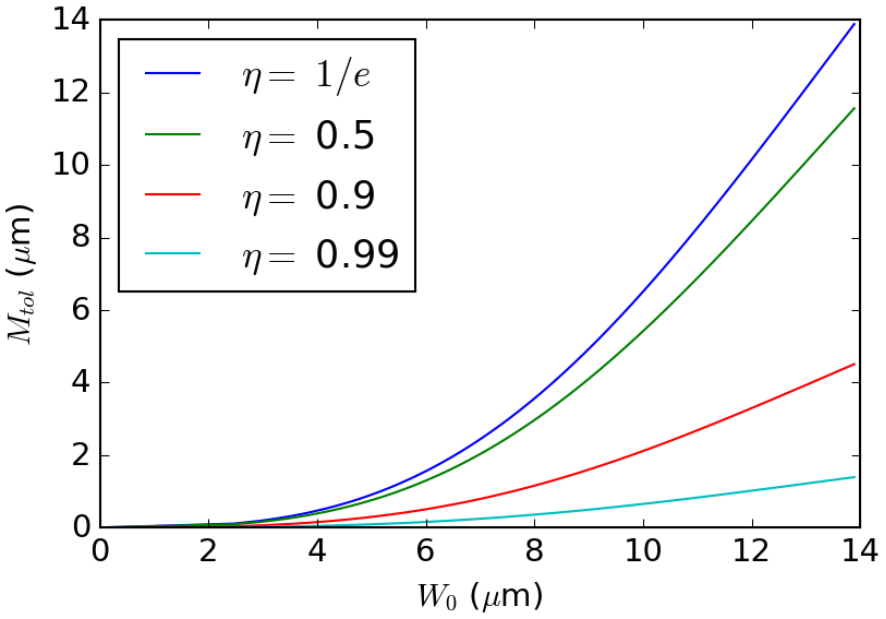

Figure 3.10: Axial alignment tolerance, M_{tol}, versus the coupling efficiency, η, when the concentricity of the cavity, δ, is varied to give different spot sizes, W_0. Here the cavity length is 1.4mm and the wavelength is $\lambda = 866$nm.

Figure 3.10 shows that the tolerance to misalignment, M_{tol}, increases with spot size, W_0, and decreases with larger desired coupling efficiencies η. This shows that the alignment accuracy is one limit on the minimum spot size achievable by our cavity whilst maintaining strong coupling to the fibre. By extension, since a small spot size, W_0, is required to obtain a large ion-cavity coupling strength, g, from eq. (2.24) we can expect that the alignment tolerance, M_{tol}, is an important limit on the overall performance of the device.

3.2.1.2 Clipping Losses

Other than the coupling efficiency, we also need to consider other cavity losses to properly analyse the behaviour of the system. Since the diameters of mirrors used in Figure 2.4 are $\sim 100\mu$m with cavity lengths that are $\sim$mm it is worth investigating how much of the cavity mode is lost because it misses the mirrors. This loss, known as clipping loss, was introduced at the end of Section 2.1.3.

Since the requirement of a large coupling strength from eq. (2.24) requires a small spot size, W_0, and the presence of an ion trap requires a large cavity length, L [36], we can see that we will expect the system to have a large on-mirror spot size, W_m, from eq. (2.8) and a small concentricity, δ, from eq. (3.6). This means that the system will have a large misalignment scaling, M_m/M_{ax}, and since W_m is in the same order of magnitude as the radius of the mirror, R_{mir}, we can expect a high clipping loss, ρ, even when the cavity is perfectly aligned.

By looking at the ratio of on-mirror misalignment, M_m, with the radius of the mirror, R_{mir}, we can see in Figure 3.11 how the clipping loss in parts per million (PPM) of any arbitrary cavity changes with misalignment. This was calculated by numerically evaluating eq. (2.16) with different cavity parameters and misalignments. By using eq. (3.7) and substituting a known alignment precision as M_{ax} it is possible to calculate the expected clipping loss from Figure 3.11, or vice versa, it is possible to calculate the precision needed for a cavity with an arbitrary clipping loss to drop to an undesired level for any cavity regime. This graph can also be used to show how small the on-mirror spot size W_m (or how large the cavity mirrors R_{mir}) would need to be to compensate for low misalignment tolerance.

Defining the tolerance in a similar way to [83] we can obtain an expression for clipping loss of perfectly aligned mirrors,

$$\rho = e^{-2\left(\frac{R_{mir}}{W_m}\right)^2}. \tag{3.12}$$

We can now easily calculate the required mirror size for any required clipping loss, ρ, when perfectly aligned with

$$R_{mir} = \sqrt{\frac{-\ln(\rho)}{2}} W_m. \tag{3.13}$$

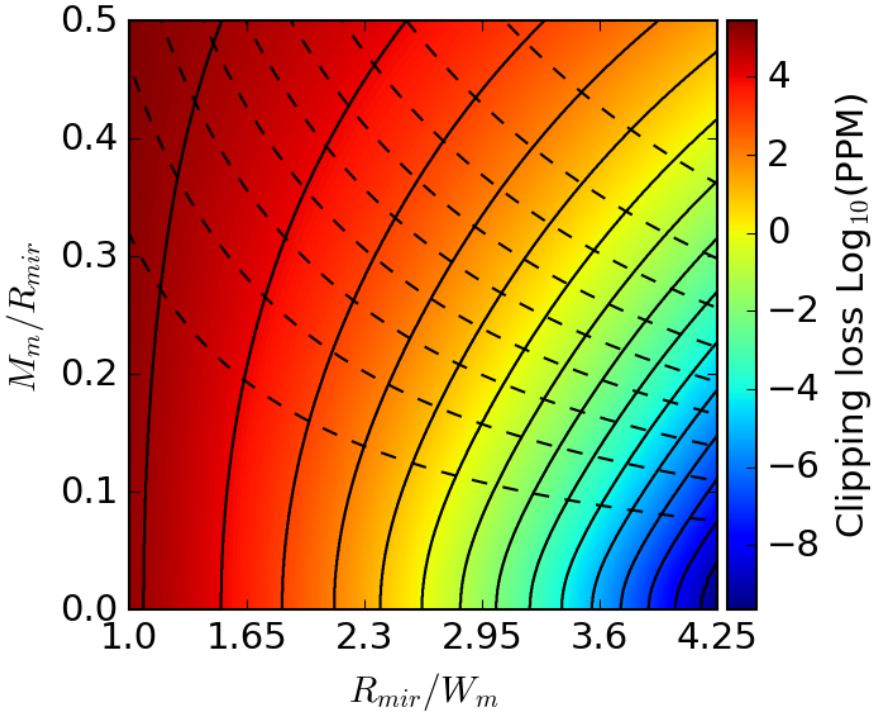

Figure 3.11: The ratio of on-mirror misalignment, M_m, with the mirror size, R_{mir}, affects the clipping loss of a mirror associated with the ratio of the mirror size, R_{mir}, to the spot size at the mirror, W_m. To easily read the data the solid black lines indicate contours at integer PPM loss values, $\log_{10}$(PPM), from 5 to -9. The dashed black lines show the coupling efficiency η from 0.9 to 0.1 in intervals of 0.1. The coupling efficiency lines were calculated using eq. (3.10) and fixing η at the desired value. Note that this graph was calculated per cavity mirror, not for the overall cavity losses.

Using Figure 3.11 we are able to analyse the coupling efficiency and clipping loss of the system shown in Figure 2.4. Using a concentricity of $\delta = 0.0166$, chosen to obtain a beam waist of $< 6\mu$m, we can work out the beam size at the cavity mirror, $W_m = 32.9\mu$m, and therefore a mirror/beam ratio of $R_{mir}/W_m = 2.13$, or 114PPM loss from eq. (3.12). From Figure 3.11 we can see that this clipping loss increases by a factor of 10, and the coupling efficiency, η, falls to 80% at a misalignment of $M_m/R_{mir} = 0.22$. Using eq. (3.7) we can see that this corresponds to an axial misalignment, M_{ax}, of 0.99μm. Since this clipping loss is for a single mirror we can calculate the overall clipping loss by,

$$\rho_{roundtrip} = \rho_{m1} + \rho_{m2}(1 - \rho_{m1}), \tag{3.14}$$

where $m1$ and $m2$ refer to mirror 1 and 2 respectively. For small clipping losses we can approximate the round trip loss, $\rho_{roundtrip}$, by adding both clipping losses. This means that our clipping loss has increased from $\sim$ 200PPM to $\sim$ 2000PPM for 0.99μm axial misalignment.

We are also able to use eq. (2.16) to calculate the misalignment tolerances of the cavity shown in Figure 2.4 with respect to the beam waist, W_0. Figure 3.12 shows the axial misalignment tolerance for clipping losses of 10, 100, 1000, and 10000 PPM and its dependence on beam waist. It is worth noting that due to clipping losses when perfectly aligned, as seen in in eq. (3.12), Figure 3.12 does not start at 0PPM.

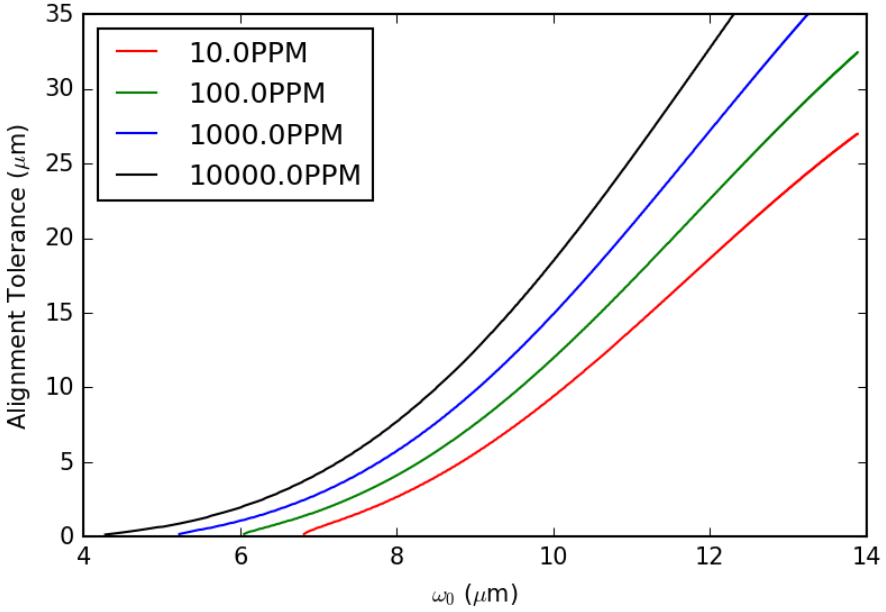

Figure 3.12: Axial misalignment tolerance with respect to cavity spot size for a cavity length $L = 1.4$mm, mirror size $R_{mir} = 70\mu$m, and wavelength $\lambda = 866$nm.

3.2.2 Rotational Misalignment of Cavity Mirrors

Figure 3.6 shows a diagram of the expected tilt of the cavity mode when one mirror is rotationally misaligned. For this type of misalignment a resulting geometry shown in Figure 3.13 was considered. Here, one mirror was rotated around the point where the perfectly aligned cavity axis intersects with the surface of the mirror by some angle θ. In the case the magnitude of misalignment is different for each of the cavity mirrors. This asymmetry means that additional care is needed to calculate the misalignment of the mode on the tilted mirror as seen in Figure 3.14.

For rotational misalignment we found that, as is the case with the axial misaligned cavity, the new cavity axis is rotated so that it passes through the centres of curvature of both mirrors. We can use this geometry, as shown in Figure 3.13, to derive an equation describing the misalignment on mirror 1, M_{m1}

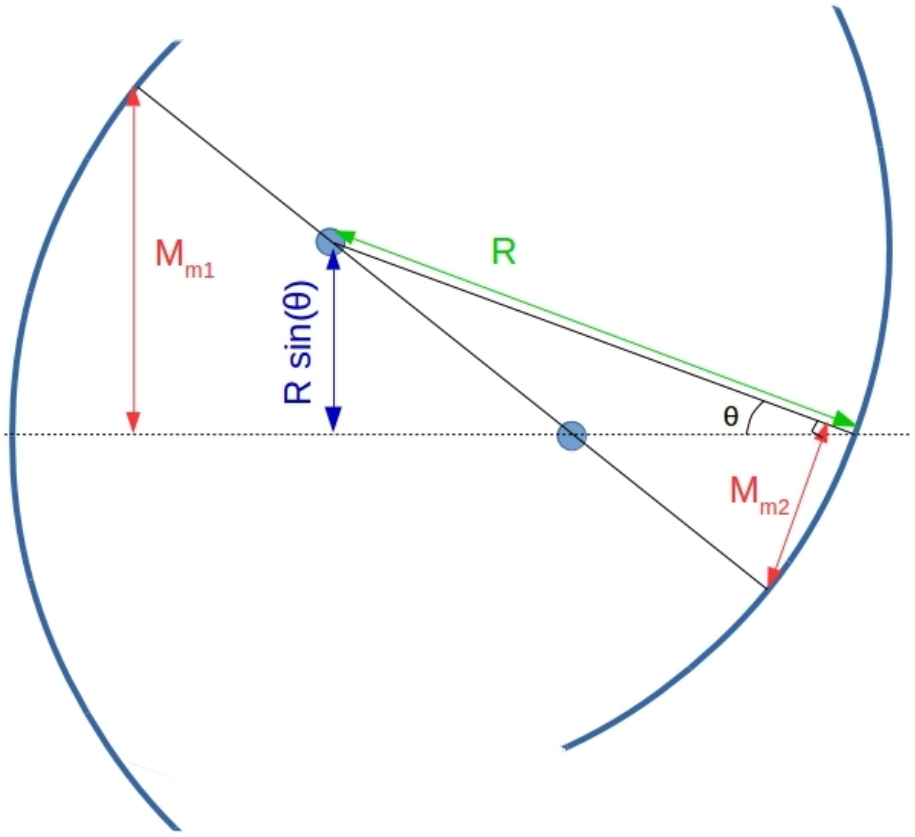

Figure 3.13: Tilting mirror 2 by some angle θ around the center of the mirror affects the alignment of the self consistent cavity mode on mirrors 1 and 2. Here the red lines indicate the on mirror misalignment, M_m, and the green line shows the radius of curvature R.

$$M_{m1} = R\sin(\theta)\left[\frac{1}{4\delta} + 0.5\right], \tag{3.15}$$

however the misalignment on mirror 2, M_{m2}, is more complex. The equation for M_{m2} can be derived using the geometry of the zoomed in diagram in Figure 3.14,

$$M_{m2} = \frac{A}{\cos(\theta)} + M_D\tan(\theta), \tag{3.16}$$

where M_D is the depth of the mirror at the point where the center of the cavity mode intersects the mirror surface. The distance A represents the perpendicular misalignment from the perfectly aligned cavity axis and can therefore be obtained via

$$A = R\sin(\theta)/left[\frac{1}{4\delta} - 0.5/right], \tag{3.17}$$

where the -0.5 indicates a mode shift towards the mirror center rather than away as seen in eq. (3.15). To calculate M_{m2} from A we then need to rotate the vector by the

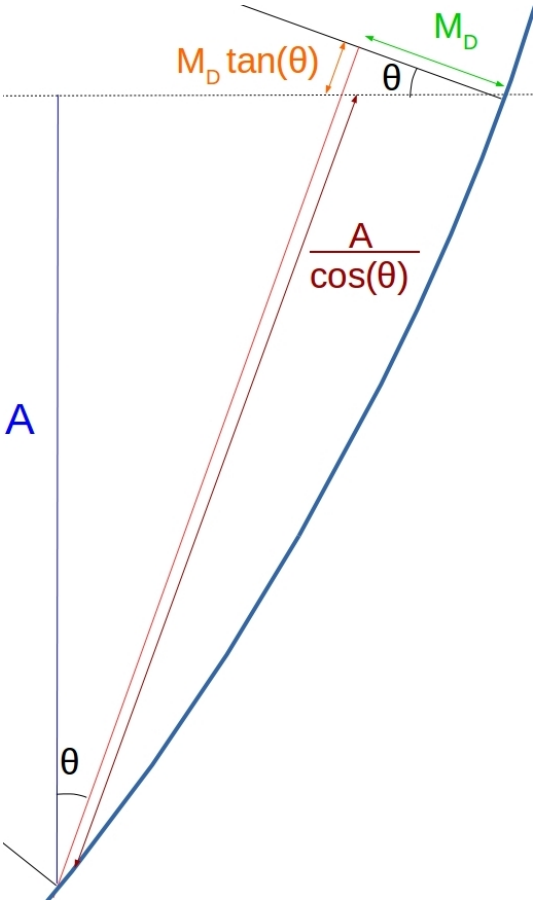

Figure 3.14: Zooming in on Figure 3.13 to show misalignment on the tilted mirror. M_D is the mirror depth from the point where the centre of the fundamental cavity mode, after tilting, intersects the mirrors surface. A is the on mirror misalignment of the mode perpendicular to the perfectly aligned cavity axis.

tilt of the mirror, and then calculate the additional misalignment from the mirror center caused by the curvature of the mirror at the point where the center of the cavity mode intersects the mirror surface,

$$M_D = |R| - \sqrt{R^2 - M_{m2}^2}. \tag{3.18}$$

M_D can be calculated by substituting eq. (3.16) into eq. (3.18) and solving the resulting quadratic equation. This gives the equation

$$M_D = \frac{-C_b - \sqrt{C_b^2 - 4C_aC_c}}{2C_a}, \tag{3.19}$$

where C_a, C_b, and C_b are

$$C_a = 1 + \tan^2(\theta), \tag{3.20}$$

$$C_b = \frac{2A\tan(\theta)}{\cos(\theta)} - 2R, \tag{3.21}$$

$$C_c = \left(\frac{A}{\cos(\theta)}\right)^2, \tag{3.22}$$

respectively. Substituting eq. (3.19) into eq. (3.16) we can finally calculate the displacement of the cavity mode on a tilted mirror M_{m2} in eq. (3.23) as shown in Figure 3.14.

$$\frac{M_{m2}}{\tan(\theta)} = R\left(\frac{1}{4\delta} - 0.5\right) + \frac{2R\left[1 - \left(\frac{1}{4\delta} - 0.5\right)\tan^2(\theta)\right]}{2 + 2\tan^2(\theta)} - \frac{\sqrt{\left\{2R\left[\left(\frac{1}{4\delta} - 0.5\right)\tan^2(\theta) - 1\right]\right\}^2 - 4\left[1 + \tan^2(\theta)\right]\left[R\tan(\theta)\left(\frac{1}{4\delta} - 0.5\right)\right]^2}}{2 + 2\tan^2(\theta)} \tag{3.23}$$

3.2.2.1 Mode Matching

To calculate the fibre-cavity coupling efficiency when a mirror is tilted we use the previously derived geometry. We also find an expression describing the approximate tolerance to the mirror tilt. First of all we can simplify the expressions by assuming M_D and θ will be sufficiently small such that the small angle approximation holds and M_D does not add significant misalignment. These assumptions can be further justified since mirror 1 sees the larger misalignment and thus the performance of the system is less affected by the misalignment on the tilted mirror diminishing the effects of M_D even more. We can now write the simplified equations as

$$M_{m1} \approx R\theta\left(\frac{1}{4\delta} + 0.5\right), \tag{3.24}$$

and

$$M_{m2} \approx R\theta\left(\frac{1}{4\delta} - 0.5\right). \tag{3.25}$$

Substituting these into eq. (3.10) we obtain

$$\theta_{tol} \approx \sqrt{\frac{\ln(\eta)\lambda\sqrt{\frac{2}{\delta}}}{2\pi L(\delta+0.5)\left(0.5+\frac{2}{(4\delta)^2}\right)}}. \tag{3.26}$$

Note that unlike M_{tol}, in eq. (3.11), when δ is kept constant the angular misalignment tolerance, θ_{tol}, decreases with the cavity length, L.

Focusing on the structure shown in Figure 2.4 we can now compare our approximation in eq. (3.26) to the full numerical simulation using eq. (3.23). Figure 3.15 shows how the approximate misalignments from eq. (3.24) and eq. (3.25) compare to the full derivations in eq. (3.15) and eq. (3.23) when calculating the coupling efficiency.

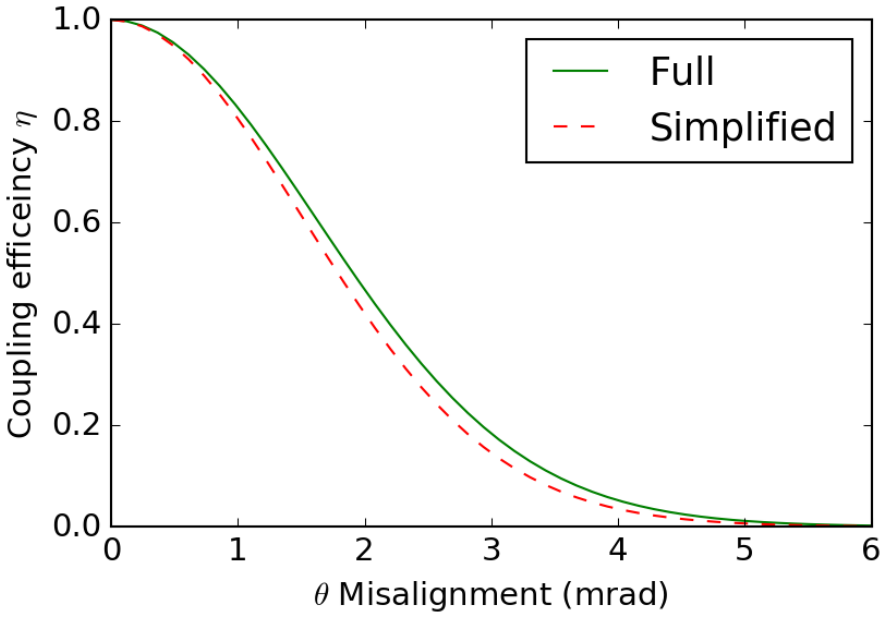

Figure 3.15: Coupling efficiency η vs angle of misalignment θ. Here the cavity length was fixed at 1.4mm and the wavelength at 866nm to match the system shown in Figure 2.4. The solid green line is the numerical simulation of the exact geometry from eq. (3.23) and the dashed red line is the approximation using eq.(3.26).

Since Figure 3.15 shows a good agreement between the simplified and full calculation we can use the approximate solution in eq. (3.26) to calculate a tolerance to rotational misalignment, θ_{tol}, for various fibre-cavity coupling efficiencies, η, as shown in Figure 3.16.

Using Figure 3.16 we can see that at smaller spot sizes, W_0, and larger required coupling efficiencies, η, the tolerance to angular misalignment, θ_{tol}, goes down from $\theta_{tol} \approx 10$mrad to $\theta_{tol} < 1$mrad.

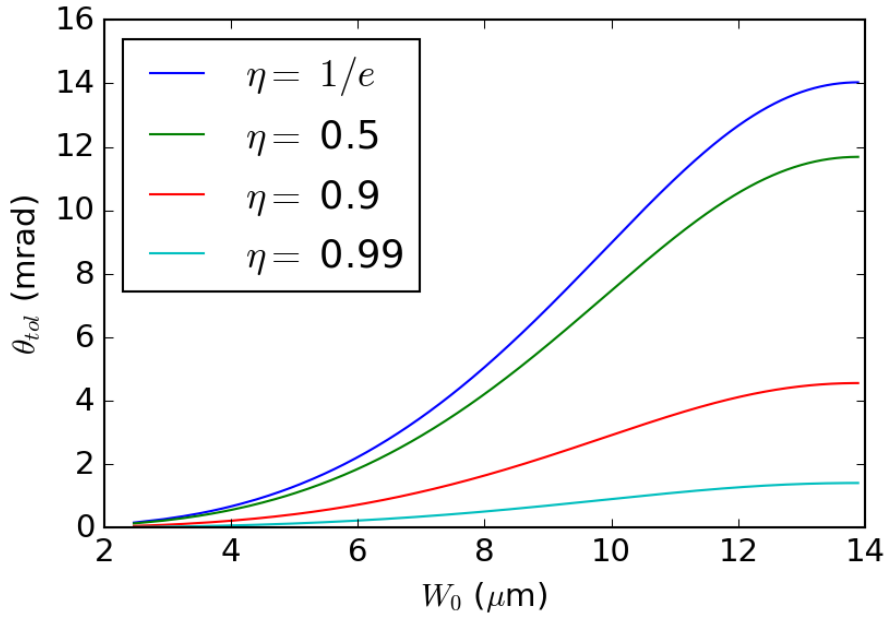

Figure 3.16: Tilt alignment tolerance, θ_{tol}, versus the coupling efficiency, η, when the concentricity of the cavity, δ, is varied to give different spot sizes, W_0. Here the cavity length is 1.4mm and the wavelength is $\lambda = 866$nm.

3.2.2.2 Clipping Losses

We are able to use Figure 3.11 to analyse the clipping losses of rotational misalignment as well. This is because the results in Figure 3.11 are calculated for each mirror and not the cavity as a whole. This is important because unlike axial misalignment, rotational misalignment does not displace the cavity mode by the same amount on both mirrors as shown in Figure 3.13 as well as eq.(3.23) and eq.(3.15).

3.3 Neutral Atom Experiments

Eq. (3.13) tells us that the clipping loss, when the cavity is perfectly aligned, is limited by the beam size at the mirror and thus the concentricity of the cavity as well as mirror size. This means that a larger mirror allows us to achieve a smaller spot size, W_0, and concentricity, δ, without increasing clipping loss, ρ.

Neutral atom experiments usually operate in a more concentric regime, to achieve strong atom-cavity coupling, and Figure 3.8 shows us that as $\delta \to 0$ the misalignment scaling of the cavity increases significantly, $M_m/M_{ax} \to \infty$. This shows that although larger mirrors can allow for larger on-mirror spot sizes and thus smaller beam waists, the spot displacement on the mirror is more sensitive to axial misalignment. This seems to indicate that neutral atom cavities are significantly more sensitive to misalignment. However, the significantly larger spot size and mirror diameter cause a larger tolerance to on-mirror displacement.

Applying the theory above to a specific example of the highly concentric neutral atom cavity demonstrated in reference [44] with cavity length $L \approx 11$mm, radius of curvature, $R = 5.500(6)$mm, and probe wavelength $\lambda = 780$nm, we are able to predict the results of misalignment in their experiment. For the clipping loss calculations it is also assumed that the mirrors used were the same as the ones used in earlier work by the same group [50] with a mirror diameter of $2R_{mir} = 8.39$mm. This paper was chosen since the experiments show an alignment tolerance, M_{tol}, of 59.(3)nm for a coupling efficiency, η of 50%. This misalignment with these cavity parameters yields an on-mirror misalignment, M_m, of 198μm. Figure 3.17 shows the results of the coupling efficiency simulation for this cavity where the dashed black lines meet at the alignment tolerance shown in literature of $M_{tol}(\eta = 0.5)$. This result helps to check the validity of our simulations and shows that whilst neutral atom experiments may achieve much stronger atom-cavity coupling strengths their cavity-fibre coupling efficiencies are a lot more sensitive to misalignment than fibre tip cavities.

Due to the large mirrors, and by extension tiny clipping losses, a full simulation of the clipping losses in this regime was not possible. Using eq. (3.12) we can see that the perfectly aligned clipping losses would be $\rho = 7.5 \times 10^{-138}$. Since we are dealing with clipping losses that are extremely small we cannot simulate the full clipping loss due to misalignment. However, we can use the mirror spot size, W_m, of 331μm and the mirror size, R_{mir}, of 4195μm to calculate the axial misalignment, M_{ax}, before the edge of the spot on the mirror is at the mirrors edge, i.e. $M_m = R_{mir} - W_m$. This happens when $M_{ax} = 1.2\mu$m which is a factor of 20 more than the alignment tolerance before the coupling efficiency falls to 0.5. This shows that since neutral atom experiments can have significantly larger mirrors and by extension be more concentric, than fibre-tip mirrors in an ion trap, they suffer more from coupling efficiency drops when misaligned than clipping losses.

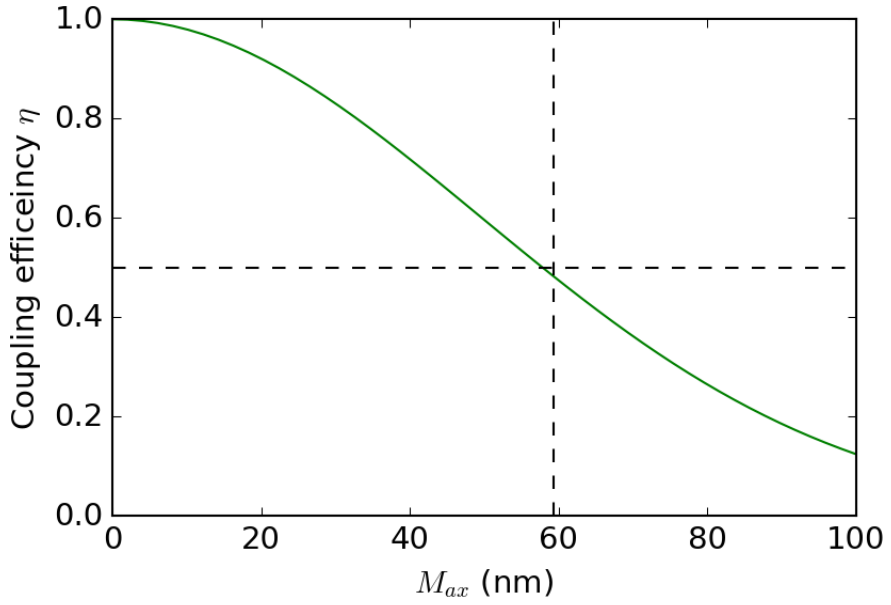

Figure 3.17: Coupling efficiency, η, versus axial misalignment, M_{ax}, of the cavity in reference [44]. Here the dashed lines show a coupling efficiency of $\eta = 0.5$ and a misalignment of $M_{ax} = 59.3$nm, as measured in reference [44], and the green solid line shows the results of our simulation.

3.4 Asymmetric Mirror Regimes

A potential solution to the problem of alignment tolerance is to use an asymmetric mirror regime as seen in Figure 3.18. For analysis in this regime we have two systems, one where we maintain the overall cavity length L of 1.4mm, and another where we maintain the distance from the ion to the fibre of 0.7mm so that it may be integrated into an ion-trap based quantum computer. This model assumed that only one end of the cavity needs to be a fibre mirror, and the large mirror can be considered highly reflective.

To compare the performance of this geometry to our fibre tip cavity when interacting with an ion we first calculate the cavity finesse using

$$F \approx \frac{2\pi}{\epsilon_{tot}}, \tag{3.27}$$

where ϵ_{tot} is the overall round trip loss. Using eq. (3.27) we are able to calculate the cavity decay rate,

$$\kappa = \frac{c\pi}{2FL}, \tag{3.28}$$

where c is the speed of light. Using eq. (2.24) we can calculate the cavity-ion coupling strength, g. Using $^{40}Ca^{+}$ ions [45], with an atomic decay rate of $\gamma = 11.2(2\pi)$MHz, we are now able to obtain the cooperativity, which is a measure of the ion-cavity coupling strength compared to the losses of the system, of the system defined by

$$C = \frac{g^2}{2\kappa\gamma}. \tag{3.29}$$

Using eq. (3.27) and eq. (3.28) we can relate the decay rate of the cavity directly to the round trip losses,

$$\kappa = \frac{c\epsilon_{tot}}{4L}. \tag{3.30}$$

Figure 3.19 shows the decay rate of the cavity shown in Figure 3.18 along with black areas which yield a beam waist W_0 of less than 6μm. This figure was created with an arbitrary axial misalignment M_{ax} of 8.64μm and areas with a decay rate κ over 10MHz are shown as white space. This allows a comparison of different cavity regimes to be quickly made to identify those with a large coupling strength g and high misalignment tolerance.

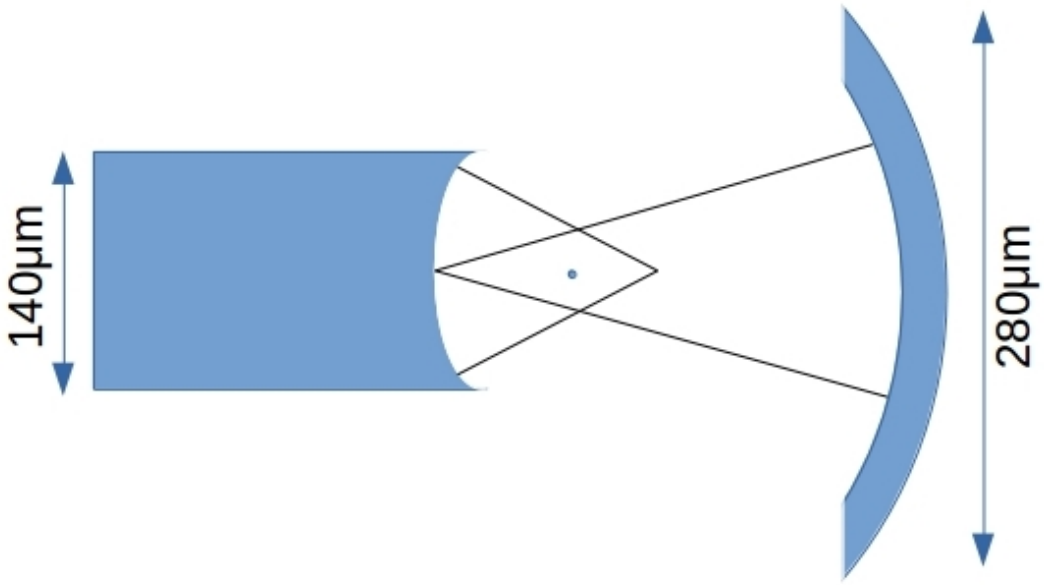

Figure 3.18: An asymmetric cavity regime with an increased tolerance to misalignment.

Using Figure 3.19 a cavity regime of $R_1/L \approx 0.5$ for the fibre mirror and $R_2/L \approx 1$ for the large mirror was selected.

Two different models of Figure 3.18 were created, the first has a cavity length L of 1.4mm (Asym 1) to keep the overall cavity distance as fixed, the second had a cavity length L of 1.63mm (Asym 2) to keep the beam waist W_0 at a set distance of $1.4/2 = 0.7$mm from the fibre tip. This was done to satisfy the distance requirement for integration into an ion-trap. A symmetrical cavity where both mirrors are fibre tips and have a cavity length $L = 1.4$mm (Sym) was also simulated for comparison with this asymmetric regime. For this comparison the concentricity δ of all three simulations was adjusted to achieve an initial decay rate κ of 10MHz due to clipping loss when perfectly aligned. Table 3.2 shows the parameters of the three cavities when perfectly aligned.

Varying the alignment of all three cavities in Figure 3.20, we can see that Sym starts out with a slightly larger cooperativity than Asym 2 and a significantly lower cooperativity than Asym 1. As we vary the misalignment of all three cavities we see that the cooperativity of the fibre tip cavity decays to < 1 within 1.67μm, whereas both Asym 1 and 2 reach a cooperativity of < 1 at around 30μm. This indicates that the asymmetric regime in Figure 3.18 is over 10 times more tolerant to misalignment than the symmetric fibre regime in Figure 2.4.

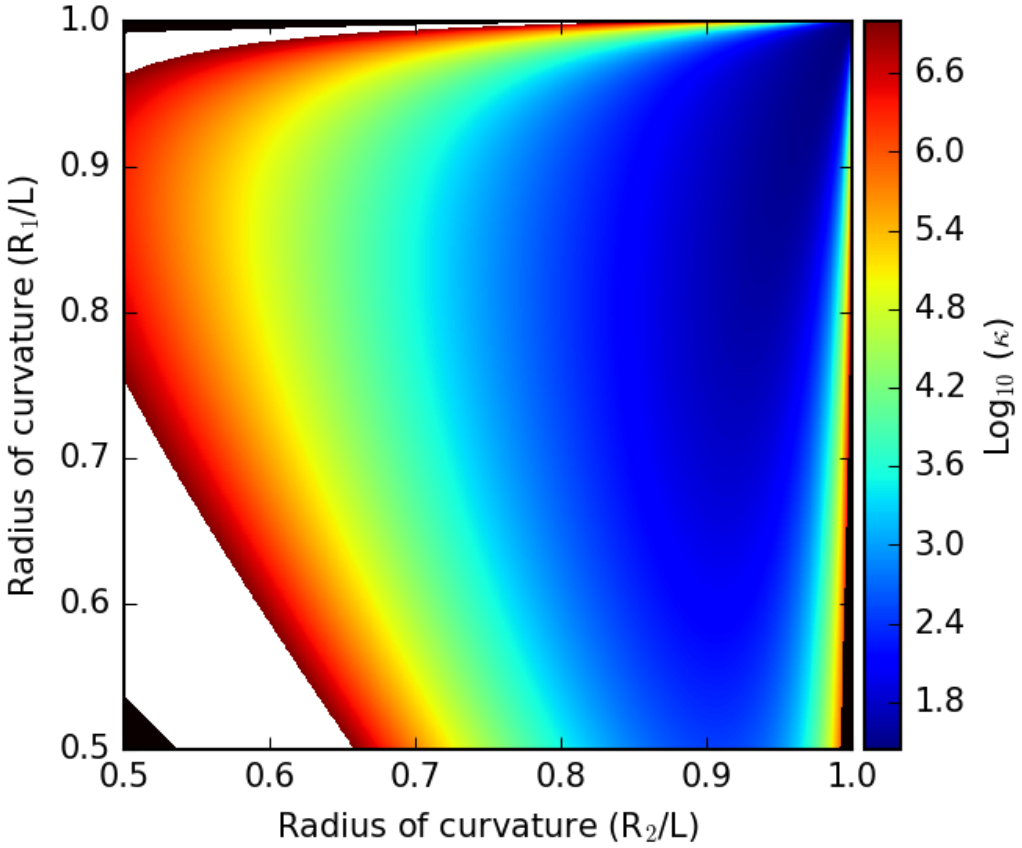

Figure 3.19: Cavity decay rate κ versus design parameters of the asymmetric cavity of Figure 3.18. Analysis was done by plotting the areas where the beam waist is $< 6\mu$m in black and overlaying it on the cavity decay rate κ. We can see that the area of a $R_1/L \approx 0.5$ fibre mirror with a large $R_2/L \approx 1$ mirror, i.e. the bottom right corner of this heatmap, yields a $<$ 10MHz decay rate κ even with a set cavity misalignment M_{ax} of 8.64μm.

	Sym	**Asym 1**	**Asym 2**
L(mm)	1.4	1.4	1.63
$R^{(1)}_{mir}(\mu\text{m})$	70	70	70
$R^{(2)}_{mir}(\mu\text{m})$	70	140	140
$-R_1/L$	0.5166	~ 0.5	~ 0.5
R_2/L	0.5166	0.9962	0.9949
$W_0(\mu\text{m})$	5.87	4.82	5.58
$L^{(1)}_m$(mm)	0.7	0.6	0.7
$F \times 10^{-3}$	33.7	33.7	28.9
κ (MHz)	10	10	10
γ (MHz)	$11.2(2\pi)$	$11.2(2\pi)$	$11.2(2\pi)$
g (MHz)	309.8	377.9	302.4
C	68.2	101.4	65.0

Table 3.2: The properties of fibre tip cavities and asymmetric cavities when perfectly aligned. Note that finesse, cavity decay rate, and cooperativity are calculated only using the clipping losses.

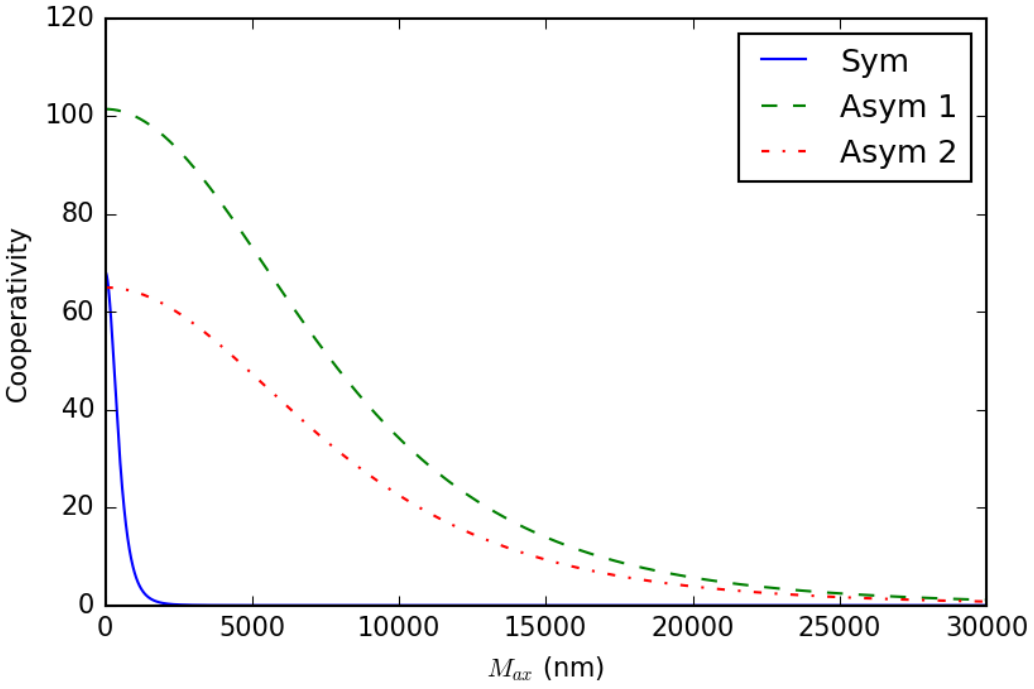

Figure 3.20: Comparison of the cooperativity of the symmetric fibre tip cavity with the asymmetric cavities Asym 1 and Asym 2 (parametrised in Table 3.2) under axial misalignment.

3.5 Optimal Fibre-tip Parameters

To analyse the overall performance of our cavity in Figure 2.4 we need to consider the transmission of light between the fibre and the cavity. In order to do this we first need to set a mirror reflectivity, R, and by extension a transmissivity, $T = 1 - R$, as well as absorption losses, A_b, and scattering losses, S_c, for the cavity mirrors. Considering all of these losses will allow us to look for the optimal parameters for our fibre-tip cavity to be used in ion-trap based quantum information processing. The clipping loss of mirror 1 is,

$$\epsilon_{cl1} = (1 - \rho_{m1}), \tag{3.31}$$

where ρ_{m1} is the fraction of light which hits mirror 1. The loss due to scattering, absorption, and mode mismatch between the fibre and mirror 1 is

$$\epsilon_{m1} = \rho_{m1}(T_{m1}(1 - \eta_{m1}) + A_b + S_c), \tag{3.32}$$

where η_{m1} is the coupling efficiency between mirror 1 and the fibre. Finally the losses due to coupling with the fibre mode of mirror 1 can be found by

$$\epsilon_{t1} = \rho_{m1} T_{m1} \eta_{m1}. \tag{3.33}$$

Next the same losses of the second mirror need to be considered. This can be done using the parameter ζ as the percentage of light not lost at mirror 1,

$$\zeta = 1 - (\epsilon_{cl} + \epsilon_{m1} + \epsilon_{f1}), \tag{3.34}$$

then going through the same process as mirror 1 to get clipping loss,

$$\epsilon_{cl2} = (1 - \rho_{m2})\zeta, \tag{3.35}$$

absorption, scattering, and losses due to cavity-fibre mode mismatch,

$$\epsilon_{m2} = (T_{m2}(1 - \eta_{m2}) + A_b + S_c)\rho_{m2}\zeta, \tag{3.36}$$

and loss due to coupling with the fibre mode at the second mirror,

$$\epsilon_{t2} = T_{m2}\eta_{m2}\rho_{m2}\zeta. \tag{3.37}$$

We can combine all of the above losses to get the overall loss per round trip,

$$\epsilon_{tot} = \epsilon_{cl1} + \epsilon_{m1} + \epsilon_{t1} + \epsilon_{cl2} + \epsilon_{m2} + \epsilon_{t2}, \tag{3.38}$$

and the round trip cavity losses that successfully couple into a fibre mode,

$$\epsilon_{in} = \epsilon_{t1} + \epsilon_{t2}. \tag{3.39}$$

Using eq. (3.39) and eq. (3.38) we are able to calculate the decay rate into the fibre, κ_{in}, and the overall cavity decay rate, κ_{tot}. This allows us to calculate the fraction of the cavity mode that is not lost.

3.5.1 Misalignment

By introducing scattering and absorption losses, of 10PPM and 2PPM respectively [52], and fixing the cavity concentricity, δ, we can calculate the optimal reflectivity for efficient ion-cavity-fibre-cavity-ion transfer. The parameters used for this analysis can be found in Table 3.3.

Parameter	**Value**
L (mm)	1.4
R_{mir} (μm)	70
δ	0.0166
λ (nm)	866
$R_{ef}(\%)$	99.82
S_c (PPM)	10
A_b (PPM)	2

Table 3.3: Cavity parameters used for subsections 3.5.1 and 3.5.2.

Figure 3.21 shows how the axial misalignment, M_{ax}, of the cavity affects the cooperativity, C, and overall cavity→fibre mode coupling efficiency, κ_{in}/κ_{tot}. When $M_{ax} = 1.5\mu$m the cooperativity drops from 6.59 to 2.2 and the coupling into the fibre drops from 0.93 to 0.18. As expected as misalignment increases both cooperativity and useful coupling decreases.

3.5.2 Changing Reflectivity

We can now test how much reflectivity affects cooperativity and amount of loss for the cavity system.

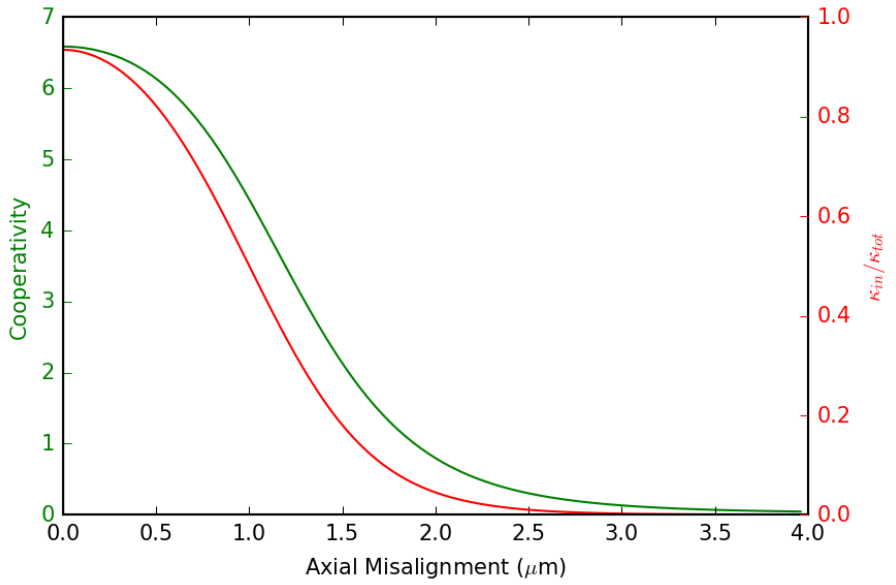

Figure 3.21: Axial misalignment affects the cooperativity and coupling efficiency of the cavity.

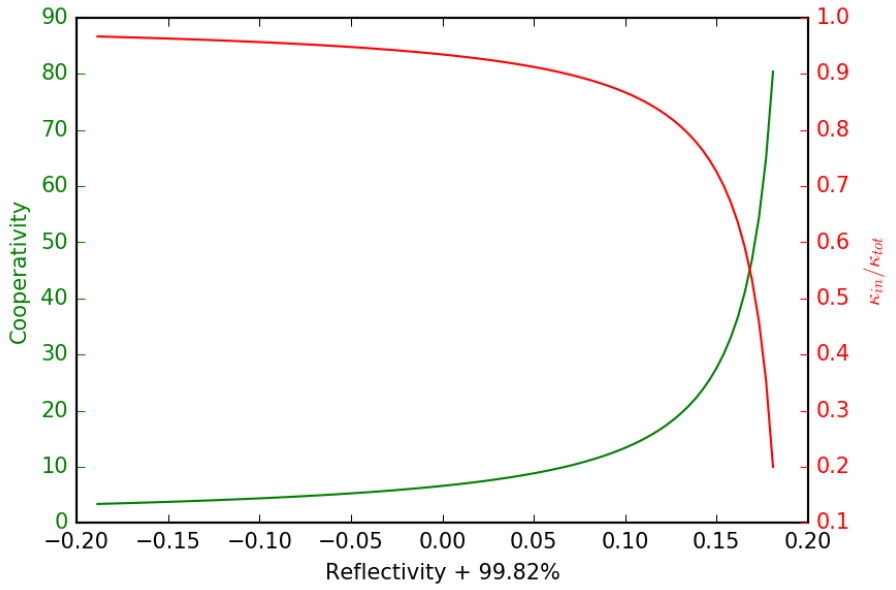

Figure 3.22: The cooperativity and the overall cavity→fibre mode coupling efficiency of the cavity shown in Figure 2.4 with mirror reflectivity around $R_{ef} = 99.82\%$.

Figure 3.22 shows how altering the reflectivity of the mirrors affects the cooperativity, C, and overall cavity→fibre mode coupling efficiency, κ_{in}/κ_{tot}. We can see that by increasing the reflectivity, R_{ef}, from $99.82\% \rightarrow 99.92\%$ of the cavity mirrors we can increase the cooperativity, C, of the system from 6.59 to 13.37. However, this increase in reflectivity decreases the overall cavity→fibre mode coupling efficiency, κ_{in}/κ, from 0.93 to 0.87. This is because the rate of decay into the fibre mode decreases but the rate of decay due to the cavity losses remains the same meaning that the losses take up

a larger fraction of the cavity decay. Therefore, the optimal reflectivity must strike a balance between cooperativity and cavity→fibre efficiency. The reflectivity $R = 99.82\%$ was chosen for this analysis since it provided the optimal balance between C and κ_{in}/κ_{tot}, whilst keeping the concentricity, δ, as discussed in the following section.

3.5.3 Optimal Radius of Curvature

Since the goal of our network is to transfer a photon from one ion to another via the use of cavities we can find the chance of successful state transfer with

$$O = \left(\frac{2C}{1+2C}\frac{\kappa_{in}}{\kappa}\right)^2, \tag{3.40}$$

where $2C/(1+2C)$ is the efficiency of storage or retrieval of a photon from an ion [86] [87] [71]. This makes O the efficiency of storage, retrieval and mode coupling which are the processes used in a quantum network which can be most altered by the cavity parameters. Therefore, by maximising eq. (3.40) we should find optimal cavity parameters for cavities in a quantum network.

Using eq. (3.40) we are able to numerically evaluate the optimal values for both the radius of curvature for the mirrors and the reflectivity of the cavity mirrors. Figure 3.23 shows the chance of success, O, heat map of possible combinations of reflectivity, R_{ef}, and concentricity, δ, parameters for a cavity-atom system with fixed length L, mirror size R_{mir}, wavelength λ, and atom spontaneous decay γ. These parameters were fixed due to the minimum cavity length before disturbing the ion-trap[36], the size of the single mode fibre, and the choice of atom. By doing this we can obtain the parameters which obtain the maximum chance of success of $O = 0.893$, with the parameters $\delta = 0.0418$ and $R_{ef} = 99.95\%$.

By fixing the concentricity at $\delta = 0.0418$ and changing only the reflectivity, R_{ef}, we can see in Figure 3.24 how fabrication errors in mirror reflectivity may change the performance of the system. Starting with a reflectivity of 99.95% we obtain a chance of success value of $O = 0.893$. When the reflectivity is 99.91% the chance of success drops to $0 = 0.874$, and when the reflectivity is 99.99 the chance of success drops to $0 = 0.679$. At higher reflectivities this drop in O is due to the light being trapped in the cavity for too long so the clipping, scattering, and absorption losses become more dominant. Whereas, having a lower reflectivity allows more light to couple into the right fibre mode but the light also has a higher chance of leaving the cavity before interacting with the atom. This is why overall a balance must be made between R_{ef} and δ to obtain the maximum possible transfer efficiency between networked ions.

Figure 3.25 shows how the cooperativity and mode coupling efficiency of the optimised cavity behave with errors in reflectivity. Initially under optimal conditions we obtain

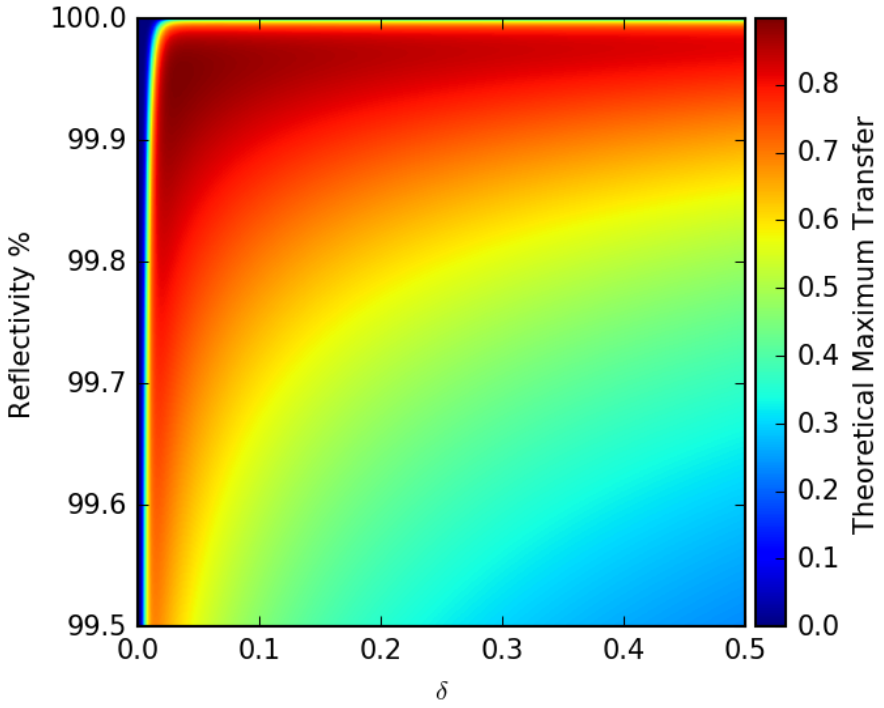

Figure 3.23: The maximum possible theoretical transfer of a cavity-fibre-cavity system when changing just concentricity and reflectivity of the system. This can be used to calculate the optimal parameters when the mirror size and cavity length are fixed. Note that this graph only has one maximum, as such it is possible to use a gradient accent algorithm to find the best parameters without worrying about local maxima.

a cooperativity of $C = 17.14$ and cavity→fibre mode coupling efficiency of $\kappa_{in}/\kappa_{tot} = 0.972$. However, at reflectivities of $R_{ef} = 99.91\%$ and $R_{ef} = 99.99\%$, the cooperativity is $C = 9.24$ and $C = 106.8$ respectively and the overall cavity→fibre mode coupling efficiency is $\kappa_{in}/\kappa_{tot} = 0.985$ and $\kappa_{in}/\kappa_{tot} = 0.828$, respectively.

Figure 3.26 shows how the cavity is affected by misalignment. For the cooperativity and the overall cavity→fibre mode coupling to fall by 50% the cavity may be axially misaligned by 3.65μm or 2.75μm respectively. Since we have to look at both values together we can calculate that this corresponds to a chance of success, O, of 0.232 and 0.038 at 2.75μm at 3.65μm axial misalignment, respectively.

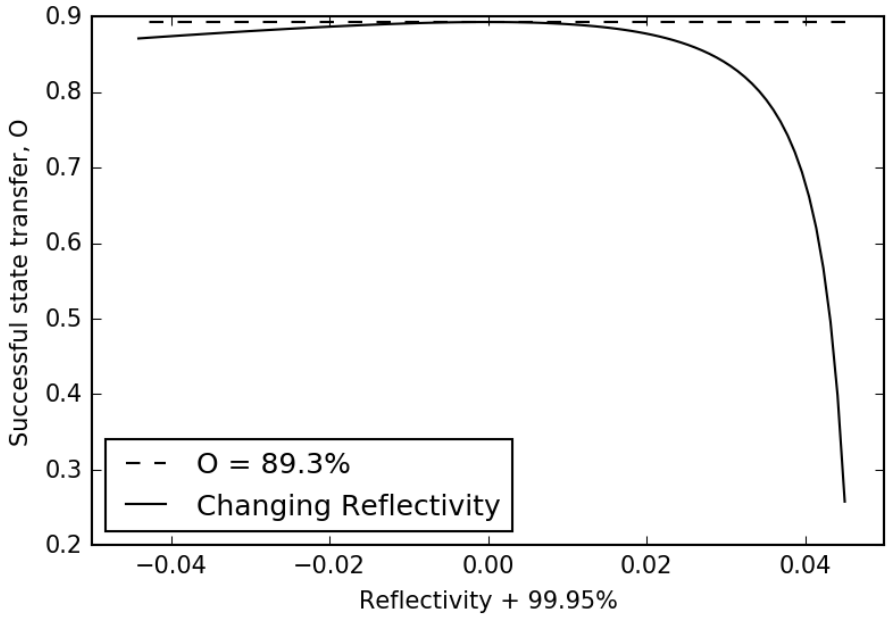

Figure 3.24: Successful state transfer of O from eq. (3.40) versus mirror reflectivity. Here we have a fixed concentricity parameter of $\delta = 0.0418$ so we can see how varying just the reflectivity from its optimum affects the system.

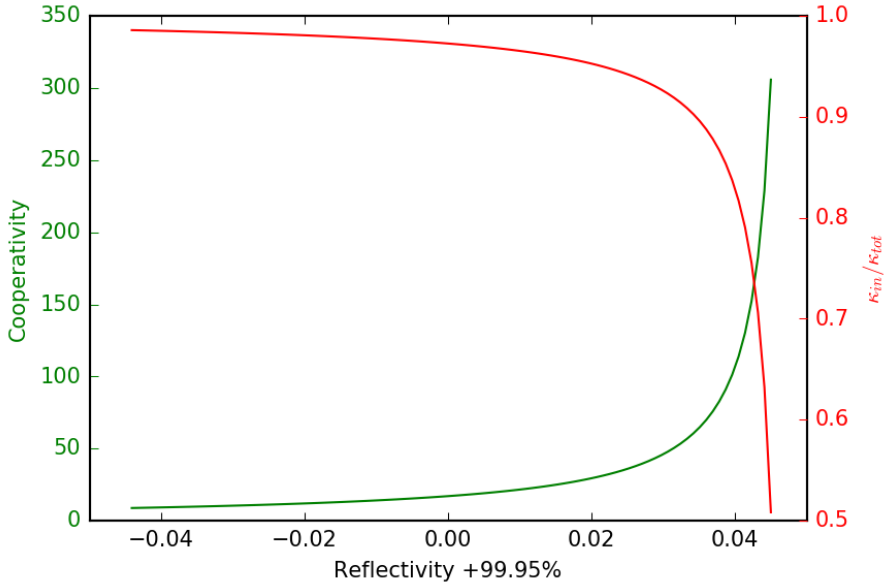

Figure 3.25: The cooperativity and the overall cavity→fibre mode coupling efficiency of the cavity shown in Figure 2.4. The mirror reflectivity at the optimal value of O is $R_{ef} = 99.95\%$ and the concentricity fixed at $\delta = 0.0418$. These were used to calculate the chance of success in Figure 3.24.

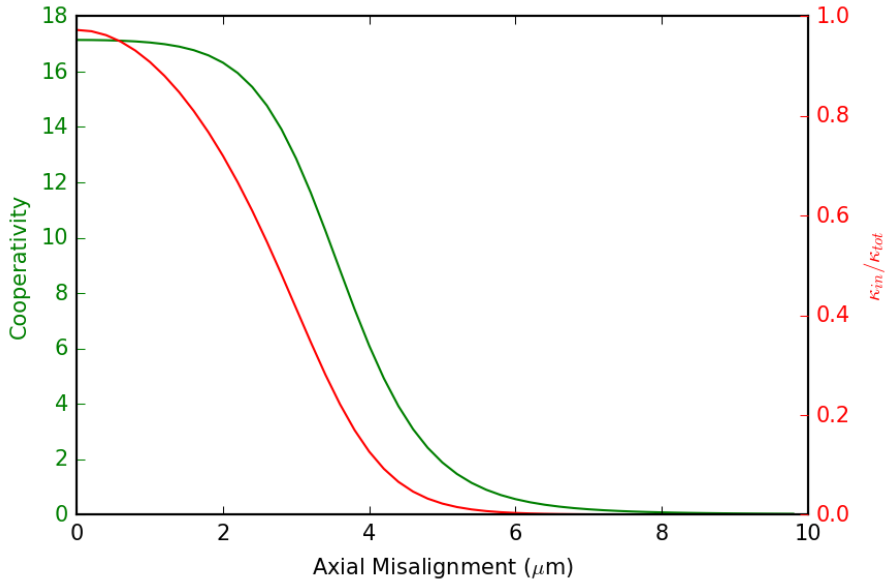

Figure 3.26: The cooperativity and the overall cavity→fibre mode coupling efficiency of the cavity shown in Figure 2.4 with axial misalignment including realistic cavity losses given in Table 3.3.

3.6 Summary of Section

This section has analysed how FP cavities behave under both axial and rotational misalignment, and analysed the performance of those cavities. By taking into account all cavity losses and coupling efficiencies and looking at the end use case of networking ions we were able to find the best parameter set for the cavities that are integrated into ion-traps. For a fixed cavity length, L, of 1.4mm and mirror size, R_{mir}, of 70μm we obtain a maximum transfer chance, O, of 0.893 when operating at a concentricity, δ, of 0.0418 with a mirror reflectivity, R_{ef}, of 99.95%. This assumes the scattering and absorption losses of the mirror are 12PPM.

However, to get a full understanding of the ion-cavity-fibre-cavity-ion system we cannot just look at the ion-cavity interactions but also need to consider the details of the incoming pulse from the fibre to the cavities. The next chapter will look at transferring a photon from one cavity to another via the use of an optical fibre, how the shape of the photon pulse affects this transfer, and how the cavity losses discussed above affect state transfer in this more detailed model.

Chapter 4

Ion-Ion State Transfer

This chapter will look at the networking of cavities with a single mode optical fibre. Then, we will introduce Ca^{40} ions into the model to analyse ion-ion state transfer. Section 4.1 will look at networking cavities with an optical fibre and how time reversal of a pulse can massively enhance transfer into a second cavity. This is a building block in our model which helps to show that near deterministic transfer is theoretically possible for a system without losses. Next, in section 4.2 we will look at how a different shape of a single photon wavefunction affects its absorption into an empty cavity, which will show that wavefunctions other than the time reverse can show an improvement in state transfer over natural emission; however the time reversed wavefunction is still the most optimal.

In section 4.3 we add an ion into one cavity with its $|e\rangle \leftrightarrow |x\rangle$ transition driven by a laser. This allows us to model the STIRAP technique for shaping a single photon pulse so we can add realistic losses to our simulations. Section 4.4 now takes this further by seeing how we can achieve optimal ion-ion state transfer by using a second laser on the receiving ion to drive absorption. This section uses the optimised parameters from Chapter 3 to analyse the system under a full simulation and tests how tolerant these parameters are to errors. Finally, section 4.5 will conclude the chapter with a summary of the chapter.

4.1 Networking Cavities

4.1.1 The Basic System

To build our model we start off looking at the system shown in Figure 1.2 without the ions. This model now consists of two cavities connected by a long optical fibre. By starting with this system we will be able to add complexity and test the system at various stages to gain insights about how the network behaves in its simplest form without losses to a simulations that models how the network should behave in the real world.

Our initial basic model, as derived in Section 2.3, used a long fibre with hundreds of longitudinal modes which is necessary for the single photon pulse to be shaped. This model was created using the Hamiltonian derived in eq. (2.65). Assuming we are dealing with pure quantum states with a single photon then the system can be written as

$$|\Psi\rangle = a\,|1,0,0...0\rangle + b\,|0,1,0...0\rangle + \sum_k c_k\,|0,0..1_k..\rangle\,, \tag{4.1}$$

where $|a|^2$ and $|b|^2$ define the population of the first and second cavities and $|c_k|^2$ is the population of the kth fibre mode. Using the Schrödinger equation [88],

$$i\hbar\frac{d}{dt}\,|\Psi\rangle = \hat{H}\,|\Psi\rangle\,, \tag{4.2}$$

yields the dynamics of the system:

$$\dot{a} = -i\Delta_a a - i\eta_a \sum_k c_k \tag{4.3}$$

$$\dot{b} = -i\Delta_b b - i\eta_b \sum_k (-1)^k c_k \tag{4.4}$$

$$\dot{c_k} = -i\Delta_k c_k - i(\eta_a a + \eta_b(-1)^k b) \tag{4.5}$$

This was then solved for 1224 fibre modes with a single photon contained entirely in the first cavity ($a = 1$, $b = 0$, $\sum^k c_k = 0$). This used the ODE solver in the python package scipy.

The next step was to graph the wave function of the single photon pulse in real space. In eq. (2.39) the electric field inside the fibre as a sum of fibre modes is shown. By

defining the detuning with respect to the fundamental cavity mode and normalising the amplitude of the electric field we obtain

$$\psi(x) = \sum_n c_{k(n)} \sin\left(\frac{\pi}{l} k(n) x\right) \tag{4.6}$$

This function is then converted into the pulse shape by

$$F(x) = |\psi(x)|^2 , \tag{4.7}$$

where $F(x)$ is proportional to the intensity distribution of the pulse. The simulation was then done with a single photon starting completely in the first cavity and the dynamics observed resulting in Figure 4.1 below.

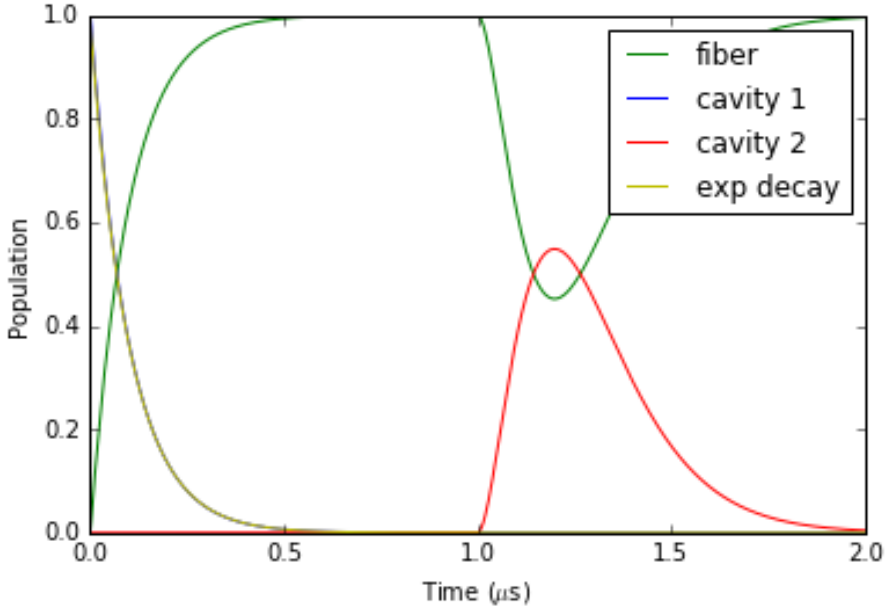

Figure 4.1: The evolution of the basic system showing how the distribution of the single photon evolves over time. The decay from cavity 1 is compared with the expected exponential decay from a cavity in free space to test consistency. This was done with a fibre length of 300m, 320 modes, 1.55μm wavelength light, and a cavity decay rate of 10MHz.

In Figure 4.1 the decay of the cavity photon into the fibre modes is calculated, and compared with the expected exponential decay, using Fermis golden rule. This decay is compared to the expected exponential decay to verify that we have calculated the correct coupling strengths. The population for the cavity a and b was calculated with $|a|^2$ and $|b|^2$, respectively, the population of the fibre was calculated by $\sum_k |c_k|^2$. As can be seen at roughly $0.5\mu s$ the photon is (almost) completely within the fibre. The pulse shape for

such a decay is a decaying exponential shape which can be seen in Figure B.1(a) of the appendix. This pulse propagates through the fibre until it reaches the second cavity at $1\mu s$ where it is partially absorbed and partially reflected. The absorption of the pulse in this system is roughly 54% and the rest is reflected back towards the first cavity.

4.1.2 Time Reversal

To test the time reversal argument made by M. Stobinska [76] in our model we flip the naturally emitted photon pulse in the fibre to produce the time reverse of the emitted pulse. This was done by waiting until the photon was completely in the fibre and then applying the following transform[77]

$$\psi(k)_{flipped} = -(-1)^k \psi(k)^{\star}_{normal}. \tag{4.8}$$

This allowed for the pulse to be flipped but to continue propagating in the same direction. This time reverse pulse, which can be seen in Figure B.1(b), evolves according to Figure 4.2 below.

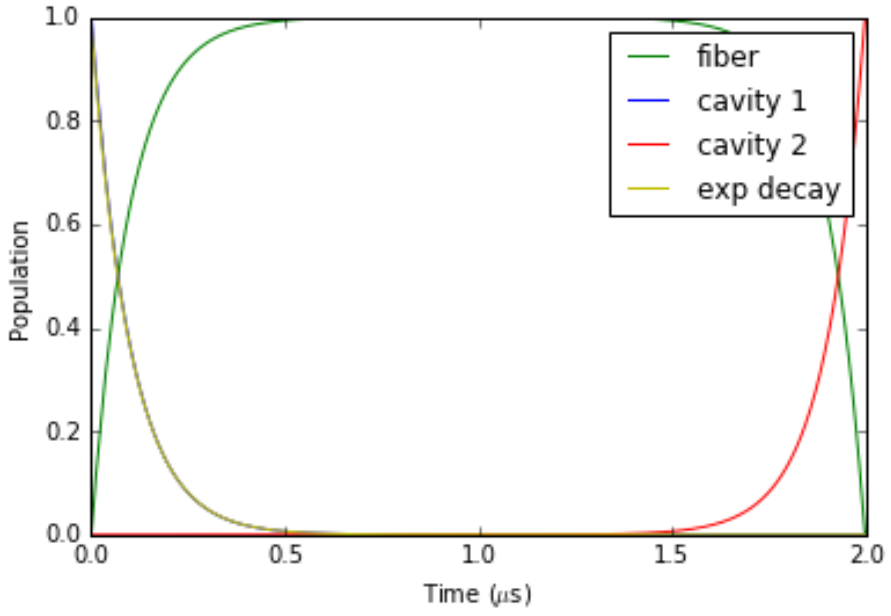

Figure 4.2: The evolution of this system shows a cavity decaying naturally until the photon is completely within the fibre, then at $1\mu s$ the transform from (4.8) is applied. The dynamics after $1\mu s$ shows how a time reverse pulse can be completely absorbed by a cavity. This was done with a fibre length of 300m, 320 modes, 1.55μm wavelength light, and a cavity decay rate of 10MHz.

In this model the pulse was flipped after exactly $1\mu s$ of time as the front of the pulse would have been just about to enter the second cavity with our fibre length. This allowed

as much of the pulse to enter the fibre as possible before flipping it around. This flipped pulse was absorbed by the cavity 2 with nearly a 100% chance, as was expected from literature[76] [79].

Thus a basic model of the system shown in Figure 1.2 has been created with the dynamics shown in Figure 4.1. Here the photon leaks out of cavity 1 with exponential decay, travels through the fibre to cavity 2 where part of it is absorbed and part of it is reflected. The argument of time reversing the dynamics for 100% absorption from literature also holds in this model[76] [79][77] as seen in Figure 4.2 where the photon is completely absorbed by cavity 2. Next we look at how to shape the photon into any arbitrary shape so that we can test how the system performs for different pulses and verify our system against known literature.

4.2 Single Photon Wavefunction Shapes for Absorption by an Empty Cavity

In order to test how shaping the wave function of the photon affects its absorption into a cavity, a simulation was created where a photon with a wave packet of a desired shape was placed in the fibre and allowed to propagate towards the second cavity. This system is shown in Figure 4.3.

Figure 4.3: Pulse starting in the fibre moving towards an empty cavity.

To create a pulse with any arbitrary shape first the transformation to switch between the time domain to the frequency domain must be calculated. Since the pulse shape in the fibre is given by (4.6),

$$\psi(x) = \sum_k c_k \sin\left(\frac{\pi k x}{l}\right), \tag{4.9}$$

in order to calculate the frequency space coefficients c_k, discrete sin transformations (DST) are used [89].

Once the shape had been generated in order to model a population of a single photon the shape was normalised with

$$\psi(k) = \frac{\psi(k)}{\sqrt{\sum_k |\psi(k)|^2}}. \tag{4.10}$$

This was done to make the overall population of the modes equal to 1. Shaping a pulse in this way allows for studying the absorption of various single photon shapes.

Now the model is able to test how changing the pulse shape affects the dynamics of the system. Figure 4.4 shows the maximum absorption of a single photon by shape. These values are consistent with the maximum absorption found in literature showing near exact replication[79]. The properties of the shapes used can be seen in Table 4.1.

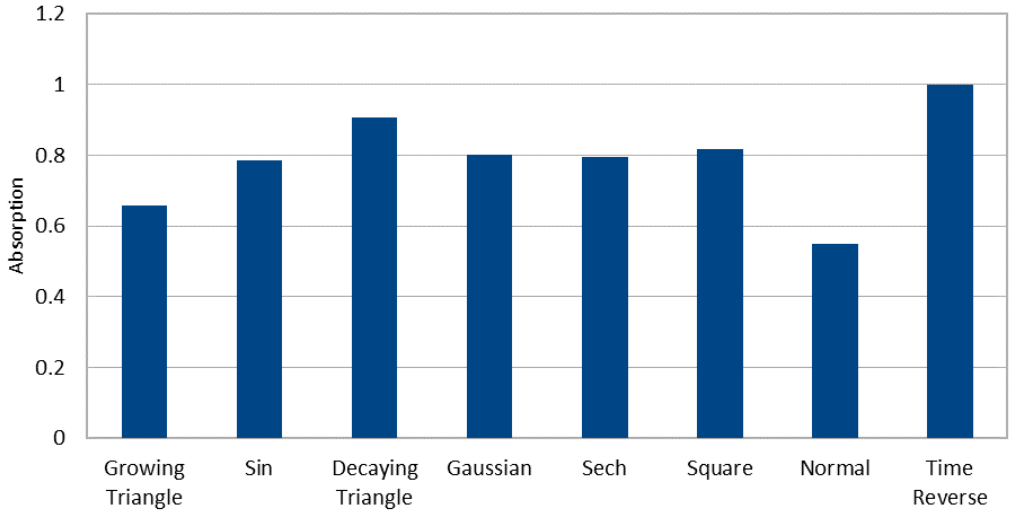

Figure 4.4: Maximum absorption into a cavity by different pulse shapes. The full details of these shapes can be found in Table 4.1 and and plotted in appendix B. These results were calculated with a fibre length of 300m, 320 modes, 1.55μm wavelength light, and a cavity decay rate of 10Mhz.

Name	**Formula**	**Validity**
(a) Natural decay	$5.06e^{\frac{x}{27m}}$	$-\infty \leq x < 0$
(b) Time reverse	$5.06e^{\frac{-x}{27m}}$	$0 \leq x < \infty$
(c) Growing triangle	$\frac{x}{75m}$	$0 \leq x \leq \frac{l}{2}$
(d) Decaying triangle	$\frac{-x}{75m} + 2$	$0 \leq x \leq \frac{l}{2}$
(e) Sin	$\sin\left(\frac{2\pi x}{l}\right)$	$0 \leq x \leq \frac{l}{2}$
(f) Gaussian	$e^{-\frac{2\left(x-\frac{l}{4}\right)^2}{\left(\frac{l}{4}\right)^2}}$	$0 \leq x \leq \frac{l}{2}$
(g) Square	1	$0 \leq x \leq \frac{l}{2}$
(h) Sech	$\text{Sech}\left(\frac{200x}{9l} + 5\right)$	$0 \leq x \leq \frac{l}{2}$

Table 4.1: This table shows the properties of the pulse shapes used for Figure 4.4. These pulses can be can be seen in Chapter B.

The shapes were calculated to have a width optimal for absorption by the second cavity. When testing with other cavity decay rates we found the same maximum absorption

occurred if the width of the shaped pulse were varied by the same factor as the new naturally decaying pulse FWHM to its old FWHM. Larger and shorter lengths were tested around this value to test optimisation of the pulse. By comparing these results with the literature [79] we are able to verify that the model created is working as expected.

In Figure 4.5 the full dynamics of a few time symmetric shapes can be seen. For each shape the pulse was placed in the fibre between $x = 0$ and $x = l/2$, centred around $x = l/4$. The pulse then propagated towards cavity 2 where the front of the pulse reaches the cavity at time 0.5μs. The pulses are absorbed reaching a maximum population in cavity 2 at about 0.8μs and then begin to decay back into the fibre. Then at 1.5μs the pulse has been completely emitted by the cavity back into the fibre.

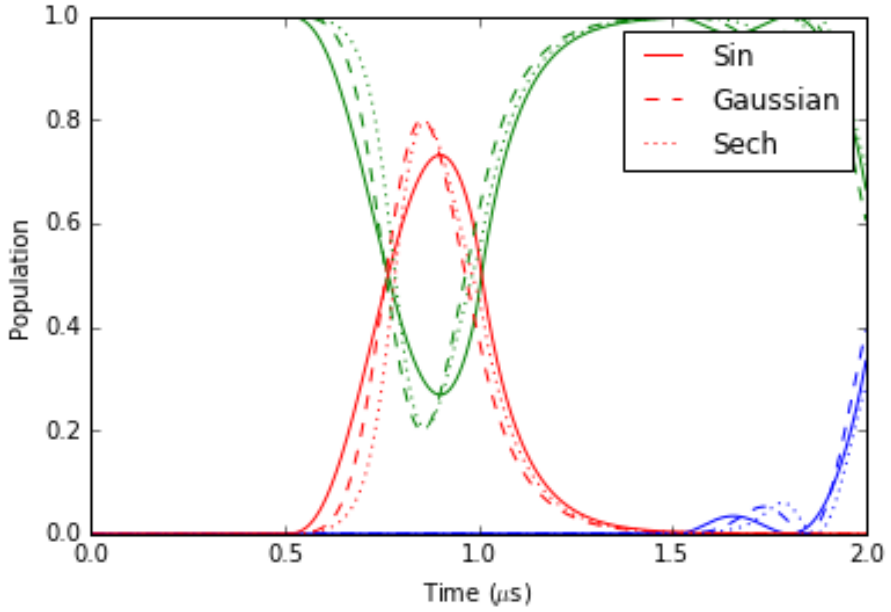

Figure 4.5: The dynamics of a system with a few different pulse shapes, as given in Table 4.1 and and plotted in appendix B. Red indicates population of cavity 2, thus showing the absorption into the cavity, whilst green is the population of fibre modes. This was done with a fibre length of 300m, 320 modes, 1.55μm wavelength light, and a cavity decay rate of 10MHz.

Time symmetric pulses are of extreme interest since they are their own time reverse. This means that if a cavity can be designed to emit such a pulse then it should be able to also fully absorb such a pulse; flipping the pulse would not be needed.

With this model we will now analyse the effects of using a 3-level atom and a laser to shape the single photon pulse in an actual experiment and see how this might affect the performance of our network.

4.3 Pulse Shaping using STIRAP

Before we are able to build a full working model of a ion-cavity-fibre-cavity-ion network we need to introduce ions into the cavities. For this we used the physics discussed in Section 2.4.1 to add a 3-level Ca^{40+} ion with the $|e\rangle \leftrightarrow |g\rangle$ transition driven by a Raman process including one laser and one cavity photon. Once the model was coded we were able to test the system, using parameters from literature[71], to create shaped pulses in the fibre from the one photon-ion-cavity-fibre system. Considering all losses Figure 4.6 shows how much of the shaped pulse we can expect to successfully enter the fibre. To create this figure we used an ion-cavity coupling strength of $g = 30\pi$MHz, a spontaneous decay rate of $\gamma = 6\pi$MHz, and a cavity decay rate of $\kappa = 4\pi$MHz. The single photon shape is created using a laser pulse driving the ion, the laser pulse is described by $\Omega(t) = gt/1\mu$s, notice that $\Omega(t)$ increases with time, this is because the ion needs to be driven harder as its excitation probability decreases to maintain or increase the shape of the emitted photon.

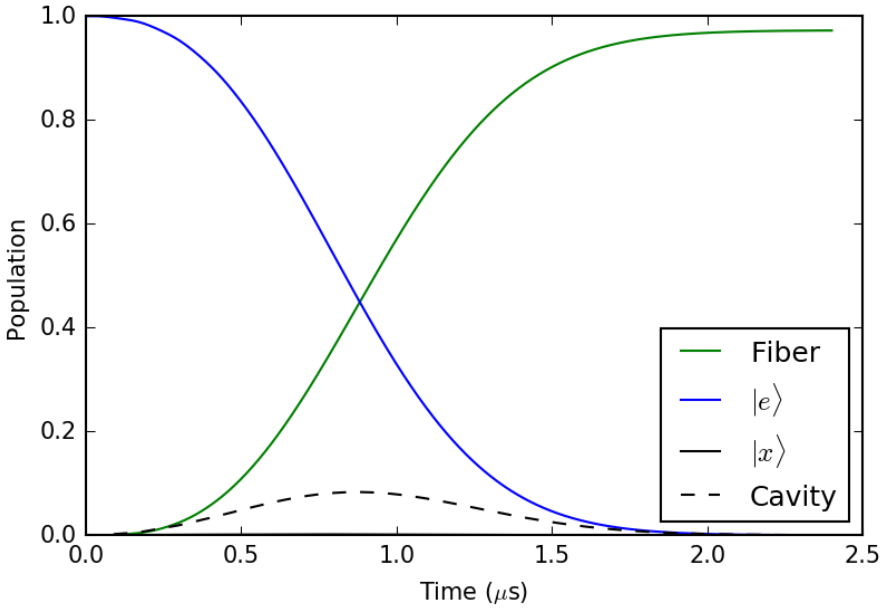

Figure 4.6: Dynamics of a ion-cavity-fibre system. Using the parameters from literature, the ion-cavity coupling strength is $g = 30\pi$MHz, the spontaneous decay rate is $\gamma = 6\pi$MHz, and the cavity decay rate is $\kappa = 4\pi$MHz. Along with a laser pulse of $\Omega(t) = gt/1\mu$s. Here the green solid line shows the population of the fibre, the blue solid line represents the population of the $|e\rangle$ ion energy level, the black solid line shows the population of the $|x\rangle$ ion energy level, and the black dashed line shows the population of the cavity.

Figure 4.6 shows a probability of emission in to the fibre of 97% which agrees with current literature. By comparing the results of our model against [71] we are now able to implement the full ion-cavity-fibre-cavity-ion system for analysis. However, rather

than simply analysing current systems the next section will use the restrictions set by the ion trap to find the optimal cavity parameters for efficient state transfer.

4.4 Optimal state transfer

Using the optimal cavity parameters calculated in Chapter 3 combined with the pulse shaping techniques and time reversal argument we are able to calculate the optimal state transfer for a set cavity length, mirror size, and wavelength as given in Table 4.2.

Parameter	**Value**
L (mm)	1.4
R_{mir} (μm)	70
Sc (PPM)	10
Ab (PPM)	2
λ (nm)	866
γ (Mhz)	$11.2(2\pi)$
l (m)	600

Table 4.2: System parameters used throughout Section 4.4

4.4.1 Driving Single Photon Absorption

Using the time reversal argument and the STIRAP shaping technique, we are able to drive the absorption of an incoming photon of known shape with the right laser pulse. In our system this can easily be done by using the time reverse of the shaping laser pulse on the ion after a delay equivalent to the photon travel time in the fibre,

$$t_D = \frac{nl}{c}, \tag{4.11}$$

where n is the group index of the fibre mode. This results in the incoming photon having the exact time reversed conditions as when it was emitted from the first cavity which causes full absorption.

For the simulations we have chosen a Gaussian shape pulse with a Full Width Half Maximum (FWHM) of 141.3m as seen in Figure 4.7. This pulse is generated using the laser pulse seen in Figure 4.8 calculated by eq.(2.72).

The Gaussian pulse in Figure 4.7 was chosen due to its symmetry and because it has no sudden sharp features. This makes the required laser pulse, seen in Figure 4.8, easier to generate as it has no sudden intensity spikes. This also makes calculating the laser pulse for the receiving cavity very simple as it is simply the time reverse of the pulse used to generate the shape. This pulse is used for most of the results in Section 4.4.

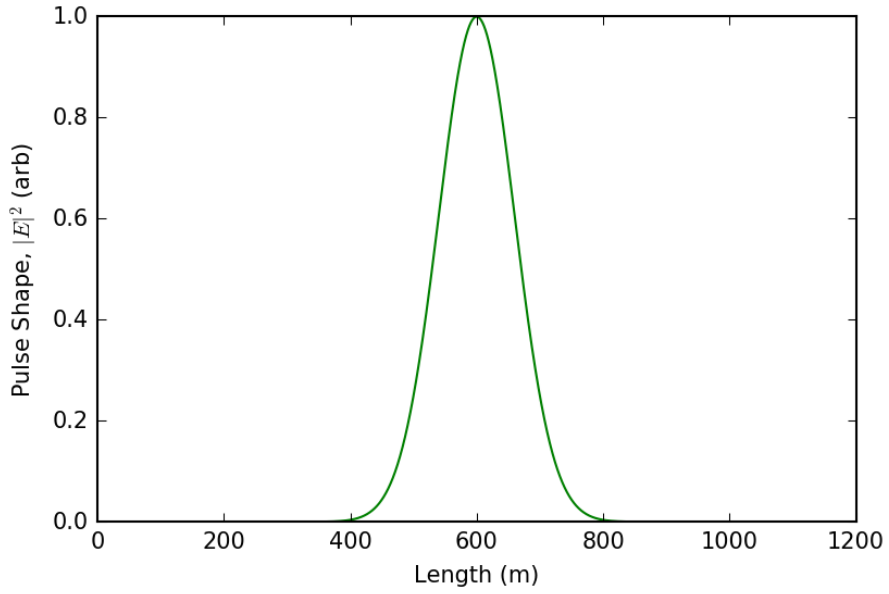

Figure 4.7: A long Gaussian shape with a FWHM of 141.3m was used for the single photon wavefunction in most of the simulations in Section 4.4. The parameters used in this pulse can be found in Table 4.2, with the laser pulse seen in Figure 4.8.

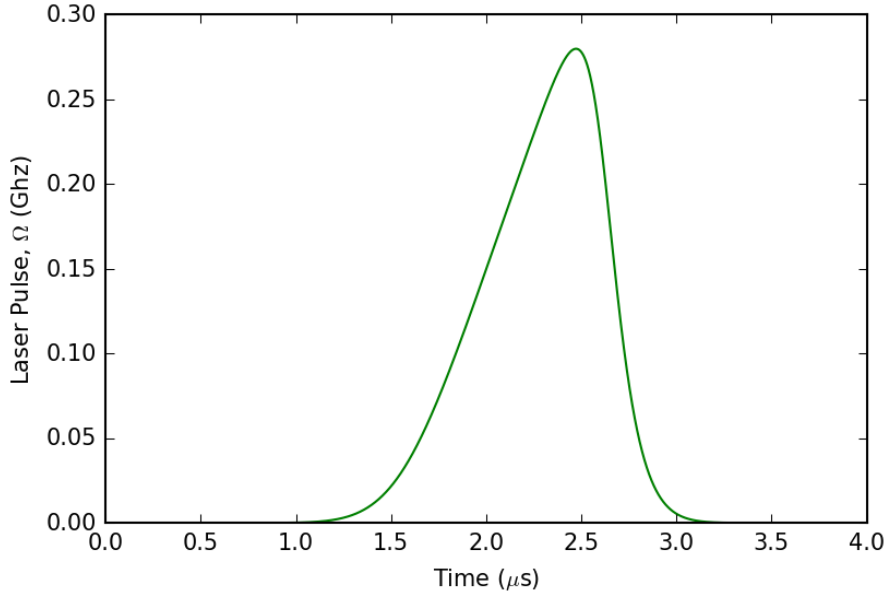

Figure 4.8: Laser pulse shape needed to produce the photon wavefunction in Figure 4.7. Note that there are no sudden transitions making this easier to implement.

4.4.2 Optimal system

Section 3.5 looked at how we can optimise our system under the constraint of set cavity lengths and mirror sizes. This section found the expected optimal reflectivity, $R_{ef} = 99.954$, and concentricity, $\delta = 0.0418$, of our system.

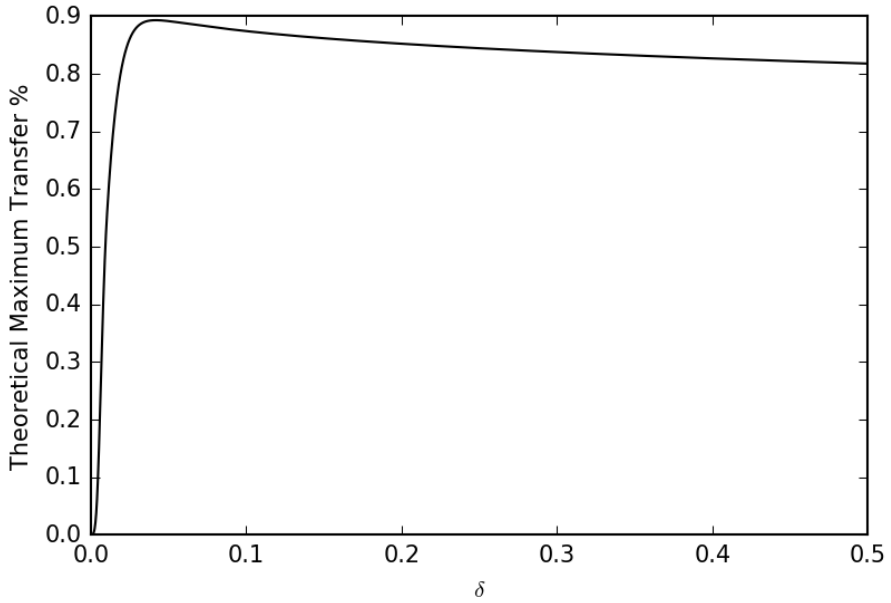

Figure 4.9: The maximum chance of success, O, for the cavity shown in Figure 2.4 with the concentricity of the cavity, δ. Note that the mirror reflectivity at each point on this graph is varied to give the optimal O value. (See appendix C, Figure C.1 for O vs R_{ef})

Figure 4.9 shows the optimal concentricity, for the cavity parameters defined in Figure 2.4, where S_c and A_b are taken as 10PPM and 2PPM respectively [52], of $\delta = 0.0418$. At this value the optimal reflectivity is $R_{ef} = 99.954\%$ yielding a cooperativity of $C = 17.14$, a coupling efficiency of $\kappa_{in}/\kappa = 0.972$, an ion-cavity coupling strength of $g = 248.2$MHz. This yields an overall maximum chance of success of 89.3%.

Section 3.5 achieved its results by optimising our cavities for a single parameter related to the expected transfer efficiency, O. This section will build on this by taking the parameters from Section 3.5 and looking at the full dynamics of the laser-ion-cavity-fibre-cavity-ion-lasers system behaves and how sensitive they are to changes in these optimal parameters. More detail on the steps of this simulation can be found in appendix A.

4.4.2.1 Mirror Size

Assuming perfectly aligned mirrors we can see the optimal ion-cavity-fibre-cavity-ion photon transfer in Figure 4.10. In this graph the parameters have been calculated for optimal transfer for each mirror size by optimising eq.(3.40), these parameters can be seen in Figure 4.11(a). In Figure 4.11(a) we see the optimal reflectivity and concentricity of cavities will different mirror sizes. In general we see that as we use larger cavity mirrors we are able to use more concentric regimes and higher reflectivity mirrors. All of this results in the cavity cooperativity and cavity↔fibre coupling efficiency seen in Figure 4.11(b)

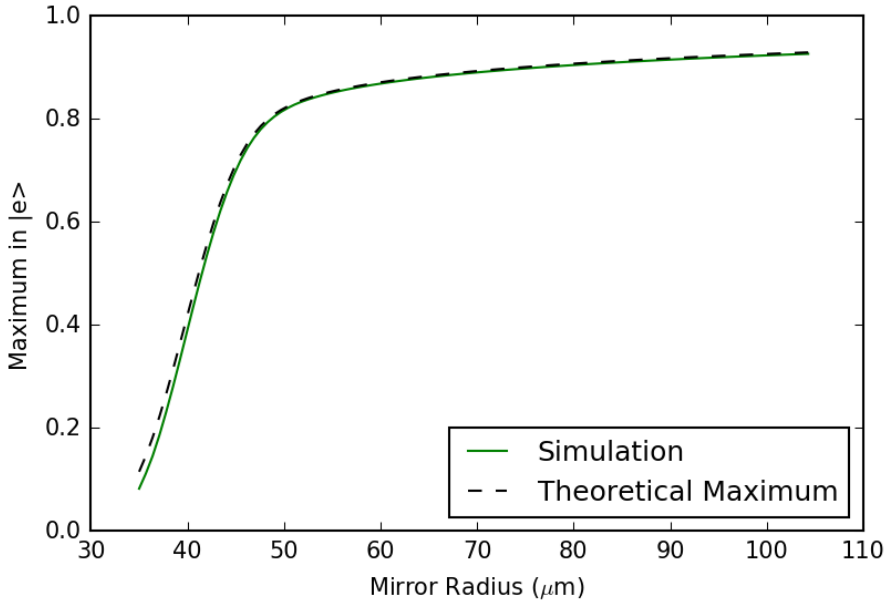

Figure 4.10: Transfer efficiency vs radius of the cavity mirrors. The dotted line represents the expected maximum transfer as calculated from eq. (3.40) and the solid green line represents the results of the full simulation.

From Figure 4.10 we see that the efficiency of photon transfer is heavily dependent on the size of the cavity mirrors, here we see that the larger the mirror the more efficient the transfer. Figure 4.10 shows that as the mirror size, R_{mir}, falls to 41μm the maximum transfer efficiency drops by 50% to 0.445. Given the set wavelength and cavity length we also see that increasing the cavity mirror larger than 50μm starts to yield diminishing returns. The reason for this can be seen from Figure 4.11(a) and Figure 4.11(b), where the clipping losses are becoming less dominant as mirror size increases, therefore the optimal parameters get more concentric. This leads to a larger coupling efficiency which, in turn, leads to the need for lower reflectivity mirrors and thus losses such as clipping, scattering and absorption become less dominant. We can conclude from this that at a mirror size of $R_{mir} = 50\mu$m the clipping losses are less of a factor than the scattering and absorption losses, and that the decrease in reflectivity with the increase in concentricity

is to lower the number of times the light reflects off the mirror, hence also lowering losses caused by scattering and absorption.

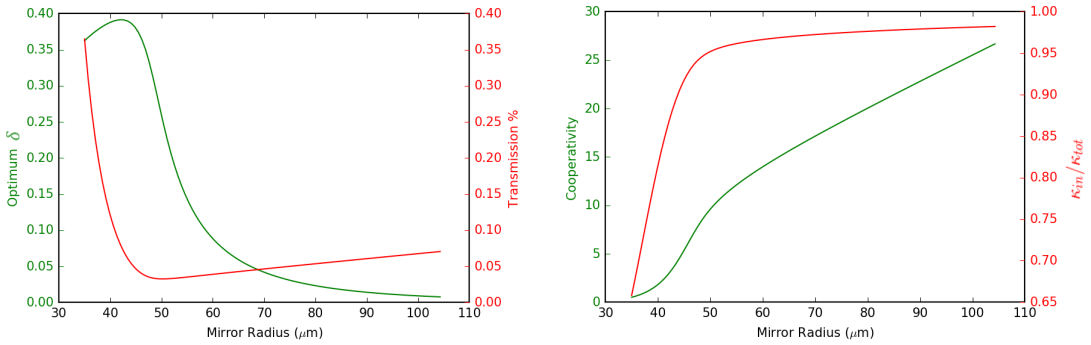

Figure 4.11: In (a) we see the optimal parameters used to calculate the results in Figure 4.10 and in (b) we see the cavity cooperativity and cavity↔fibre coupling efficiency in Figure 4.10

4.4.2.2 Cavity Length

The length of the cavity is very important in determining the optimal mirror parameters. By combining eq. (2.8) and eq. (2.5) with our definition of δ we can find that the beam waist size can be expressed as

$$W_0^2 = \frac{\lambda L\sqrt{\delta}}{\sqrt{2}\pi}, \tag{4.12}$$

and the size of the beam on the mirror can be expressed as

$$W_m^2 = \frac{\lambda L}{2\pi}\left[\sqrt{2\delta} + \frac{1}{\sqrt{2\delta}}\right]. \tag{4.13}$$

Eq. (4.12) and eq. (2.24) clearly show that the coupling strength is inversely proportional to the cavity length, $g \propto 1/L$. Eq. (4.13) and eq. (3.12) show that an increased cavity length will also cause an increased clipping loss due to larger beams on the mirror.

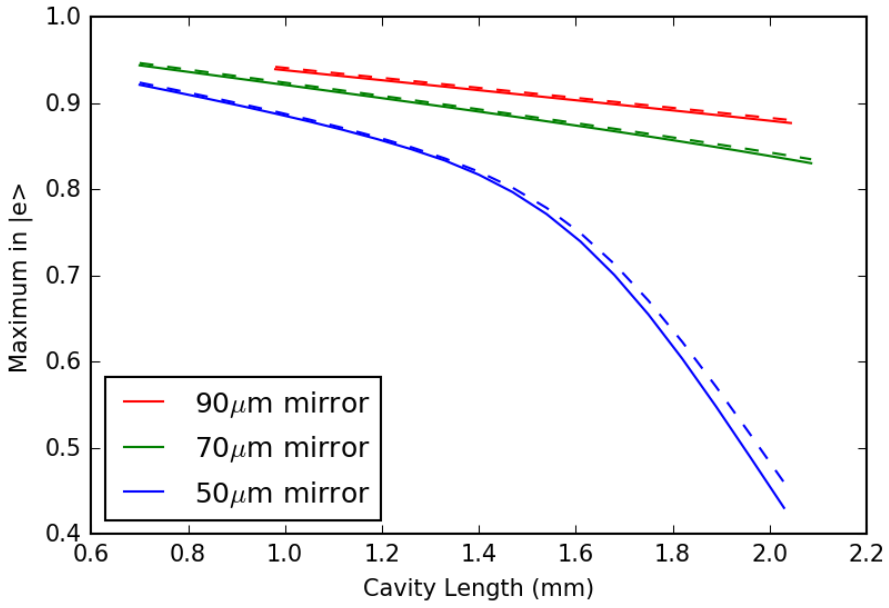

Figure 4.12: Transfer efficiency vs cavity length. Here the dotted lines represent the theoretical maximum transfer, from eq.(3.40), for each mirror size and the solid line shows the simulated results. The red, green and blue lines are for mirrors with radius, R_{mir}, of 90μm, 70μm, and 50μm, respectively. The parameters for each mirror at each cavity length can be seen in Figure D.1, Figure D.2, and Figure D.3 of the appendix.

Figure 4.12 shows how the cavity length changes the optimal performance of cavities with different mirror sizes. The maximum transfer at a cavity length, L, of 1.4mm for the 90μm, 70μm, and 50μm mirror radius is 0.915, 0.890, and 0.817, respectively, falling to 0.903, 0.874, and 0.744 at a cavity length of 1.6mm. We can see from Figure 4.12

that larger cavity mirrors are less affected by increasing cavity lengths. Assuming that we are still able to effectively couple light from a larger mirror to a single mode fibre, this subsection shows that increasing the length of the cavity in exchange for a larger cavity mirror might be a better trade off depending on how much this trade off affects the RF electromagnetic field, and hence trapping time, of the ion trap.

4.4.2.3 Wavelength

This section looks at how using light of different wavelengths would affect the performance of the system. Figure 4.13 shows that larger wavelengths cause an overall less efficient system. At our operating wavelength of 866nm we obtain a maximum transfer of 0.890. However if we increase the operating wavelength to 1550nm then we only achieve a transfer of 0.875. The transfer drops by 50% at a wavelength of 3027nm. On the other hand if we reduce the wavelength of the cavity to 522nm we see an increase in photon transfer to 0.893. However this seems to show diminishing returns as an operating wavelength of 180nm only achieves a transfer of 0.894.

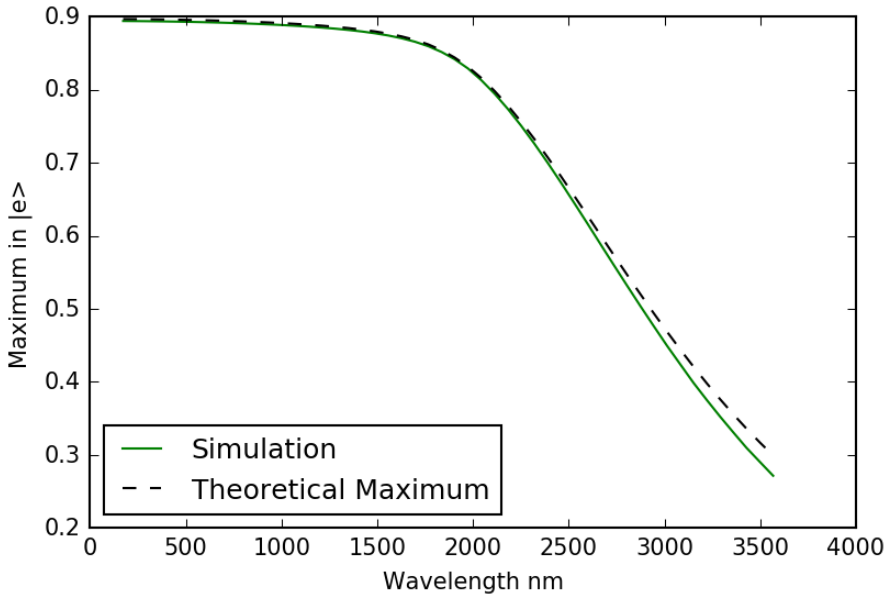

Figure 4.13: Transfer efficiency vs wavelength of light. The dotted line shows the theoretical maximum and the green solid line shows the results of the simulation.

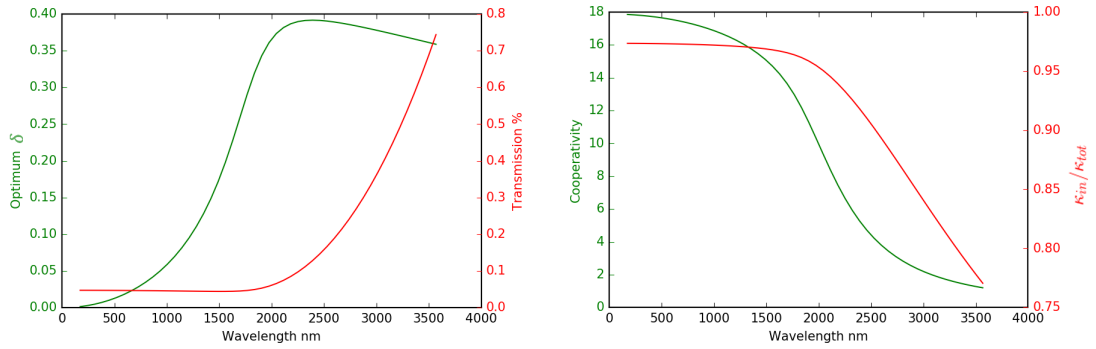

Figure 4.14: (a) shows the parameters for Figure 4.13, and (b) shows the cooperativity and coupling efficiency obtained using the parameters in Figure 4.14(a).

Figure 4.14(a) shows that as the wavelength increases to 2390 nm, the optimal parameters cavity parameters get more confocal to avoid increasing clipping losses. Then, as

the wavelength increases further the optimal parameters start to get more concentric again. This is due to clipping losses having a larger impact on the system, therefore it becomes more optimal to have a lower reflectivity mirror and a higher coupling strength, i.e. the photon and atom interact at a faster time-scale and the photon leaks out at a faster time-scale.

Figure 4.13 was calculated assuming the decay rate of the ion was constant at $11.2(2\pi)$MHz and a changing coupling strength, because we are varying both the wavelength λ and spot size W_0 from eq. (2.24). If we wanted to consider another ion such as Yb^+ using the 925nm transition, as in [90], then we would have to also consider the spontaneous decay rate, $2(2\pi)$MHz, of that atom. Comparing different ions and transitions in this way would be a very useful extension of this research for future projects.

This section also assumes that the the fibre is effectively lossless at any chosen wavelength. In practice this may mean choosing fibres made from different materials or hollow-core fibres.

4.4.2.4 Scattering and Absorption Losses

Two of the major limiting factors in the design of this cavity are the scattering losses and absorption losses of the cavity mirrors. If these were non-existent then a highly confocal cavity with a near 100% reflectivity would be optimal, as seen in Figure 4.16(a), because even with lower coupling strength, g, we would be able to trap the light for a longer period of time to ensure interaction with the trapped ion causing the large cooperativity and coupling efficiency seen in Figure 4.16(b). Unfortunately, these losses are intrinsic to the system and heavily dictate the optimal parameters of the system, as well as its overall efficiency.

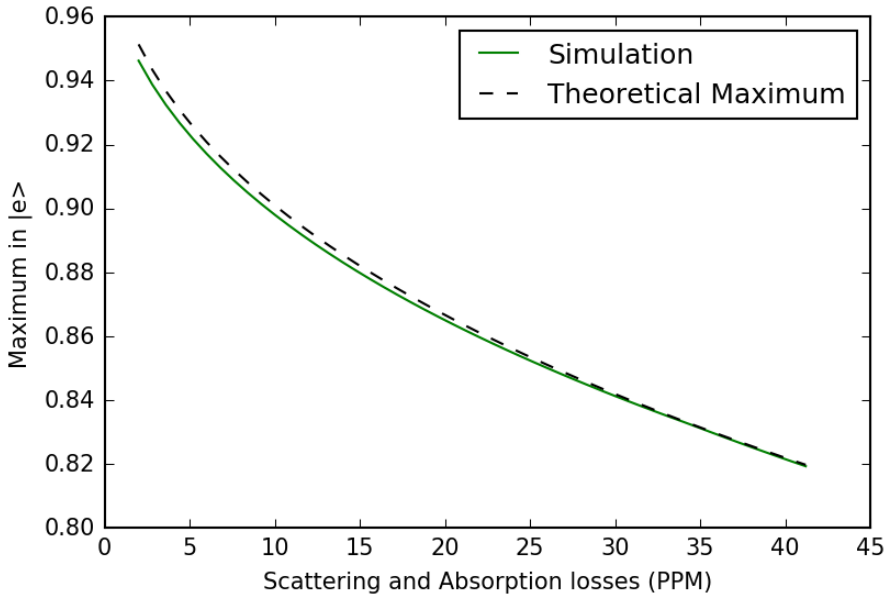

Figure 4.15: Transfer efficiency vs scattering and absorption losses.

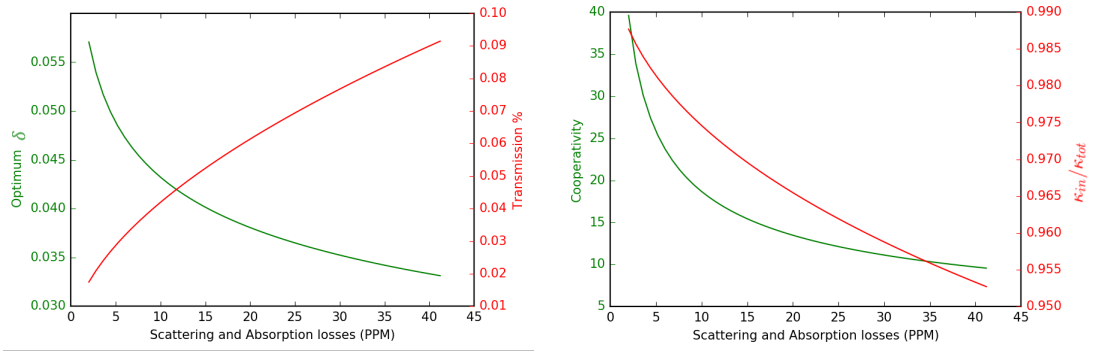

Figure 4.16: (a) shows the optimal cavity parameters as we change the scattering and absorption losses. (b) shows the resulting cooperativity and coupling efficiency when using the parameters shown in (a). The overall ion-ion transfer efficiency can be found in Figure 4.15.

Figure 4.15 shows how altering the scattering and absorption losses of the cavity mirrors affects the maximum ion-ion transfer. Our default system has mirrors with scattering and absorption losses of 12ppm and achieves a transfer efficiency of 0.890. If we halve the losses to 6ppm or double them to 24ppm we achieve a transfer efficiency of 0.917 and 0.855, respectively. This shows that we, obviously, want the lowest possible value for these losses, however we can compensate for high losses by increasing concentricity and decreasing the reflectivity of the mirrors as shown in Figure 4.16(a). This compensation works by speeding up the interaction between the cavity and the ion so that the photon spends less time in the lossy cavity. Doing this may increase the clipping losses per round trip, however this is offset by the shorter number of round trips due to the decreased mirror reflectivity.

4.4.2.5 Fibre Length

In this section we ignore attenuation losses in the fibre to see how the fibre length might affect the physics behind our network and see if there is a optimal length for our fibre.

Figure 4.17 shows what happens if we reduce the length of the fibre, including what happens if we reduce the length of the fibre to shorter than the single photon pulse. The maximum value in this graph is 0.8923 and the minimum is 0.8879. When the fibre is over 300m long the maximum transfer settles at 0.8902. All of these values are slightly lower than the theoretical maximum, $O = 0.8928$, and the variation in overall transfer only has a short range of 0.0044 indicating that the optimal transfer efficiency is independent of fibre length when ignoring attenuation losses. As the frequency spacing, $\Delta\omega$, of the fibre gets larger as the fibre length decreases the coupled frequency modes are less able to properly sample the pulse. At extremely short lengths $\Delta\omega$ may become large enough that effectively only one frequency is coupled to the cavity; this case is known as the short fibre limit.

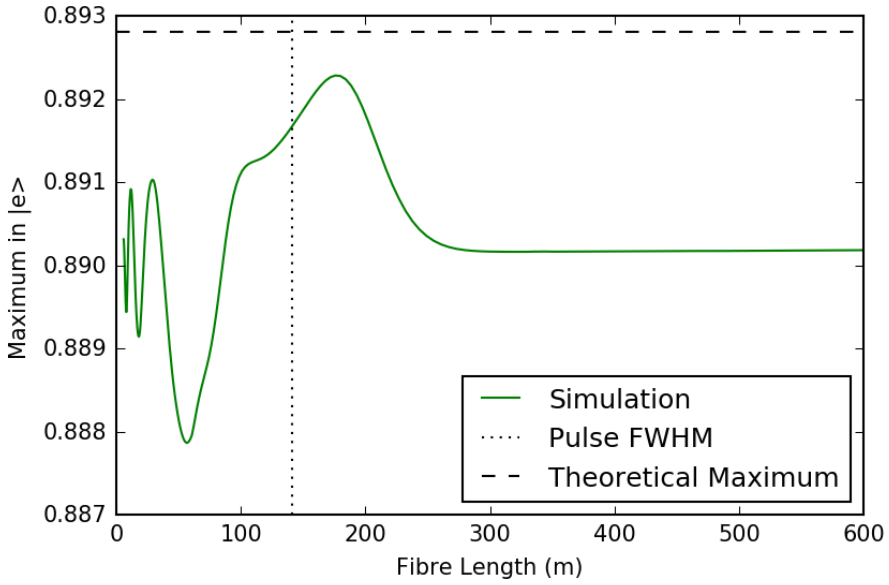

Figure 4.17: Maximum transfer efficiency for changing the fibre size while keeping the laser pulse the same. The vertical dotted line shows the Full Width Half Maximum (FWHM) of the pulse. As a result, to the left of this line the pulse is larger than the fibre transmitting it.

Since we have shown that the length of the fibre does not alter the transfer efficiency of our system it is still worth noting that repeaters of shorter lengths are more desirable as a real system will have some degree of attenuation loss. The simulations created have the option to consider fibre attenuation losses. However including these types of losses only shows a decrease in transfer efficiency equivalent to what was lost in the fibre. This straightforward result is shown in appendix E and will not be discussed further here.

4.4.3 Imperfections

This subsection looks at taking the cavity with the optimal parameters and seeing how it behaves when various imperfections, such as misalignment, delay in turning on the second laser and fabrication tolerances in the cavity mirrors, are introduced. For our system we used the new cavity losses, caused by imperfections, to calculate the laser pulse for our single photon wavefunction. This will show the optimal results of these imperfect systems.

4.4.3.1 Misaligned Cavities

Using the geometry derived in Chapter 3.2 with the full simulation we are able to see how misalignment affects the overall performance of the system.

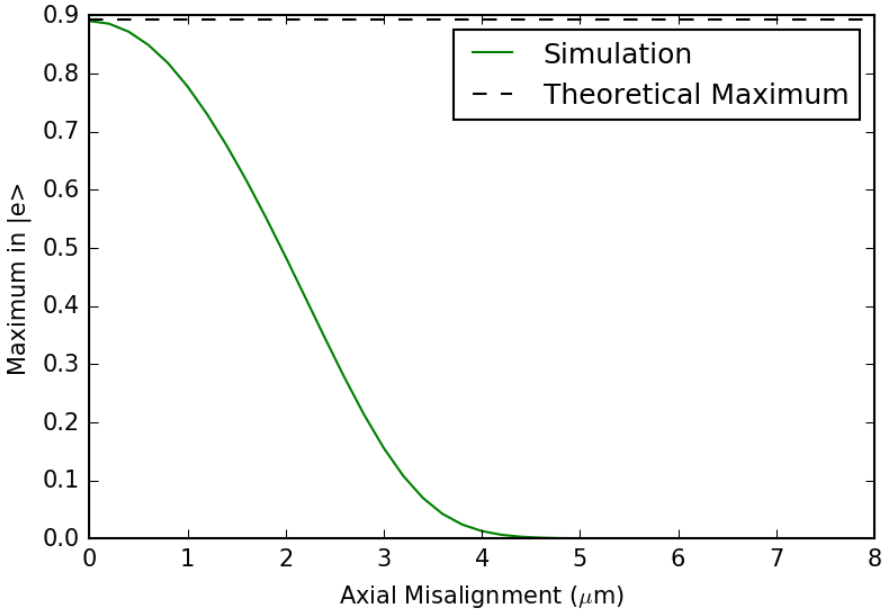

Figure 4.18: Transfer efficiency vs axial misalignment. The cooperativity and coupling efficiency of this can be seen in Figure D.4

Figure 4.18 shows that the overall ion-ion transfer efficiency falls by 50% to 0.445 when the cavity is axially misaligned by $M_{ax} = 2.11\mu$m. This is caused by a decrease in both the cooperativity and the cavity↔fibre coupling efficiency as seen in Figure D.4. For these cavity parameters this level of tolerance to misalignment is perfectly acceptable as various products on the market allow for nm level precision when aligning fibres [91], which is achievable in experiments [44]. For integration inside an ion-trap quantum computer, the use of advanced alignment tables may not be suitable as they would need to operate within a vacuum chamber, could cause disruption to the trapping potential, and they would be very expensive to scale. In practice this means a less accurate alignment methods may be used. One such method would be to fabricate a micro

structure to keep the fibre aligned. Post experiments with these structures have achieved a maximum lateral alignment accuracy of 150nm[92].

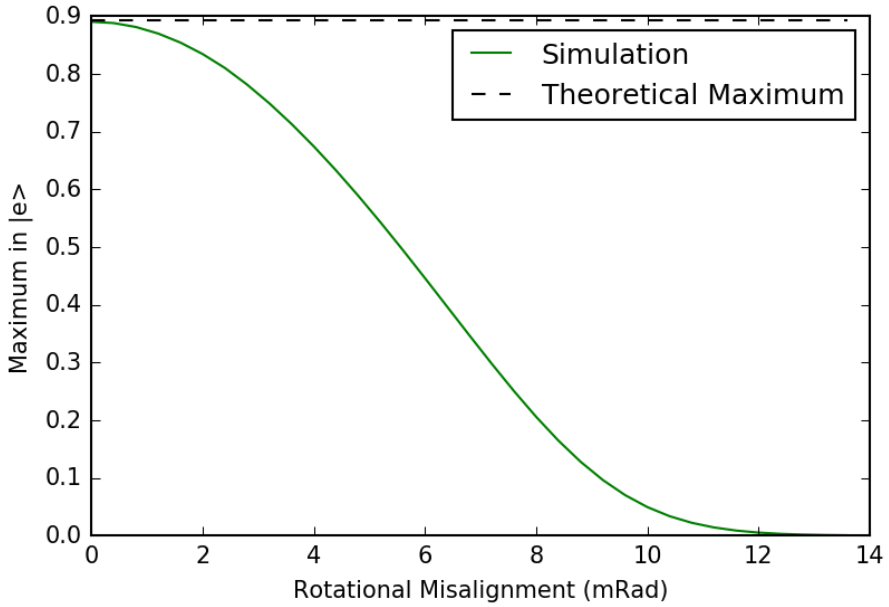

Figure 4.19: Transfer efficiency vs rotational misalignment. The cooperativity and coupling efficiency of this can be seen in Figure D.5

Figure 4.19 shows that the overall ion-ion transfer efficiency falls by 50% to 0.445 when the cavity is rotationally misaligned by $\theta = 6.18$mrad (0.354°). This is caused by a decrease in both the cooperativity and the cavity↔fibre coupling efficiency as seen in Figure D.5. Since alignment tables exist that allow for 2μrad precision[93], a tolerance in the mrad regime is 3 orders of magnitude larger than the achievable precision. However, when using micro structures to align the fibres the angular alignment accuracy of 6.3mrad[92] would cause significant loss.

Whilst the tolerances to misalignment in this subsection are very reasonable when using an alignment table, it is worth bearing in mind that as the mirror size increases and cavity length decreases, the optimal system will operate at increased concentricity to improve coupling with the ion. This will affect the tolerance to errors in misalignment more dramatically than our current system. However, when using micro structures to align the cavities special attention should be taken to increase the accuracy of the angular alignment because the method used in some experiments [92] would result in above 50% losses of ion-ion transfer efficiency.

4.4.3.2 Fabrication Tolerance

When designing a device such as these fibre tip cavities it is important to know how tolerant the mirrors are to fabrication errors in the reflectivity and radius of curvature. Since the cavity length, L, is fixed at 1.4mm we will be looking at radius of curvature in terms of the concentricity parameter, δ. Figure 4.20 shows that as the error in concentricity changes from $\delta = 0.0418$, the maximum transfer decreases from 0.89. At $\delta = 0.0218$ the transfer efficiency falls to 0.787, and at $\delta = 0.0618$ the transfer efficiency falls to 0.883. Since the mirror curvature can be made to a higher precision than ± 0.02 ($\pm 28\mu$m for a cavity length of 1.4mm)[94], for a fibre tip mirror created by CO_2 laser ablation, the tolerance in mirror curvature should not be an issue. We can also see from Figure 4.21 that at a concentricity of $\delta = 0.0224$ the cooperativity peaks and then starts to decrease; this is due to the trade off between clipping losses and scattering and absorption losses.

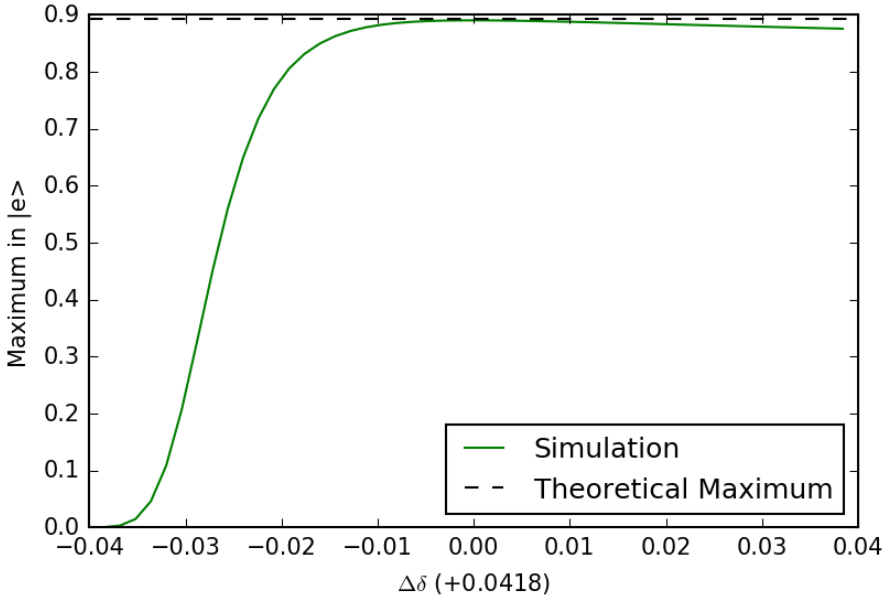

Figure 4.20: Transfer efficiency vs concentricity. Figure 4.21 shows how the cooperativity and cavity↔fibre coupling efficiency are affected by this error.

Figure 4.22 shows how the reflectivity of the cavity affects its overall performance. If we increase the reflectivity from the optimal value of 99.954% we see a rapid drop in maximum transfer. This is due to the light being trapped in the cavity for longer resulting in the cavity losses playing an increasingly bigger role. Increasing the mirror reflectivity by +0.02%, to 99.974%, we see a drop in transfer of around 0.02, to 0.87. However, if we decrease the mirror reflectivity we also notice a drop in maximum transfer because the photon has less time in the cavity and is less likely to interact with the atom. A drop in reflectivity of −0.02%, to 99.934%, results in a drop in transfer of about 0.01, to 0.88. This shows that whilst it is important to fabricate a reflectivity that yields a good balance between interactions with the atom and coupling into the fibre, the tolerance

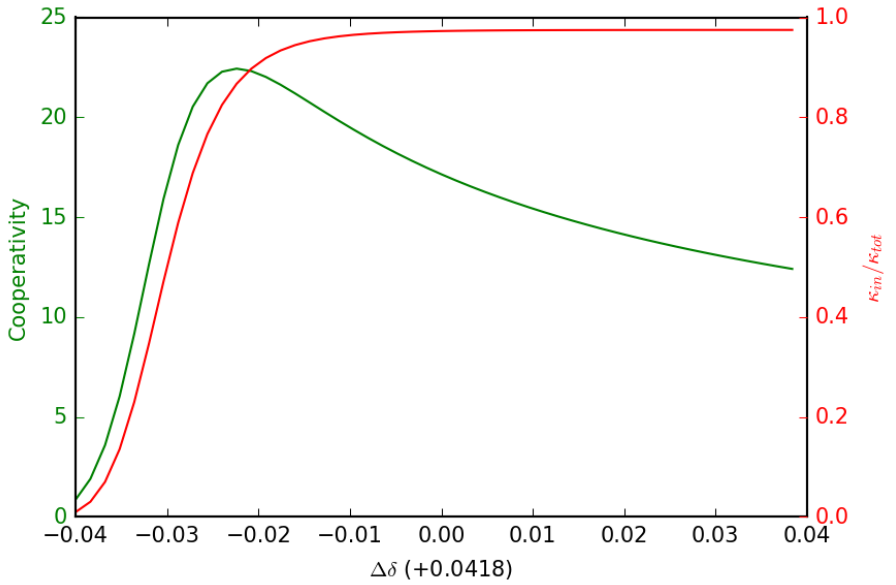

Figure 4.21: Cooperativity and cavity-fibre coupling efficiency vs concentricity for the results shown in Figure 4.20.

on the reflectivity is perfectly reasonable as mirrors with a reflectivity of 99.993% have been demonstrated with an error of ±0.001%[94], and mirrors with significantly higher reflectivity have been achievable for decades[95].

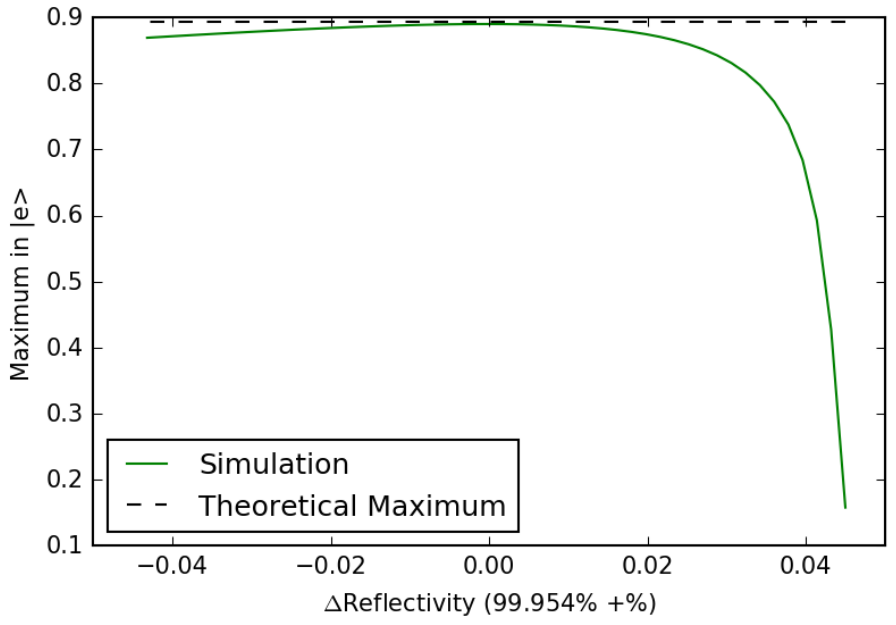

Figure 4.22: Transfer efficiency vs reflectivity. As we simulate a cavity with an error in the reflectivity we see that the performance of the system decreases. The results of the full simulation here match very well with what we see in Figure 3.25.

Whilst the parameters in this subsection are very reasonable for our use case, it is worth

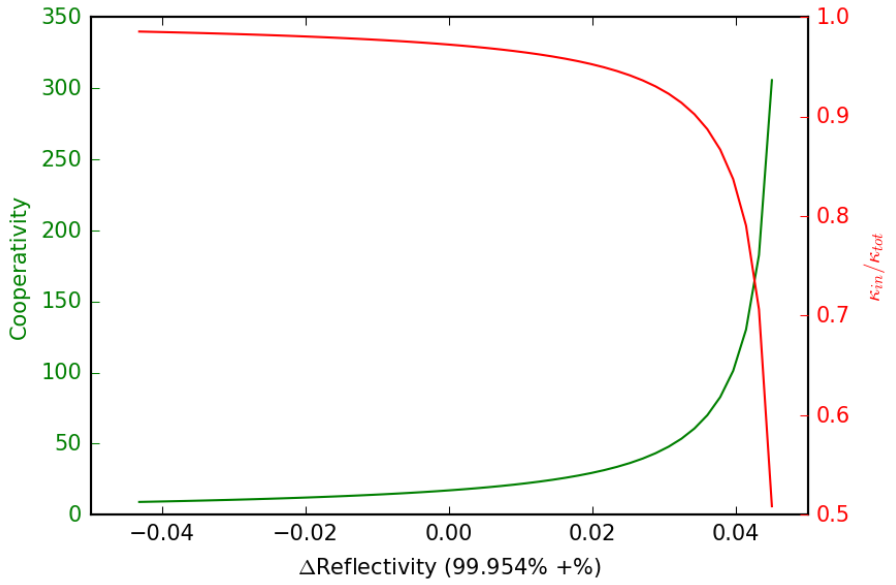

Figure 4.23: Cooperativity and cavity-fibre coupling efficiency vs reflectivity for the results shown in Figure 4.22

bearing in mind that as the mirror size increases and cavity length decreases, the clipping loss of the cavity will be reduced which will allow for increased concentricity. This will affect the tolerance to errors in δ more dramatically than our current system.

4.4.3.3 Laser Pulse Delay

Another important aspect of this set up is to be able to time the laser pulse of the second cavity so that it lines up with the expected arrival time of the photon. In the simulation this is done by calculating the arrival delay with eq. (4.11), and assuming the laser is activated at exactly the right time. The single photon wavefunctions used had a Guassian profile with three different FWHM values. Figure 4.24 shows that, as expected, a delay in activating the laser pulse on the second cavity results in an overall lower transfer efficiency.

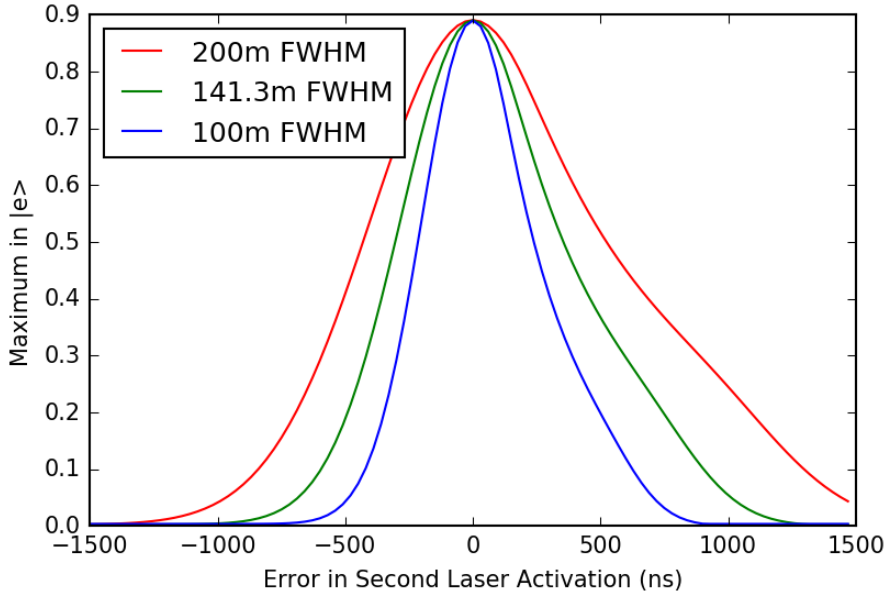

Figure 4.24: Transfer efficiency vs error in second laser activation. All three single photon pulses used a Guassian profile.

Figure 4.24 shows that in our system the pulse with a FWHM of 141.3m requires a delay of 400ns for a fall in efficiency of 50%, to 0.445, whereas the pulses with a FWHM of 100m and 200m are tolerant to a delay of 263ns and 588ns, respectively, for the same fall in transfer efficiency. This shows that the larger the target pulse the more tolerant the system is to error in laser activation time.

4.5 Chapter Summary

This chapter looked at using an optical fibre to connect the cavities that were analysed in the previous chapter. Section 4.1.1 built the initial dynamics of two cavities connected by a fibre, with the first cavity initially containing a single photon. This section showed that, under the given parameters, the photon would enter the second cavity with 54% probability. Section 4.1.2 shows that near deterministic transfer is theoretically possible by time reversing the emitted pulse. This is consistent with the results expected from literature[76].

Section 4.2 took the shaping of the pulse even further and looked at how the probability of the photon entering the cavity is dependent on the shape of the incoming photon wavefunction. By testing different shapes we were able to compare our results with expected results from literature to verify that the model was correct[79].

Section 4.3 added laser driven ions into the cavities and considered the losses associated with the system. This section was the final step in creating an accurate simulation of our real world system. Using this system we could test the expected loss of ion-cavity-fibre transfer with literature [71] allowing further confidence in our results.

Section 4.4 finally put together all of the components from Chapter 3 and Chapter 4 to calculate the optimal cavity parameters under the constraints imposed by the fibre trap. This section looked at how the system is affected by mirror size, cavity length, wavelength, scattering and absorption losses, and fibre length. Moreover, how the performance of the optimised system is analysed with respect to misalignments, fabrication errors, and timing delays of the pulse.

The next chapter will look at the conclusions we can draw from the results of this thesis.

Chapter 5

Conclusion

The motivation of this project was to analyse how the addition of cavities and an optical fibre could improve the performance of ion to ion transfer for the ion trap based quantum computer proposed at NQIT [23]. For this analysis we took the simplest network of a ion-cavity-fibre-cavity-ion, as seen in Figure 1.2, which would represent two nodes of our quantum computer. Using restrictions on cavity length and mirror size, found from previous research on integrating fibre tip cavities into ion traps [36][37], we were able to simulate an optimised network of cavities for maximum ion-cavity-fibre-cavity-ion transfer. In future work this optimised system could be used to generate entanglement between the two ions without needing to use single photon detectors. Ideally, for this system we would be able to find a solution that would allow the transfer of this system to be near deterministic (above an overall efficiency of 99% for a two qubit gate [12]) because without the 'double click' event of the detectors we would be unable to tell if the entanglement was unsuccessful.

This thesis has introduced useful insight into the behaviour of cavity system, with Chapter 3 analysing relationships between alignment and cavity performance for use in any FP cavity regime. Chapter 4 produced an analysis of ion-ion population transfer using cavities and an optical fibre under constraints where they are integrated with an ion trap, and produced insights to find the optimal cavity parameters for this use case.

Chapter 3 found that misalignment may play a bigger role in losses of a cavity system than previously expected[15]. In the case of highly concentric mirrors, the system is extremely sensitive to misalignment. However, for the fibre tip cavities, due to a combination of small mirror sizes and long cavity lengths, we operate in a much more stable regime than systems such as neutral atom experiments. As a result of this the NQIT system is tolerant to axial misalignments in the order of μm and rotational misalignments in the order of mrad. This is further shown by results from Section 4.4.3.1, which given current alignment systems is perfectly achievable for high-end alignment tables, but may require extra care when aligned using fabricated micro-structures.

Section 3.4 proposed an asymmetric cavity where the mirrors had different size and concentricities that is expected to achieve similar transfer efficiencies as the NQIT system, however this system shows improved tolerance against misalignment. Whilst increased tolerance to misalignment may not be necessary under current design restrictions, further improvement of the ion trap geometry may allow shorter cavity lengths and larger mirrors. This would result in a desire for more misalignment tolerant designs.

Chapter 4 found a balance between the concentricity of the cavity and the reflectivity of the mirrors for the optimal ion-cavity-fibre-cavity-ion transfer. However, this balance is dependent on the exact constraints of the system, i.e. cavity length, wavelength, mirror size, and scattering and absorption losses. Under the current design restrictions the tolerance to errors of the system, such as misalignment or fabrication uncertainty, is reasonable. However, an overall ion-ion transfer efficiency of 89% is well below the near deterministic value we would need to achieve direct ion to ion entanglement and remove the detector layer of the NQIT system for scalable quantum computing. As a result improvements must be made to allow for a shorter cavity length or larger cavity mirrors to increase this efficiency. If this is not possible then the results in Section 4.4.2.1 and Section 4.4.2.2 indicate that a longer cavity with larger mirrors in a more concentric regime would be worth looking into for future NQIT designs. In both these cases the cavities would be more concentric which would reduce the tolerance to misalignment as expected from Figure 3.8.

5.1 Future Work

So far this work has looked at the case of transferring the population of one ion in a cavity to another connected by an optical fibre, using the STIRAP technique to shape the pulse. This work has many ways it may be expanded further.

5.1.1 Shaping via Cascaded Cavities

One potential avenue for future research would be to remove the lasers driving the ions by using cascaded cavities to shape the single photon pulse. A diagram of such a system can be seen in Figure 5.1

Figure 5.1: Cascaded cavities.

By considering left and right propagating modes separately [96], we can model the system with the Hamiltonian (dropping $\hbar$),

$$\hat{H} = \Delta_a \hat{a}^\dagger \hat{a} + \Delta_b \hat{b}^\dagger \hat{b} + \sum_i^N \Delta_A \hat{A}_i^\dagger \hat{A}_i + \sum_i^N \Delta_B \hat{B}_i^\dagger \hat{B}_i + \sum_k \Delta_k \hat{c_k}^\dagger \hat{c_k} + H_{int}, \tag{5.1}$$

where $\hat{A}$ and $\hat{B}$ represent the annihilator operators for N cavities on the left and right side respectively, $\hat{a}$ and $\hat{b}$ are the final end cavities, and $\hat{c_k}$ represents the optical fibre connecting both cavity systems. The interaction term $\hat{H}_{int}$ is given by

$$\begin{aligned} \hat{H}_{int} = {} & J_a(\hat{a}\hat{A}_0^\dagger + \hat{A}_0\hat{a}^\dagger) + J_b(\hat{b}\hat{B}_0^\dagger + \hat{B}_0\hat{b}^\dagger) + J_A \sum_i^{N-1} (\hat{A}_i\hat{A}_{i+1}^\dagger + \hat{A}_{i+1}\hat{A}_i^\dagger) \\ & + J_B \sum_i^{N-1} (\hat{B}_i\hat{B}_{i+1}^\dagger + \hat{B}_{i+1}\hat{B}_i^\dagger) + \eta_A \sum_k (\hat{A}_N\hat{c_k}^\dagger + \hat{c_k}\hat{A}_N^\dagger) \\ & + \eta_B \sum_k (\hat{B}_N\hat{c_k}^\dagger + \hat{c_k}\hat{B}_N^\dagger)(-1)^k \end{aligned} , \tag{5.2}$$

where $J_{a,b}$ is the coupling strength between the main cavities and the first cavity of the cascade. $J_{A,B}$ is the coupling strength between each of the neighbouring cavity layers on the left and right side of the fibre respectively, and $\eta_{A,B}$ is the coupling of the fibre modes to the $\hat{A}_N$ and $\hat{B}_N$ cavities either side of it where N number of cavities. A quick simulation using the parameters seen in Table 5.1 allows us to see how such a system may act with no atoms and a single photon in the first cavity.

L	N	$\eta_{A,B}$	$J_{A,B}$	$J_{a,b}$	$\Delta_{A,B}$
$3000m$	8	2.24×10^6	$10\eta_{A,B}$	$\eta_{A,B}$	$\sqrt{2J_{A,B}}$

Table 5.1: Parameters used in the many cavity model.

The values chosen in Table 5.1 were done as a proof of concept and may not be representative of a real world device. The system under these parameters produces the results shown in Figure 5.2(a) and Figure 5.2(b).

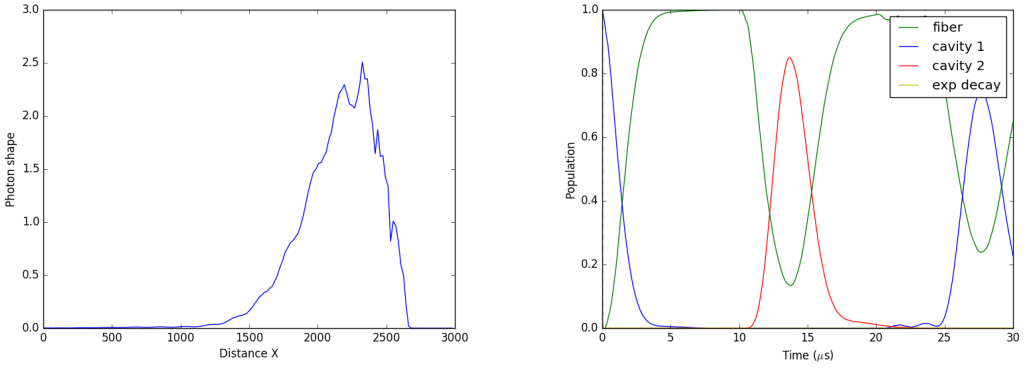

Figure 5.2: Cavity-cascaded cavity-fibre-cascaded cavity-cavity system. Figure (a) shows the pulse at time 9μs as a result of this many cavity system. Figure (b) shows the absorption as a result of many cavity system, the pulse reaches the second cavity at 10μs and is absorbed with a >80% chance.

In Figure 5.2(b) the pulse decays from cavity 1, then propagates in the fibre until 10μs and is then absorbed with a >80% chance into cavity 2. This model may be expanded upon with better cavity parameters to enable passive single photon shaping. By aiming for a time symmetric shape it may be possible to drive absorption without the need for a laser. However, further issues that would need to be considered are increased scattering and absorption losses due to the extra surface boundaries and extra fabrication errors due to the cavities all needing to be the correct length. Assuming it is possible to create a shape time symmetric enough to obtain (near) full absorption theoretically, one then needs to investigate how much variation in the receiving cavity array can be tolerated. This cavity system can be the result of a Bragg grating written at the ends of the fibre, which may help with some of these tolerances.

5.1.2 Creating Entanglement

In our system we focus on transferring the state $|e_1, g_2\rangle \rightarrow |g_1, e_2\rangle$. However, for quantum computing we require the ability to generate an entangled state i.e. $\frac{1}{\sqrt{2}}[|e_1, g_2\rangle + |g_1, e_2\rangle]$.

Using, our current simulation we can achieve this by calculating a STIRAP pulse that would have a 50% chance of actually generating a photon. This can easily be done with the code already created. However, as can be seen from Figure 5.3 using the time reverse of the laser pulse used to generate the 50% photon emission does not allow for complete absorption of the 50% photon pulse (Figure 5.3(a)), instead the time reverse of the laser pulse that would be used to generate the full photon emission is needed (Figure 5.3(b)).

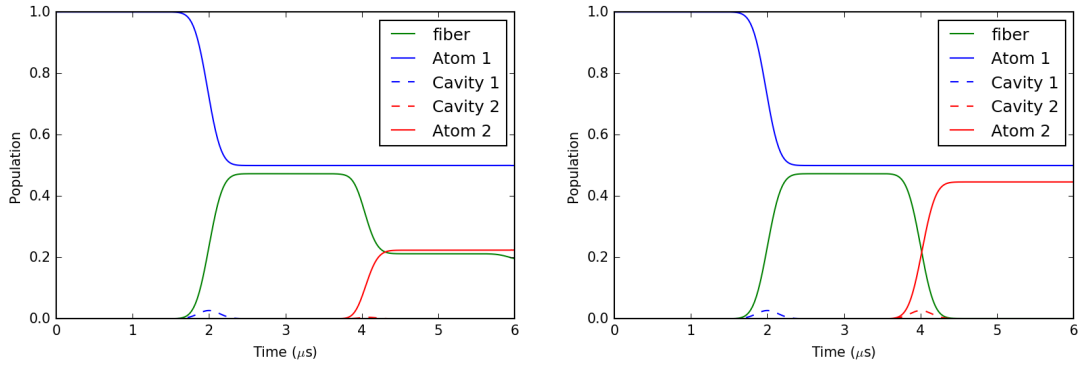

Figure 5.3: (a) shows the population transfer when the laser pulse is set to generate a photon with a 50% chance and the second cavity uses the time reverse laser pulse to absorb the incoming photon. (b) shows the population transfer when the laser pulse is set to generate a photon with a 50% chance and the second cavity uses a laser pulse that is the time reverse of one with a 100% chance of emitting a photon.

Figure 5.3(b) also shows that whilst 50% of the excitation is still in the first ion, the second ion has received only 44.6%, which is due to the losses analysed in this thesis.

A full analysis of this entanglement generation, including creating other states, would be a useful continuation of this work.

5.1.3 Networking Multiple Ions

Another way this work can be expanded is by adding multiple cavities to simulate a network of ions. Whilst a two ion-cavity system is good for studying the individual components, further insight may be had by creating a more complex network.

In this system it may be worth using a symmetric laser pulse to shape the emitted photon, which will allow the same laser pulse to be used for both receiving and emitting ions. Once this is done we could set all fibre lengths in the system as a multiple of the shortest length, which would allow us to create a system where all of the ions can be driven periodically. This system would therefore operate at a set clock speed.

5.1.4 Comparing Different Ions

In this work we have focused on using Ca^+ ions, however other experiments have used different ions such as Yb^+ and neutral atoms such as Rb [45]. An in depth analysis of the performance how different systems act under the optimisation in this thesis may provide a useful insight into which ions are the best under different circumstances.

Appendix A

Numerical Methods

The final simulation, which obtained many of the results in chapter 4 of the thesis, has four distinct steps, with each step requiring their own numerical methods. The code was written in the programming language Python using the packages NumPy, SciPy, Math, and plotted using Matplotlib.

The first step is to take in the fixed cavity parameters (i.e. mirror size, cavity length, wavelength etc) and guess the near optimal concentricity and reflectivity values. The second step uses a numerical method known as the Nelder-Mead method [97], a type of gradient descent algorithm, to find the optimal parameters. The code then checks if the optimised result is physically possible: if not then it will change the initial guess values and try to optimise again, if it is possible then it moves on to the next step.

The next step uses the misalignment geometry derived in this thesis, and known Gaussian beam physics to calculate the electric field of the cavity mode on the mirror surface. Using Simpsons rule[97] for integration we are able to find the losses and coupling efficiencies of the cavity.

The third step is to calculate the laser pulse required to generate the desired cavity→fibre decay, which results in any arbitrary single photon pulse shape. This step uses the cavity parameters calculated in step two, with equations found in literature[71], and the trapezoidal rule[97] for cumulative integration.

The final step is the full network simulation. This simulation starts with the ion in the first cavity in the excited state and uses the laser pulse calculated in step three to generate the desired single photon pulse in the fibre. This step also uses the delay of the pulse arriving at the second cavity and the time symmetry of the problem to drive maximum absorption into the second cavity. Finally this method takes the highest value of the excited state in the second ion as the maximum chance of transfer. This step uses the Runge-Kutta method[97], with the complex values mapped as real values, for solving the differential equations.

All of these steps are then looped to find how changing the system affects its performance.

Appendix B

Pulse Shapes

This appendix shows the single-photon pulse shapes used in Section 4.2.

Pulses shown in this appendix were first calculated, then converted to the equivalent frequency space shape. The pulses were then normalised to correspond to a single photon. For the pulses used in these simulations the distance x is given in meters and the height of the shape is arbitrary.

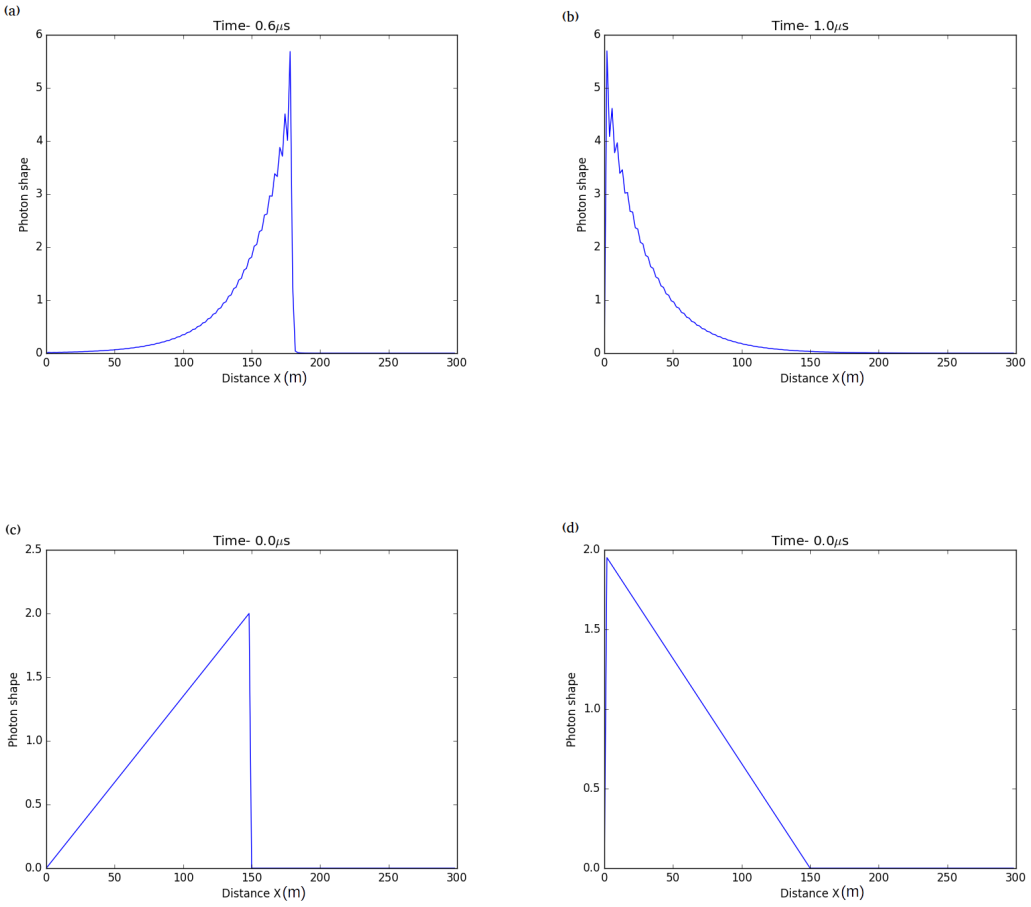

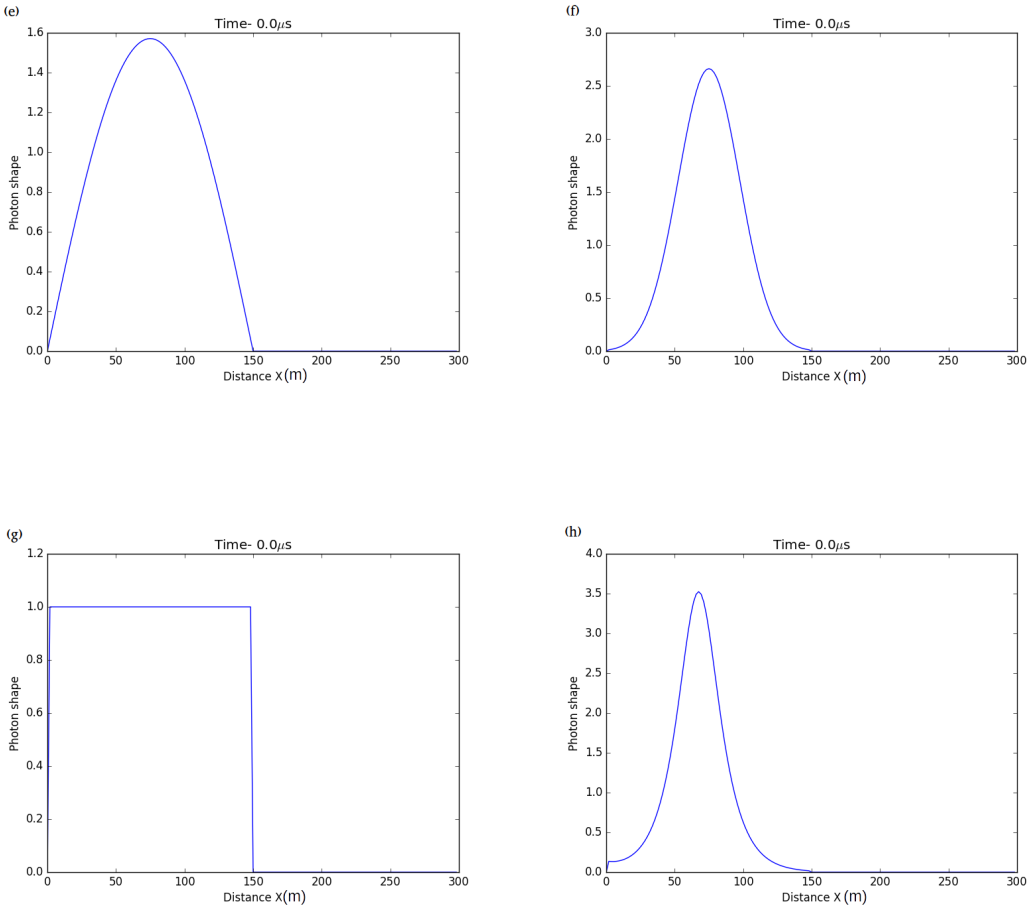

Figure B.1: Pulse shapes (a)-(h) as defined in Table 4.1

The pulse shown in Figure B.1(a) shows the result of a pulse from the cavity if it is allowed to decay naturally.

Appendix C

Optimal Transmission

Figure C.1 shows the maximum ion-cavity-fibre-cavity-ion transfer of our system as a function of mirror transmission with the concentricity being optimised for each point. This is in addition to Figure 4.9 in Section 4.4.2 which shows the transfer rate versus concentricity.

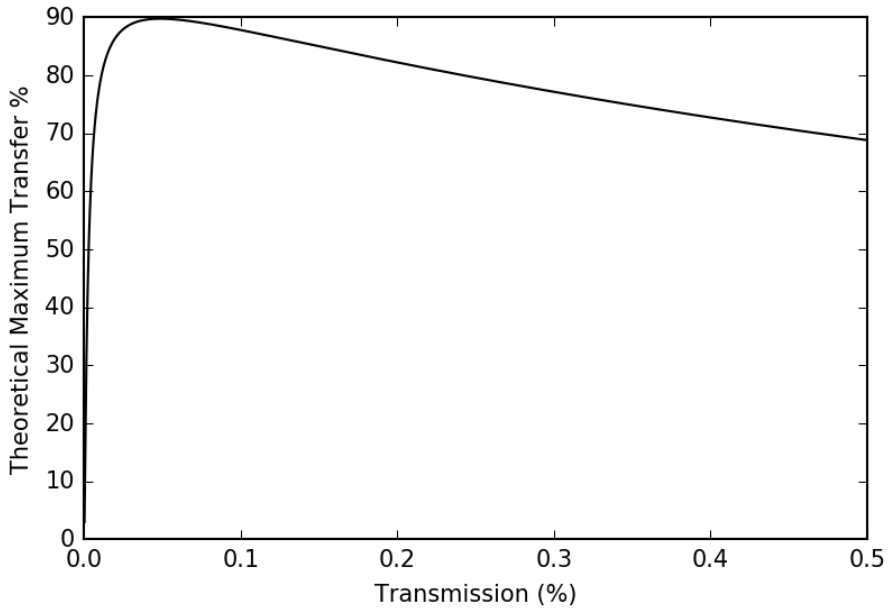

Figure C.1: The maximum chance of success, O, for the cavity shown in Figure 2.4 with the transmissivity of the mirror. Note that the cavity concentricity at each point on this graph is varied to give the optimal O value as seen in Figure 4.9.

Appendix D

Supplementary Figures for Section 4.4

Figure D.1, Figure D.2, and Figure D.3 below show the parameters of the 90μm, 70μm, and 50μm mirrors for Figure 4.12. Figure D.3 shows that as the clipping losses increase that the optimal cavity compensates by having a lower reflectivity, this reduces the amount of time the photon spends in the cavity and reduces the chance of it being lost.

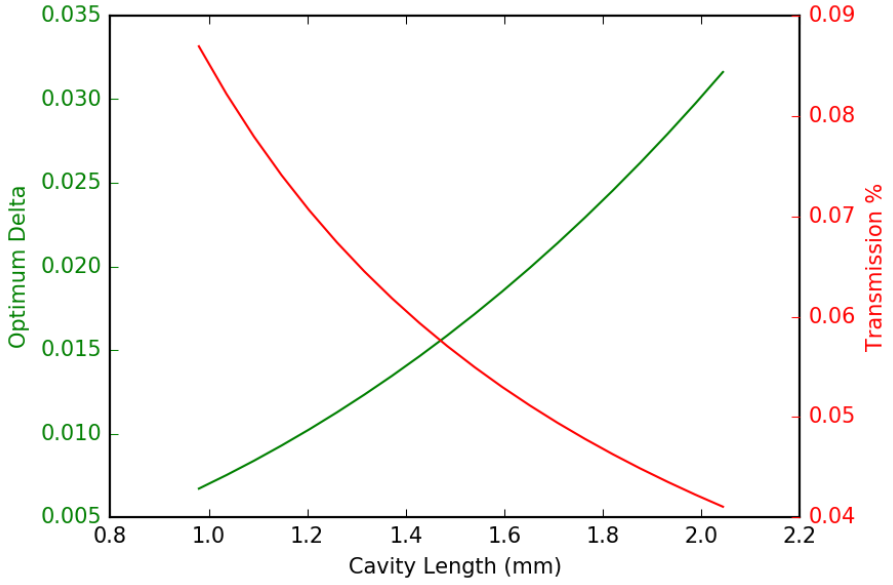

Figure D.1: Optimal concentricity and transmission vs cavity length for the 90μm mirror in Figure 4.12.

Figure D.4 and Figure D.5 show how the cooperativity and coupling efficiency are affected by both axial and rotational misalignment in Figure 4.18 and Figure 4.19, respectively.

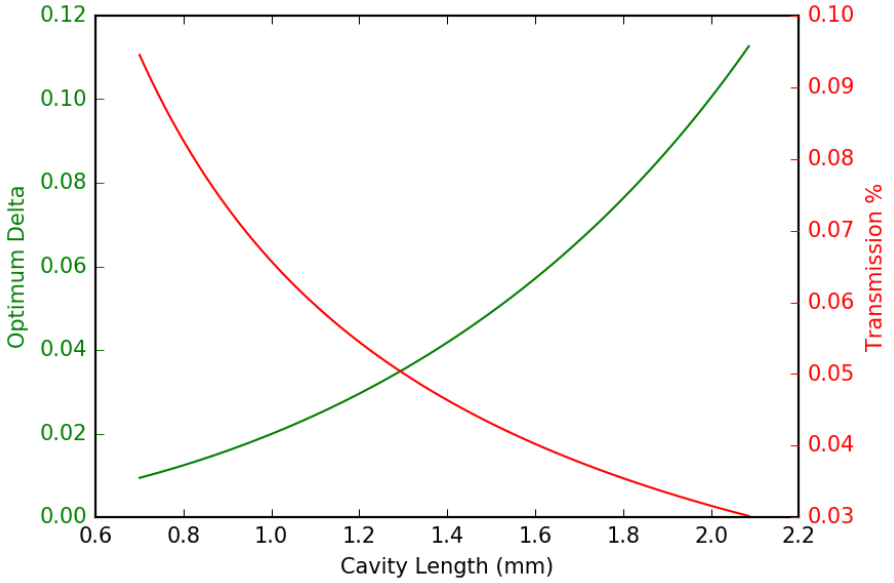

Figure D.2: Optimal concentricity and transmission vs cavity length for the 70μm mirror in Figure 4.12.

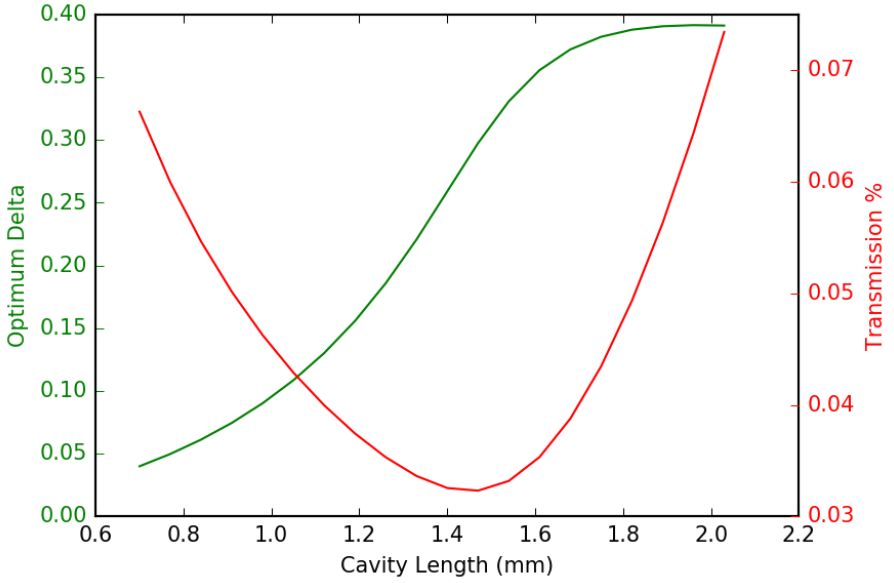

Figure D.3: Optimal concentricity and transmission vs cavity length for the 50μm mirror in Figure 4.12.

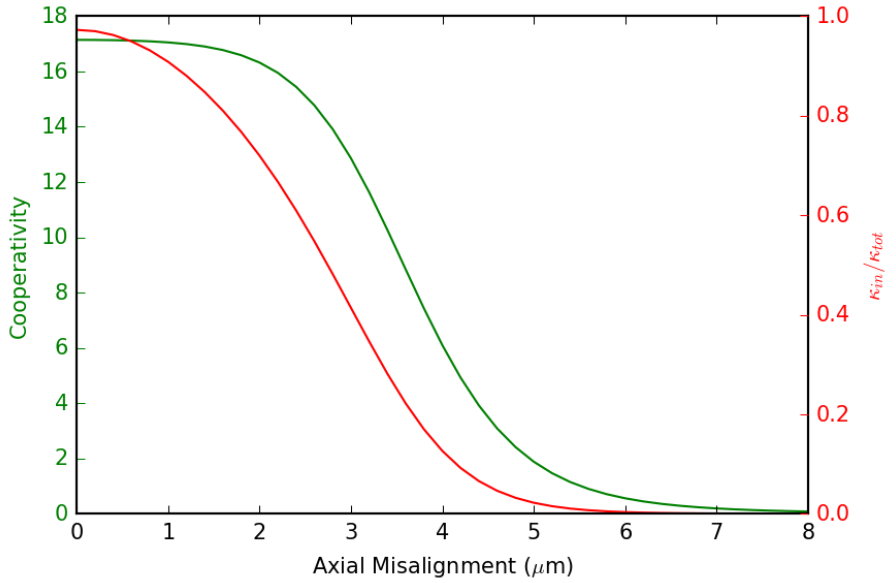

Figure D.4: Cooperativity and coupling efficiency of the optimal cavity vs axial misalignment as seen in Figure 4.18

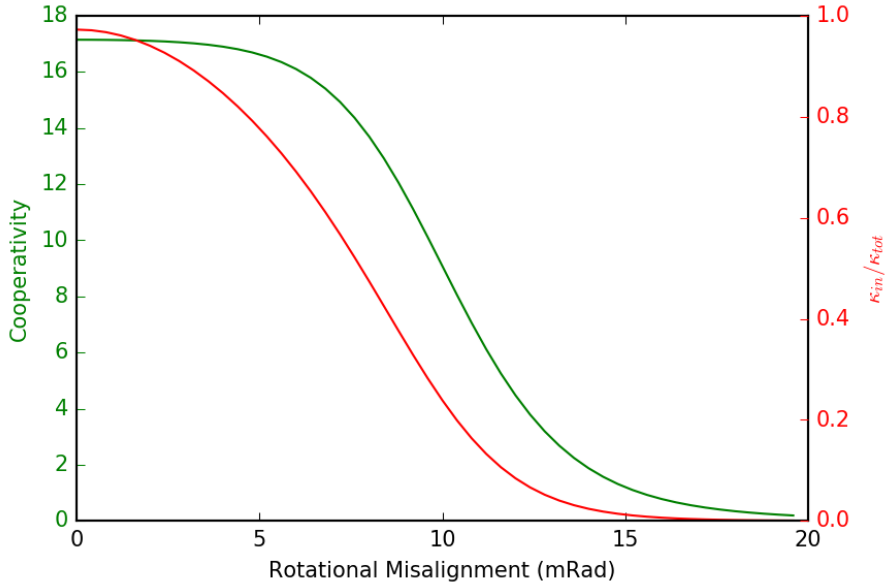

Figure D.5: Cooperativity and coupling efficiency of the optimal cavity vs rotational misalignment as seen in Figure 4.19

Appendix E

Fibre Losses

In Section 4.4.2.5 the effects of fibre losses were briefly looked at. However, since they do not affect the performance of the cavity and only act as a simple additional loss the results have not been included in the main thesis. Figure E.1 shows how loss within the fibre affects the overall ion-ion transfer efficiency.

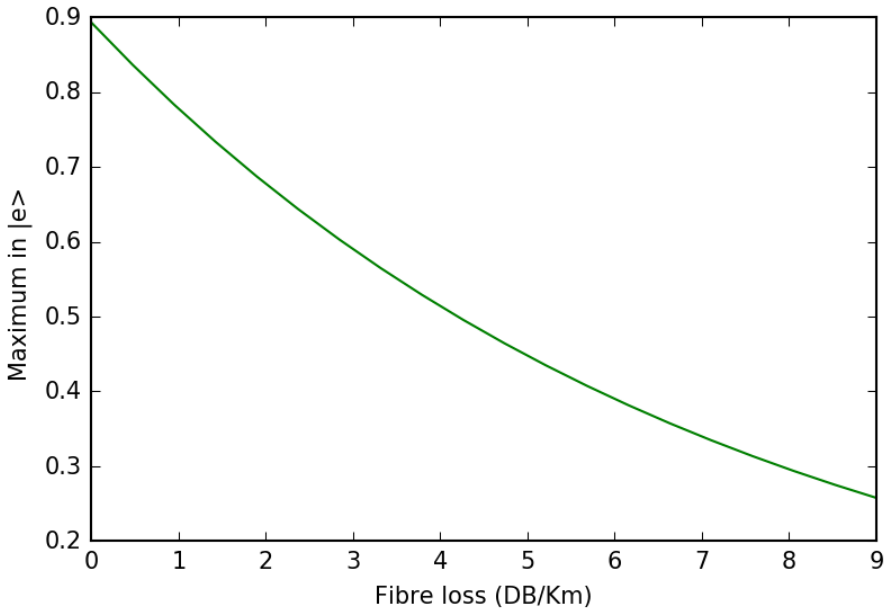

Figure E.1: Maximum transfer efficiency with a 600m fibre versus fibre loss.

Publications

1. D. T. Clarke and P. Horak, "Alignment requirements of Fabry-Perot microresonators for ion trap quantum information processing (Conference Presentation)", Proc. SPIE 10674, Quantum Technologies 2018, 106740P (29 May 2018); doi: 10.1117/12.2307152; https://doi.org/10.1117/12.2307152

2. C. J. Stirling, A. L. Donko, N. Baktash, K. Grabska, A. L. Camacho Rosales, D. T. Clarke, J. J. Prentice, M. T. Posner, "Student-led outreach and public engagement activities at the University of Southampton to celebrate the inaugural International Day of Light", Proc. SPIE 10741, Optics Education and Outreach V, 107410B (14 September 2018); doi: 10.1117/12.2320304; https://doi.org/10.1117/12.2320304

References

[1] A. Einstein. The Nobel Prize in Physics 1921. *Nobel Media AB 2018*, 1921.

[2] J. P. Dowling and G. J. Milburn. Quantum Technology: The Second Quantum Revolution. *Philos. Trans. Royal Soc. A*, 361, 1655, 2003.

[3] R. P. Feynman. Simulating physics with computers. *Int. J. Theor. Phys.*, 21(6-7):467–488, 1982.

[4] S. Boixo, S. V. Isakov, V. N. Smelyanskiy, R. Babbush, N. Ding, Z. Jiang, M. J. Bremner, J. M. Martinis, and H. Neven. Characterizing Quantum Supremacy in Near-Term Devices. *Nat. Phys.* 14, 595-600, 2018.

[5] T. Häner and D. S. Steiger. 0.5 Petabyte Simulation of a 45-Qubit Quantum Circuit. *Proceedings of the International Conference for High Performance Computing, Networking, Storage and Analysis,* SC'17, pages 33:1-33:10, 2017.

[6] S. Aaronson and A. Arkhipov. The Computational Complexity of Linear Optics. *Theory of Computing* 9(4):143–252, 2010.

[7] T. Graß, D. Raventós, B. Juliá-Díaz, C. Gogolin, and M. Lewenstein. Quantum annealing for the number-partitioning problem using a tunable spin glass of ions. *Nat. Commun*, 7(May):11524, 2016.

[8] J. M. Gambetta, J. M. Chow, and M. Steffen. Building logical qubits in a superconducting quantum computing system. *npj Quantum Information*, **3**, 2, 2017.

[9] K. Nemoto, M. Trupke, S. J. Devitt, B. Scharfenberger, K. Buczak, J. Schmiedmayer, and W. J. Munro. Photonic Quantum Networks formed from NV centers. *Sci. Rep*, **6**, 26284, 2016.

[10] B. Lekitsch, S. Weidt, A. G. Fowler, K. Mølmer, S. J. Devitt, C. Wunderlich, and W. K. Hensinger. Blueprint for a microwave trapped ion quantum computer. *Science Adv.* **3**, 2 2017.

[11] E. Knill, R. Laflamme, and W. H. Zurek, Resilient Quantum Computation. *Science*, 279, 5349, 1998.

[12] A. G. Fowler, M. Mariantoni, J. M. Martinis, and A. N. Clelan, Surface codes: Towards practical large-scale quantum computation. *Phys. Rev. A*, 86, 4, 2012.

[13] G. Waldherr, Y. Wang, S. Zaiser, M. Jamali, T. Schulte-Herbruggen, H. Abe, T. Ohshima, J. Isoya, J. F. Du, P. Neumann, and J. Wrachtrup, Quantum error correction in a solid-state hybrid spin register.. *Nature*, 506, 7487, 2014.

[14] R. Barends, J. Kelly, A. Megrant, A. Veitia, D. Sank, E. Jeffrey, T. C. White, J. Mutus, A. G. Fowler, B. Campbell, Y. Chen, Z. Chen, B. Chiaro, A. Dunsworth, C. Neill, P. OMalley, P. Roushan, A. Vainsencher, J. Wenner, N. Korotkov, N. Cleland, and J. M. Martinis, Superconducting quantum circuits at the surface code threshold for fault tolerance. *Nature*, 508, 7497, 2014.

[15] C J Ballance, T P Harty, N M Linke, M A Sepiol, and D M Lucas. High-Fidelity Quantum Logic Gates Using Trapped-Ion Hyperfine Qubits. *Phys. Rev. Lett.* **117**,060504:1–6, 2016.

[16] D Kielpinski. Architecture for a large-scale ion-trap quantum computer. *Nature*, **417**, (June):709–711, 2002.

[17] D Hucul, I V Inlek, G Vittorini, C Crocker, S Debnath, S M Clark, and C Monroe. Modular entanglement of atomic qubits using photons and phonons. *Nature*, **11**, 37-42, 2015.

[18] J. I. Cirac and P. Zoller. *Phys. Rev. Lett.* **74**(20):4091–4094, 1995.

[19] A. Fruchtman and I. Choi. Technological Roadmap for Fault-Tolerant Quantum Computing. *Networked Quantum Information Technologies hub*, Oxford University, 2016.

[20] J. Hsu. CES 2018: Intel's 49-Qubit Chip Shoots for Quantum Supremacy. *https://spectrum.ieee.org/tech-talk/computing/hardware/intels-49qubit-chip-aims-for-quantum-supremacy*, 2018. [accessed 19/01/2018]

[21] S. K. Moore. IBM Edges Closer to Quantum Supremacy with 50-Qubit Processor. *https://spectrum.ieee.org/tech-talk/computing/hardware/ibm-edges-closer-to-quantum-supremacy-with-50qubit-processor*, 2018. [accessed 21/11/2018]

[22] J. Kelly. A Preview of Bristlecone, Googles New Quantum Processor. *https://ai.googleblog.com/2018/03/a-preview-of-bristlecone-googles-new.html*, 2018. [accessed 21/11/2018]

[23] A. Gheorghiu, A. Datta, C. Wade, D. Nadlinger, D. OBrien, E. Geurtsen, E. Kassa, F. Sweeney, H. Rowlands, I. Walmsley, I. Choi, J. Joo, J. Smith, J. Becker, N. Walk, N. Beaudrap, P. Leek, P. Wallden, P. Inglesant, R. Deshmukh, R. Srivastava, S.

Benjamin, W. Zhang, W. Hensinger, and X. Yuan, Annual Report 2018. *Networked Quantum Information Technologies hub*, Oxford University, 2018.

[24] D L Moehring, P Maunz, S Olmschenk, K C Younge, D N Matsukevich, L Duan, and C Monroe. Entanglement of single-atom quantum bits at a distance. *Nature*, 449, 68–71, 2007.

[25] B. P. Williams, R. J. Sadlier, and T. S. Humble. Superdense Coding over Optical Fiber Links with Complete Bell-State Measurements, (*Phys. Rev. Lett.*, 118, 050501, 2017.

[26] D Bouwmeester, JW Pan, K Mattle, M Eibl, H Weinfurter, and A Zeilinger. Experimental quantum teleportation. *Nature*, 390(6660):575–579, 1997.

[27] Laser Components, *Application Report: Avalanche Photodiodes*, *https://www.lasercomponents.com/fileadmin/user_upload/home/Datasheets/lc/application-reports/lc-apd/avalanche-photodiodes.pdf*, [Accessed 20th November 2018].

[28] L. You, J. Wu, Y. Xu, X. Hou, W. Fang, H. Li, W. Zhang, L. Zhang, X. Liu, L. Tong, Z. Wang, and X. Xie, Microfiber-coupled superconducting nanowire single-photon detector for near-infrared wavelengths. *Optics Express*, 25, 31221, 2017.

[29] E. Kyoseva, A. Beige, and L. C. Kwek. Coherent cavity networks with complete connectivity. *New J. Phys*, **14**, 023023, 2012.

[30] T. Pellizzari. Quantum Networking with Optical Fibres. *Phys. Rev. Lett*, 79(26):5242–5245, 1997.

[31] A. Serafini, S. Mancini, and S. Bose. Distributed quantum computation via optical fibers. *Phys. Rev. Lett*, 96(1), 010503, 2006.

[32] J. Yin, et al. Satellite-based entanglement distribution over 1200 kilometers. *Science*, 356, 6343, 1140-1144, 2017.

[33] T. Inagaki, N. Matsuda, O. Tadanaga, M. Asobe, and H. Takesue. Entanglement distribution over 300 km of fiber. *Opt. Express*, 21, 23241-23249, 2013.

[34] N. Sangouard, C. Simon, H. Riedmatten, and N. Gisin. Quantum repeaters based on atomic ensembles and linear optics. *Rev. Mod. Phys.*, 83, 33, 2011.

[35] H. J. Kimble. The quantum internet. *Nature*, 453(7198):1023–1030, 2008.

[36] N. Podoliak, H. Takahashi, M. Keller, and P. Horak. Comparative numerical studies of ion traps with integrated optical cavities. *Phys. Rev. Appl.*, 6, 044008, 2016.

[37] N. Podoliak, H. Takahashi, M. Keller, P. Horak. Harnessing the mode mixing in optical fiber-tip cavities. *J. Phys. B: At. Mol. Opt. Phys*, 50, 085503, 2017.

[38] K.J. Vahala. Optical Microcavities. *Nature*, 424, 839, 2003.

[39] W. Bogaerts, P. DeHeyn, T. V. Vaerenbergh, K. DeVos, S. K. Selvaraja, T. Claes, P. Dumon, P. Bienstman, D. VanThourhout, and R. Baets. Silicon microring resonators. *Laser Photonics Rev.*, 6, 1, 47-73, 2012.

[40] I. S. Grudinin, V. S. Ilchenko, and L. Maleki. Ultrahigh optical Q factors of crystalline resonators in the linear regime. *Phys. Rev. A.*, 74, 063806, 2006.

[41] J.W. Silverstone, R. Santagati, D. Bonneau, M.J. Strain, M. Sorel, J.L. OBrien, and M.G. Thompson. Qubit entanglement between ring-resonator photon-pair sources on a silicon chip. *Nat. Commun.*, 6, 7948, 2015.

[42] S. Noda. Photonic Crystal Cavities. *Optical Fiber Communication Conference, OSA Technical Digest .*, 978-1-943580-07-1, 2016.

[43] M. A. Arain and G. Mueller. Design of the Advanced LIGO recycling cacities. *Opt. Express*, 16, 14:10018, 2008.

[44] C. H. Nguyen, A. N. Utama, N. Lewty, K. Durak, G. Maslennikov, S. Straupe, M. Steiner, and C. Kurtsiefer. Single atoms coupled to a near-concentric cavity. *Phys. Rev. A*, 96, 031802, 2017.

[45] B. Brandstätter, A. McClung, K. Schüppert, B. Casabone, K. Friebe, A. Stute, P. O. Schmidt, C. Deutsch, J. Reichel, R. Blatt, and T. E. Northup. Integrated Fiber-Mirror Ion Trap for Strong Ion-Cavity Coupling. *Rev. Sci. Instrum.*, 84, 12, 123104, 2013.

[46] H. J. Pan, P. Ruan, H. W. Wang, and F. Li. Confocal Fabry-Perot Interferometer for Frequency Stabilization of Laser. *Laser Phys.*, 21, 2, 336-339, 2010.

[47] A. Yariv, *Quantum Electronics*, Wiley; 3rd edt. 1989.

[48] T. Fukushima. Approximation accuracy of Gaussian-optical approach applied to two-dimensional optical microcavities. *IEEE*, 19th International Conference on Transparent Optical Networks (ICTON), 10.1109/ICTON.2017.8025076, 2017.

[49] O. Svelto, *Principles of Lasers*, Springer; 5th edt. 2010.

[50] K. Durak, C. H. Nguyen, V. Leong, S. Straupe, and C. Kurtsiefer. Diffraction-limited FabryPerot cavity in the near concentric regime. *New J. Phys.*, 16, 103002, 2014.

[51] H. Takahashi, J. Morphew, F. Orucevic, A. Noguchi, E. Kassa, and M. Keller. Novel laser machining of optical fibers for long cavities with low birefringence. *Opt. Express*, 22, 25, 31317, 2014.

[52] D. Hunger, T. Steinmetz, Y. Colombe, C. Deutsch, T. W. Hänsch, J. Reichel. A fibre Fabry-Perot cavity with high finesse. *New J. Phys.* 12, 065038, 2010.

[53] R P Stanley, R Houdré, U Oesterle, M Gailhanou, and M Ilegems. Ultrahigh finesse microcavity with distributed Bragg reflectors. *Appl. Phys. Lett.*, **65**, 1883, 1994.

[54] E. X. Perez. Design, fabrication and characterization of porous silicon multilayer optical devices, *Universitat Rovira i Virgili*, 978-84-691-0362-3, 2007.

[55] D. Wang, I. T. Ferguson, and J. A. Buck. GaN-based distributed Bragg reflector for high-brightness LED and solid-state lighting. *Appl. Opt*, 46(21):4763, 2007.

[56] S. Kato and T. Aoki. Strong Coupling between a Trapped Single Atom and an All-Fiber Cavity. *Phys. Rev. Lett*, 115, 093603, pages 1–5, 2015.

[57] C Wuttke, M Becker, S Brückner, M Rothhardt, and A Rauschenbeutel. Nanofiber Fabry-Perot microresonator for nonlinear optics and cavity quantum electrodynamics. *Opt. Lett*, 37(11):1949–1951, 2012.

[58] S. Dewra et al. Fabrication and Application of Fiber Bragg Grating - a Review. *Adv. Eng. Tec. Appl.*, 4(2):15–25, 2015.

[59] I. H. Malitson. Interspecimen Comparison of the Refractive Index of Fused Silica. *J. Opt. Soc. Am*, 55(10):1205, 1965.

[60] G. K. Gulati, H. Takahashi, N. Podoliak, P. Horak, M. Keller. Fiber Cavities with Integrated Mode Matching Optics. *Sci. Rep.*, 7:5556, 2017.

[61] Z. Burell. An Introduction to Quantum Computing using Cavity QED concepts. *arXiv:1210.6512v1 [quant-ph]*, 2012.

[62] J. Larson. Dynamics of the JaynesCummings and Rabi models: old wine in new bottles. *Phys. Scr.*, 76, 2, 146, 2007.

[63] G. Lindblad. On the Generators of Quantum Dynamical Semigroups. *Commun. Math. Phys.*, 48, 119–130, 1976.

[64] S. Rosenblum, S. Parkins, and B. Dayan. Photon routing in cavity QED: Beyond the fundamental limit of photon blockade. *Phys. Rev. A.*, 84, 033854, 2011.

[65] Y. L. Zhou, Y. M. Wang, L. M. Liang, and C. Z. Li. Quantum state transfer between distant nodes of a quantum network via adiabatic passage. *Phys. Rev. A*, 79(4), 044304, 2009.

[66] P. Meystre and M. Sargent. *Elements of quantum optics.* ISBN: 3-540-52160-7. page 76. Springer-Verlag Berlin Heidelberg, 1990.

[67] P. Meystre and M. Sargent. *Elements of quantum optics.* ISBN: 3-540-52160-7. pages 79, 354. Springer-Verlag Berlin Heidelberg, 1990.

[68] P. Meystre and M. Sargent. *Elements of quantum optics.* ISBN: 3-540-52160-7. page 123. Springer-Verlag Berlin Heidelberg, 1990.

[69] G S Vasilev, A Kuhn, and N V Vitanov. Optimum pulse shapes for stimulated Raman adiabatic passage. *Phys. Rev. A*, **80**, 013417, 2009.

[70] G. S. Vasilev, D. Ljunggren, and A. Kuhn. Single photons made-to-measure. *New J. Phys*, 12, 063024, 2010.

[71] A. Kuhn. *"Cavity Induced Interfacing of Atoms and Light",* in *Engineering the Atom-Photon Interaction: Controlling Fundamental Processes With Photons, Atoms and Solids.* Berlin, Germany: *Springer*; ISBN 978-3-319-19231-4, 2015.

[72] M. Keller, B. Lange, K. Hayasaka, W. Lange, and H. Walther. Continuous generation of single photons with controlled waveform in an ion-trap cavity system. *Nature*, 431(9):1075–1078, 2004.

[73] M. Keller, B. Lange, K. Hayasaka, W. Lange, and H. Walther. A calcium ion in a cavity as a controlled single-photon source. *New J. Phys*, 6, 95, 2004.

[74] V. Averchenko, D. Sych, and G. Leuchs. Heralded Temporal Shaping of Single Photons Enabled By Entanglement. *Phys. Rev. A*, 96(4), 043822, 2017.

[75] D. Sych, V. Averchenko, and G. Leuchs. Generic method for lossless generation of arbitrarily shaped photons. *Phys. Rev. A*, 96, 053847, 2017.

[76] M. Stobińska, G. Alber, and G. Leuchs. Perfect excitation of a matter qubit by a single photon in free space. *EPL*, 86, 14007, 2009.

[77] S. Stenholm and M. Jakob. Open systems and time reversal. *J. Mod. Opt.* 51:6-7, 841-850, 2004.

[78] G. Leuchs and M. Sondermann. Time reversal symmetry in optics. *Physica Scripta.* 85, 058101, 2012.

[79] Y. Wang, J. Miná, L. Sheridan, and V. Scarani. Efficient excitation of a two-level atom by a single photon in a propagating mode. *Phys. Rev. A*, 83(6), 063842, 2011.

[80] H. P. Specht, J. Bochmann, M. Mücke, B. Weber, E. Figueroa, D. L. Moehring, and G. Rempe. Phase shaping of single-photon wave packets. *Nat. Photon*, 3(July):469–472, 2009.

[81] J. Dilley, P. Nisbet-Jones, B. W. Shore, and A. Kuhn. Single-photon absorption in coupled atom-cavity systems. *Phys. Rev. A*, 85, 023834, 2012.

[82] S. Ritter, C. Nolleke, C. Hahn, A. Reiserer, A. Neuzner, M.Uphoff, M. Mucke, E. Figueroa, Joerg Bochmann, and G. Rempe. An elementary quantum network of single atoms in optical cavities. *Nature*, 484, 195-200, 2012.

[83] W. B. Joyce and B. C. DeLoach. Alignment of Gaussian beams. *Appl. Opt.*, 23, 4187-4196, 1984.

[84] T. G. Ballance. An ultraviolet fibre-cavity for strong ion-photon interaction. *University of Cambridge: Thesis*, 2016.

[85] G. H. Spencer and M. V. R. K. Murty. General ray tracing Procedure, *Opt. Soc. Am.*, 52, 6:672678, 1962.

[86] A. V. Gorshkov, A. Andr, M. D. Lukin, A. S. Srensen. Photon storage in Λ-type optically dense atomic media. I. Cavity mode. *Phys. Rev. A* 76, 033804, 2007.

[87] B. Vogell, B. Vermersch, T. E. Northup, B. P. Lanyon, C.A. Muschik. Deterministic quantum state transfer between remote qubits in cavities. *Quantum Sci. Technol.* 2, 045003, 2017.

[88] R. Shankart. *Principles of Quantum Mechanics 2nd ed.* Plenum Press, 1994.

[89] S. A. Martucci. Symmetric Convolution and the Discrete Sine and Cosine Transforms, *IEEE Transactions on Signal Processing,* 42(5):1038–1051, 1994.

[90] M. Steiner, H. M. Meyer, C. Deutsch, J. Reichel, and M. Khl. Single Ion Coupled to an Optical Fiber Cavity. *Phys. Rev. Lett.* 10, 043003, 2013.

[91] Physik Instrumente. Alignment for Optics and Silicon Photonics Specifications. *https://static.pi-usa.us/fileadmin/user_upload/pi_us/files/catalogs/PI_Fast_Silicon_Photonics_Alignment-Fully-Automatic.pdf?_ga=2.151013881.196152137.1541782856-713042084.1541782856*, [Accessed 14th November 2018].

[92] X. Liu, K.-H. Brenner, M. Wilzbach, M. Schwarz, T. Fernholz, and J.Schmiedmayer. Fabrication of alignment structures for a fiber resonator by use of deep-ultraviolet lithography, *Appl. Opt*, 44, 6857, 2005.

[93] Physik Instrumente. 6-Axis Alignment System Specifications. *https://static.pi-usa.us/fileadmin/user_upload/physik_instrumente/files/datasheets/H-206-Datasheet.pdf?_ga=2.133715470.1015642451.1542204060-1200013802.1542204060*, [Accessed 14th November 2018].

[94] E. Janitz, M. Ruf, M. Dimock, A. Bourassa, J. Sankey, and L. Childress. Fabry-Perot microcavity for diamond-based photonics, *Phys. Rev. A*, 92, 043844, 2015.

[95] G. Rempe, R. J. Thompson, and H. J. Kimble. Measurement of ultralow losses in an optical interferometer. *Opt. Lett.*, 17, 363, 1992.

[96] T. M. Barlow, R. Bennett, and A. Beige. A master equation for a two-sided optical cavity. *J. Mod. Opt*, 62, 11-20, 2015.

[97] W. Press, S. Teukolsky, W. Vetterling, B. Flannery, E. Ziegel, *Numerical Recipes: The Art of Scientific Computing*, Cambridge University Press; 3rd edt. 2007.

[98] D. T. Clarke and P. Horak, Alignment requirements of Fabry-Perot microresonators for ion trap quantum information processing *Proc. SPIE 10674, Quantum Technologies 2018*, 10.1117/12.2307152, 2018.